Dissertation

submitted to the

Combined Faculty of Natural Sciences and Mathematics

Heidelberg University, Germany

for the degree of

Doctor of Natural Sciences (Dr. rer. nat.)

Presented by

Jing Sun

Oral examination: 24-11-2023

Cavity-controlled thermal reactivity and fermionic dynamics using classical mappings

Referees: Prof. Dr. Oriol Vendrell

Prof. Dr. Andreas Dreuw

Abstract

In quantum chemistry, a full quantum dynamical description of large many-body systems is not currently feasible. One can consider both classical and semi-classical treatments of approximating the quantum dynamics of molecular systems to simulate simpler dynamics. Motivated by their cost-effectiveness and the fact that chemical dynamics take place often in an energy and density-of-states regime where a classical description can be meaningful, a classical description of the quantum dynamics of systems is explored in this dissertation.

We first illustrate how the reaction rate is affected by the cavity effect. *cis-trans* isomerization of HONO is used as an example to demonstrate the cavity-controlled reactivity. Due to the high dimensionality of the potential energy surface, we describe the reaction rate through a classical reactive flux method. The quantum Hamiltonian for simulating cavity-modified molecular dynamics is transformed into a classical mapping Hamiltonian. We consider a single molecule inside the cavity. For simplicity, we assume the cavity is coupled to an aligned molecule. The $x-$ aligned case is studied in both low-friction and strong-friction regimes of the reaction coordinate. The low(strong)-friction regime is also known as the underdamped(overdamped) regime, which is mentioned in Grote-Hynes theory. In the underdamped regime, we illustrate the key difference between a single molecule and a collective of molecules with fixed Rabi splitting. We also show a modification of the reaction rate with different cavity frequencies for different aligned cases. Our results show that the modification of the reaction rate is related to the solvent environment. This will be described in chapter 3.

We then consider free-orientated molecules inside the cavity within the underdamped regime. Compared with aligned cases, the free orientation of molecules leads to a disorder of light-matter coupling, which should be observed in experimental results. Since a thermally excited molecule passing through the barrier is a rare event, we consider N molecules inside the cavity with 1 activated molecule and $N-1$ non-activated molecule. We aim to see how the reaction rate is affected by the number of molecules with fixed coupling strength. We connect the enhancing rate by increasing the number of molecules with the energy transfer efficiency from the activated molecule to the cavity. And the efficiency is sensitive to the resonant frequency. Based on this observation, we also show the modification of the

reaction rate by tuning the lifetime of the cavity. Our findings shed important new light on the question of collective effects in chemical reactivity under vibrational strong coupling. This will be described in chapter 4.

On the other hand, we turn to describe the fermionic dynamics through Meyer-Miller mapping. In chapter 5, We proceed by describing the relation between the initial phase space density of the classically mapped system and the initial configuration of the electrons, and propose strategies to sample this phase space density. We compare the MM mapping with exact quantum results and with different mappings explicitly designed for fermions, namely the SM with and without the inclusion of antisymmetry (the latter corresponds to the original MW mapping), and to the LMM. We then compare Hubbard and impurity Hamiltonians, with and without interactions, and consider as well a model for excitonic energy transfer between chromophores. In this model with interactions we show that the classical MM mapping is able to capture interference effects caused by the presence of different energy transfer pathways leading to the same final state, both when the interferences are constructive and destructive. Our results show that the construction of the maximal fermionic occupation does not seem to be necessary. Also, the performance of the mappings is sensitive to sampling strategies of the initial phase-space distribution for fermions.

Zusammenfassung

In der Quantenchemie ist eine vollständige quantenmechanische Beschreibung großer Vielteilchensysteme derzeit nicht durchführbar. Sowohl klassische als auch halbklassische Ansätze zur Approximation der quantenmechanischen Dynamik von molekularen Systemen haben eine lange Geschichte und wurden durch ihre Kosteneffizienz und die Tatsache motiviert, dass chemische Dynamiken oft in einem Energie- und Zustandsdichte-Regime stattfinden, in dem eine klassische Beschreibung sinnvoll sein kann.

In dieser Arbeit zeigen wir, wie die Reaktionsrate durch den Hohlraumeffekt beeinflusst wird. Wir wählen die Beschreibung der Reaktionsrate durch eine klassische reaktive Flussmethode. Daher wird ein klassischer Zuordnungs-Hamiltonian zur Simulation von hohlraummodifizierter molekularer Dynamik durchgeführt. Die *cis-trans*-Isomerisierung von HONO wird als Beispiel verwendet, um die hohlraumgesteuerte Reaktivität zu demonstrieren. Der Fall der x-Ausrichtung wird sowohl im Bereich geringer Reibung als auch im Bereich starker Reibung der Reaktionskoordinate untersucht. Der Bereich geringer (starker) Reibung wird auch als der unterdämpfte (überdämpfte) Bereich bezeichnet, wie es in der Grote-Hynes-Theorie erwähnt wird. Danach konzentrieren wir uns auf den unterdämpften Bereich. Wir veranschaulichen den wesentlichen Unterschied zwischen einem einzelnen Molekül und einer Gruppe von Molekülen mit fester Rabi-Aufspaltung. Außerdem zeigen wir eine Modifikation der Reaktionsrate bei unterschiedlichen Hohlraumfrequenzen für verschiedene Ausrichtungsfälle. Unsere Ergebnisse zeigen, dass die Modifikation der Reaktionsrate mit der Lösungsmittelumgebung zusammenhängt. Dies wird im Kapitel 3 beschrieben.

Dann betrachten wir frei ausgerichtete Moleküle innerhalb des Hohlraums im unterdämpften Bereich. Im Vergleich zu den ausgerichteten Fällen führt die freie Ausrichtung der Moleküle zu einer Störung der Kopplung von Licht und Materie, die in experimentellen Ergebnissen beobachtet werden sollte. Da ein thermisch angeregtes Molekül, das die Barriere überwindet, ein seltenes Ereignis ist, betrachten wir N Moleküle im Hohlraum, wobei ein Molekül aktiviert ist und $N - 1$ Moleküle nicht aktiviert sind. Wir möchten sehen, wie die Reaktionsrate von der Anzahl der Moleküle mit fester Kopplungsstärke beeinflusst wird. Wir verknüpfen die Verbesserungsrate durch Erhöhen der Anzahl der Moleküle mit der Energieübertragungseffizienz vom aktivierten Molekül auf den Hohlraum. Die Ef-

fizienz ist empfindlich gegenüber der Resonanzfrequenz. Basierend auf dieser Beobachtung zeigen wir auch die Modifikation der Reaktionsrate durch das Einstellen der Lebensdauer des Hohlraums. Unsere Erkenntnisse werfen wichtiges neues Licht auf die Frage der kollektiven Effekte in der chemischen Reaktivität unter Vibrationsstarker Kopplung. Dies wird im Kapitel 4 beschrieben.

Im zweiten Teil beschreiben wir die fermionische Dynamik durch die Meyer-Miller-Zuordnung. Im Kapitel 5 fahren wir fort, indem wir die Beziehung zwischen der anfänglichen Phasenraumdichte des klassisch abgebildeten Systems und der anfänglichen Konfiguration der Elektronen beschreiben und Strategien zur Abtastung dieser Phasenraumdichte vorschlagen. Wir vergleichen die MM-Zuordnung mit exakten quantenmechanischen Ergebnissen und mit verschiedenen Zuordnungen, die explizit für Fermionen entwickelt wurden, nämlich der SM mit und ohne die Berücksichtigung der Antisymmetrie (wobei letzteres der ursprünglichen MW-Zuordnung entspricht) und der LMM. Wir vergleichen dann Hubbard- und Impuls-Hamiltonians, sowohl mit als auch ohne Wechselwirkungen, und betrachten auch ein Modell für den energetischen Austausch von Exzitonen zwischen Chromophoren. In diesem Modell mit Wechselwirkungen zeigen wir, dass die klassische MM-Zuordnung in der Lage ist, Interferenzeffekte zu erfassen, die durch das Vorhandensein verschiedener Energieübertragungswege zum gleichen Endzustand verursacht werden, sowohl wenn die Interferenzen konstruktiv als auch destruktiv sind. Unsere Ergebnisse zeigen, dass der Aufbau der maximalen fermionischen Besetzung scheinbar nicht notwendig zu sein scheint. Außerdem ist die Leistung der Zuordnungen empfindlich gegenüber Abtaststrategien der anfänglichen Phasenraumverteilung für Fermionen.

Contents

List of Figures

List of Tables

Chapter 1

Introduction

In this chapter, we first briefly introduce the cavity with vibraional strong coupling. Starting from polariton states, we mention these state can be prepared by Fabry-Perot cavity. We point out the important experimental results observing modification of reaction rate inside the cavity. These observations indicate the potential of controlling chemical processes through the cavity, which inspires theoretical approaches to explain the mechanism behind the cavity effect.

Then, we turn to introduce mixed quantum-classical approaches that have been used in electronic dynamics and the benefits of using the mixed quantum-classical approaches. Several mapping approaches are presented in terms of electronic states, which shows that the electronic dynamics can be described by classical variables. Then the concept is extended to use classical mapping for fermions. For example, Li-Miller mapping has been used to describe fermions, which shows promising results in non-interacting systems. Here, we aim to explore the applicability of Meyer-Miller mapping for fermions in both non-interacting and interacting systems.

1.1 Introduction to cavity QED

In this section, we briefly mention the polariton states, which can be prepared by Fabry Perot cavities. We then focus on the cavities with vibrational strong coupling. We describe important experimental results of the modification of groundstate reaction rates with vibrational strong coupling. These experiments inspire the theoretical approaches to explain the modification, and the mechanism behind it, which is also the goal of this study.

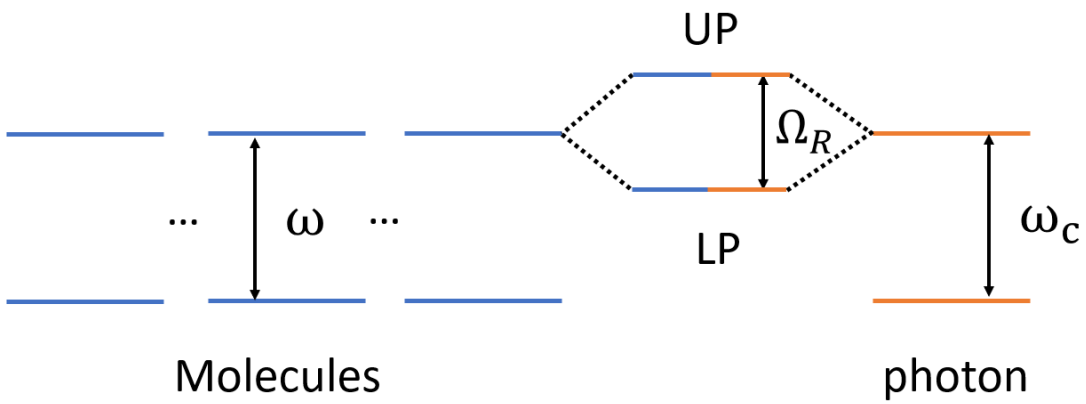

Figure 1.1. A schematic demonstration of hybridized state between molecular states and photon state. As the photon frequency matches the transition of the molecules, the polariton states are formed, including upper and lower polariton states(UP and LP). The energy gap between UP and LP is defined as Rabi splitting, Ω_R.

1.1.1 Polaritonic states

Theoretical studies of hybrid states of light and matter, or polaritonic states, can be traced back to the 1950s [1,2]. The polaritons have been experimentally observed since the 1980s [3, 4]. Most recently, polariton chemistry become an active field of study. Since experimental research demonstrates the potential to manipulate chemical processes, various theoretical studies have flourished with the aim of explaining the key factor of the polaritonic effect on the processes.

The formation of the polariton is attributed to light-matter coupling. Light plays an important role in a chemical process. Photon is both a basic ingredient in chemical reactions and a fundamental tool for the examination of molecular properties. As the coupling is weak, the electromagnetic field of light is treated as a perturbation, which provides access for the system to visit other quantum states. However, the assumption of the perturbation breaks down as the coupling is strong enough to overcome the dissipating process of the photon. In this strong coupling regime, light and molecules of the system form hybrid states, which give different properties from individual photons and molecules. The hybrid states between a photon and a group of molecules consist of 2 polaritonic states and a large number of dark states(shown in fig 1.1). The polaritonic state with higher(lower) energy is denoted as upper(lower) polariton, which is delocalized. The energy gap between the lower polariton(LP) and the higher polariton(UP) is defined as Rabi splitting. While the dark states are localized and nearly degenerate manifold of states.

1.1.2 Vibrational and electronic strong coupling

There are different ways to reach a strong coupling regime. By utilizing the surface plasmon [5, 6] of nanoparticles, an intense electromagnetic field is formed inside a nanocavity, which overcomes the dissipative process. However, the resonant frequency is dependent on the shape and size of the nanoparticles and plasmon modes. The control of their shape and size to tune the resonant frequency is challenging. We highlight a Fabry-Perot cavity [7], a type of optical microcavity, which can be used to achieve strong coupling between photons and molecules. The cavity consists of two mirrors that trap the electromagnetic field inside. And the frequency of the trapped field depends on the cavity size. When the cavity frequency matches the optical transition of the molecules, the photon and molecular states form hybrid states. The cavity can be tuned to couple with either the electronic or the vibrational transition of the molecules, resulting in electronic strong coupling (ESC) or vibrational strong coupling (VSC), respectively.

1.1.3 Experiments and theoretical approaches

Recently, a modified reaction rate of photoisomerization in merocyanine compounds under ESC with optical microcavities has been reported by Ebbesen and his colleagues [8]. This is a promising approach for manipulating fundamental chemical processes. By interacting with a vacuum field, the rates and branching ratios of these basic chemical processes can be altered in a reversible way. This means we can achieve selective control of excited state reactivity, without exposing delicate molecular species or materials to the harmful effects of intense laser fields.

Inspired by the results of Ebbesen's group, various experimental studies have been done to examine the cavity effect on the reaction rate of different chemical processes. [9–11] One of the recent advances in the field is the observation of the modified efficiency of singlet fission through strong light-matter coupling within an optical microcavity [12–14]. This phenomenon involves the formation of polaritons that alter the relative energy levels between electron donor and acceptor manifolds, enabling the conversion of a singlet state into two triplet states. This process could potentially enhance the external quantum efficiency of organic optoelectronic devices by increasing the number of charge carriers generated per photon absorbed.

On the other hand, similar studies for VSC have also been shown recently. They focus on the manipulation of chemical reactions in the ground electronic state inside Fabry–Perot cavities [15–17]. Concerning the ground state reactions inside the cavity with VSC, the experiments are carried out in the dark. That is to say, the system remains in groundstate without being excited by external laser light. The decreased reactivity is observed for silyl

cleavage in an alkynylsilane [15,16]. While an increased reactivity is shown in the hydrolysis of para-nitrophenyl acetate [17]. Hence, a number of theoretical studies have been done with the aim of explaining how the cavity enhances or suppresses the reaction rate.

To illustrate how the cavity alters the reaction rate, a single molecule inside the cavity has been investigated due to simplicity. The reaction rate inside the cavity has been described by transition state theory(TST), which concludes the VSC-modified reactivities cannot be explained by TST [18]. To go beyond TST, a number of theoretical works describe the reactivity through different methods. The transmission coefficient based on the Grote-Hynes theory is utilized to describe reactivity. At first, only suppression of the reactivity is predicted [19, 20]. Later, both suppression and enhancement of the reactivity are performed, which is connected to the solvent effect [21–23]. On the other hand, a full quantum rate is described through the hierarchical equations of motion approach, which gives an increasing reactivity [24].

However, experimental studies mostly report a number of molecules inside the cavity. Theoretical studies for a single molecule must assume an ultrastrong coupling between the cavity and the molecule in order to fix the Rabi splitting. The gap between a single molecule with ultrastrong coupling and a collective of molecules with weak coupling is still an open question. With the aim to illustrate the collective effect, classical molecular dynamics have been implemented. [25–27] Due to the computational cost, a number of 1-D systems with fixed dipole are considered in quantum calculations, which concludes the importance of the dark states and the energy disorder [28–30]. Overall, despite many theoretical efforts, a clear theoretical explanation of the experimentally observed modifications of ground-state chemical reactivity is unavailable. In this study, we aim to illustrate how the reaction rate is affected inside the cavity by investigating the isomerization of HONO inside the cavity.

1.2 Introduction to classical mapping

In this section, we first introduce the benefits of mixed quantum-classical approaches. We then focus on classical mapping approaches. These mapping approaches are first used to describe fermionic states. Following the successful results of the mapping fermionic states, the mapping approaches are then applied to mapping fermions, which inspires us to investigate the application of Meyer-Miller mapping of fermionic dynamics.

1.2.1 Mixed quantum-classical approaches

A realistic simulation of complex systems with full quantum dynamics is generally intractable. Therefore, we often have to partition the problem into a (small) quantum subsys-

tem and a classical environment that can be modeled with simpler dynamics. In chemistry, describing the dynamics of a system through mixed quantum-classical method is nothing new [31–50]. Under *nonadiabatic* process, the electronic states are strongly coupled to the nuclei coordinates, which is highly studied in the field of solar cells, vision, and photosynthesis, among others. When the coupling between the electronic states and the neucei coordinates cannot be neglected, we often treat a molecular system as a subsystem of N electronic states coupled to an environment of classical nuclear modes. The nuclei motion is approximated by an ensemble of independent trajectories that propagate under classical equations of motion. Among the simplest trajectory-based methods are Ehrenfest dynamics [36,37], in which the nuclei move on a mean-field potential defined by the instantaneous electronic populations, while the electronic variables follow exact subsystem dynamics according to the instantaneous nuclear configuration. This method has a number of known severe drawbacks.

Another way is to, however; simulate the quantum nature of the initial state through a quasiclassical sampling of the corresponding probability distribution. By exploring the classical limit of quantum mechanics, new theoretical concepts have been developed, including mean-field trajectories, surface hopping [36, 37], quantum-classical Liouville method [51–58], and various phase-space representations of quantum mechanics with the semiclassical propagator [32, 34, 59, 60]. In addition, there is another benefit to describing quantum phenomena by a classical method. The numerical effort of a quantum-mechanical calculation increases exponentially in terms of the degrees of freedom while a classical calculation increases linearly instead. These classical approaches have been applied to a wide range of studies, including internal conversion [61], nonadiabatic process [62], and recently cavity dynamics [63].

1.2.2 Classical mapping of electronic states

Let us focus on one of the treatments, which describes the electronic dynamics by mapping the discrete space of diabatic or adiabatic electronic states, into a set of classical variables, which then evolve together with the nuclei under an overall classical Hamiltonian. Several mappings have been proposed for the electronic degrees of freedom, for example, the original Meyer-Miller (MM) Hamiltonian consisting of one harmonic oscillator per electronic state, and different flavors of the spin-mapping (SM) Hamiltonian, which use classical spin degrees of freedom to map the state of the electronic subspace [34, 60]. We stress that the nuclear-electronic MM Hamiltonian can be re-quantized, which leads to the exact quantum dynamics. And this mapping is also known as MMST. [41]

However, the equation of motion (EOM) of fully classical mapping is not necessarily

an approximation. Both the classical EOM of the MM mapping for the electronic states and solving the Schrödinger equation are formally equivalent and have a close formal resemblance with the Ehrenfest method [32, 34]. The differences are, however, significant and related to how initial conditions are sampled and to how observables are derived from the trajectories [32, 34, 59, 60]. One can argue that mapping approaches provide a more fundamental answer to the question of how to mix classical and quantum degrees of freedom than, e.g. Ehrenfest or surface-hopping approaches [36, 37], and often outperform them in benchmark applications [48, 49, 64, 65].

1.2.3 Classical mapping of second quantization

Miller and White took the pioneering step to extend the concept of classical mappings to the treatment of electrons (fermions) under a second-quantized Hamiltonian [31]. This step can be motivated by the formal similarity between the second-quantized Hamiltonian for bosons and fermions, and the fact that the bosonic creation/annihilation operators are analogous to the ladder operators of interacting harmonic oscillators, which can subsequently be downgraded to classical variables to obtain useful mapping. In their work, Miller and White arrived at a mapping for the fermionic operators using the Heisenberg correspondence relation [66, 67] between matrix elements and classical variables. By construction, the Miller-White (MW) mapping respects the sign-change rules of the the commutation relations of fermionic operators. Although it is not presented in this way in Ref. 31, this mapping can be alternatively reached by first performing a (exact) Jordan-Wigner transformation of the fermionic Hamiltonian into a corresponding chain of spins [68], where so-called sign-change operators $(1 - 2\hat{n}_j)$ appear, and then taking a spin-mapping (SM) [32–34, 60] for each fermionic degree of freedom.

In their original work, the MW mapping was not applied to dynamical processes but it was demonstrated that it yields the correct energy for selected electronic configurations of the helium atom and of the hydrogen molecule. Subsequent works reformulated the MW mapping on the basis of a Cartesian Hamiltonian, like in the original MM mapping, while still preserving the sign-change rules of the fermionic operators. [69–72] This mapping, called Li-Miller mapping (LMM) in a recent publication [72], yields the exact dynamics of the fermions in Fock space for non-interacting Hamiltonians [69]. Based on these developments, promising results have been obtained in studies of electronic dynamics and quantum transport in molecular junctions and quantum dots. [59,60,69–75] These results indicate that a broader range of electronic processes in molecules may be approachable through classical mappings of the electronic degrees of freedom in Fock space, which is one of the motivations for this work.

It turns out that the original MM mapping applied to non-interacting fermionic Hamiltonians, in the same way as the LMM, deliver the exact dynamics of the system when the initial state is a physical fermionic state. Starting from this observation, in this study we explore this formal connection and examine the applicability of the original MM mapping to the quantum dynamics of electrons in closed systems in a second quantized setting.

Chapter 2

Theory

In this chapter, we describe the methodologies that are applied to our studies including cavity-controlled isomerization of HONO and classical mapping for fermionic dynamics. We first derive the Hamiltonian of cavity quantum electrodynamics(cavity QED). Then we transform this quantum Hamiltonian into classical function with Meyer-Miller mapping on the cavity mode. Since we focus on the modification of the reaction rate inside the cavity, a classical reaction rate method is used.

Moreover, we perform three different mappings including Meyer-Miller mappings, spin mapping, and Li-Miller mapping. We demonstrate how the mappings transform second quantization operators for fermion into classical variables. In addition, two different sampling methods are provided which will be discussed in non-interacting systems.

2.1 Quantized light-matter interaction

Starting from a minimally coupled coulomb Hamiltonian governing the non-relativistic dynamics of matter in an electromagnetic(EM) environment [76], we have:

$$\hat{H} = \sum_i \frac{1}{2m_i} \left[\hat{\boldsymbol{P}}_i - z_i \hat{\boldsymbol{A}}(r_i, t) \right]^2 + \hat{V} + \hat{H}_{EM}, \tag{2.1}$$

in which the vectors are represented by bold cases. $\hat{\boldsymbol{P}}_i = -i\hbar\nabla_i$. m_i and z_i represent i-th particle's mass and charge, respectively. Index i runs over all nuclei and electronic coordinates. $\hat{V}$ includes nuclei-nuclei, nuclei-electron, and electron-electron interaction.

$\hat{\boldsymbol{A}}(r_i, t)$ represents the vector field of the EM environment. Quantized electric($\hat{\boldsymbol{E}}$) and magnetic fields($\hat{\boldsymbol{B}}$) of EM can be connected to $\hat{\boldsymbol{A}}$ by Maxwell's equations [77]. By forcing the Coulomb gauge $\nabla \cdot \hat{\boldsymbol{A}} = 0$, a unique $\hat{\boldsymbol{A}}$ is defined and only the transverse component of EM is included. Hence, $\hat{H}_{EM}$ can be expressed by quantized electric and magnetic fields,

$$\hat{H}_{EM} = \frac{\epsilon_0}{2} \int d\boldsymbol{r} \left[\hat{\boldsymbol{E}}(\boldsymbol{r})^2 + c^2 \hat{\boldsymbol{B}}(\boldsymbol{r})^2 \right], \tag{2.2}$$

where ϵ_0 is the extinct coefficient of vacuum and c is the speed of light. In additions, the relations of $\hat{\boldsymbol{A}}$, $\hat{\boldsymbol{E}}$, and $\hat{\boldsymbol{B}}$ can be expressed by [78]

$$\hat{\boldsymbol{E}} = -\frac{\partial \hat{\boldsymbol{A}}}{\partial t}, \tag{2.3}$$

$$\hat{\boldsymbol{B}} = \nabla \times \hat{\boldsymbol{A}}. \tag{2.4}$$

A general solutions of $\hat{\boldsymbol{A}}(\boldsymbol{r}, t)$, $\hat{\boldsymbol{E}}(\boldsymbol{r}, t)$, and $\hat{\boldsymbol{B}}(\boldsymbol{r}, t)$ are expressed as a sum over all the modes,

$$\hat{\boldsymbol{A}}(\boldsymbol{r}, t) = \sum_{\alpha} \boldsymbol{u}_{\alpha} \left(\hat{A}_{\alpha} e^{i(\boldsymbol{k}\cdot\boldsymbol{r} - \omega_{\alpha} t)} + \hat{A}_{\alpha}^{\dagger} e^{i(-\boldsymbol{k}\cdot\boldsymbol{r} + \omega_{\alpha} t)} \right) \tag{2.5}$$

$$\hat{\boldsymbol{E}}(\boldsymbol{r}, t) = i \sum_{\alpha} \omega_{\alpha} \boldsymbol{u}_{\alpha} \left(\hat{A}_{\alpha} e^{i(\boldsymbol{k}\cdot\boldsymbol{r} - \omega_{\alpha} t)} - \hat{A}_{\alpha}^{\dagger} e^{i(-\boldsymbol{k}\cdot\boldsymbol{r} + \omega_{\alpha} t)} \right) \tag{2.6}$$

$$\hat{\boldsymbol{B}}(\boldsymbol{r}, t) = i \sum_{\alpha} \boldsymbol{k} \times \boldsymbol{u}_{\alpha} \left(\hat{A}_{\alpha} e^{i(\boldsymbol{k}\cdot\boldsymbol{r} - \omega_{\alpha} t)} - \hat{A}_{\alpha}^{\dagger} e^{i(-\boldsymbol{k}\cdot\boldsymbol{r} + \omega_{\alpha} t)} \right), \tag{2.7}$$

where $\boldsymbol{u}_{\alpha}$ is a unit vector denoting the direction of the vector potential. Focusing on $\hat{H}_{EM}$ which is a time-independent Hamiltonian, then we have

$$\hat{\boldsymbol{A}}(\boldsymbol{r}) = \sum_{\alpha} \boldsymbol{u}_{\alpha} \left(\hat{A}_{\alpha} e^{i\boldsymbol{k}\cdot\boldsymbol{r}} + \hat{A}_{\alpha}^{\dagger} e^{-i\boldsymbol{k}\cdot\boldsymbol{r}} \right) \tag{2.8}$$

$$\hat{\boldsymbol{E}}(\boldsymbol{r}) = i \sum_{\alpha} \omega_{\alpha} \boldsymbol{u}_{\alpha} \left(\hat{A}_{\alpha} e^{i\boldsymbol{k}\cdot\boldsymbol{r}} - \hat{A}_{\alpha}^{\dagger} e^{-i\boldsymbol{k}\cdot\boldsymbol{r}} \right) \tag{2.9}$$

$$\hat{\boldsymbol{B}}(\boldsymbol{r}) = i \sum_{\alpha} \boldsymbol{k} \times \boldsymbol{u}_{\alpha} \left(\hat{A}_{\alpha} e^{i\boldsymbol{k}\cdot\boldsymbol{r}} - \hat{A}_{\alpha}^{\dagger} e^{-i\boldsymbol{k}\cdot\boldsymbol{r}} \right). \tag{2.10}$$

Combing eq 2.2 and eq 2.8, we arrive

$$\hat{H}_{EM} = \sum_{\alpha} \epsilon_0 V \omega_{\alpha}^2 \left(\hat{A}_{\alpha}^{\dagger} \hat{A}_{\alpha} + \hat{A}_{\alpha} \hat{A}_{\alpha}^{\dagger} \right), \tag{2.11}$$

where V represents the cavity volume [79]. In the second quantization, the photonic Hamiltonian can be written as,

$$\hat{H}_{EM} = \sum_{\alpha} \frac{\hbar \omega_{\alpha}}{2} \left(\hat{a}_{\alpha}^{\dagger} \hat{a}_{\alpha} + h.c. \right) = \sum_{\alpha} \hbar \omega \left(\hat{a}_{\alpha}^{\dagger} \hat{a}_{\alpha} + \frac{1}{2} \right), \tag{2.12}$$

with the equivalence,

$$\hat{A}_{\alpha} \equiv \sqrt{\frac{\hbar}{2\epsilon_0 \omega_{\alpha} V}} \hat{a}_{\alpha}, \quad \hat{A}_{\alpha}^{\dagger} \equiv \sqrt{\frac{\hbar}{2\epsilon_0 \omega_{\alpha} V}} \hat{a}_{\alpha}^{\dagger}. \tag{2.13}$$

Therefore, for each radiation mode α, the EM field is quantized, which corresponds to the quantum harmonic oscillator. Also, $\hat{H}_{EM}$ can be written as

$$\hat{H}_{EM} = \frac{1}{2} \sum_{\alpha} \left(\hat{p}_{\alpha}^2 + \omega_{\alpha}^2 \hat{q}_{\alpha}^2 \right), \tag{2.14}$$

with canonical position and momentum,

$$\hat{q}_\alpha = \sqrt{\frac{\hbar}{2\omega_\alpha}}\left(\hat{a}_\alpha^\dagger + \hat{a}_\alpha\right), \quad \hat{p}_\alpha = i\sqrt{\frac{\hbar}{2\omega_\alpha}}\left(\hat{a}_\alpha^\dagger - \hat{a}_\alpha\right). \tag{2.15}$$

Therefore, eq 2.1 is rewritten as,

$$\hat{H} = \sum_i \frac{1}{2m_i}\left[\hat{P}_i - z_i\hat{A}\right]^2 + \hat{V} + \frac{1}{2}\sum_\alpha\left(\hat{p}_\alpha^2 + \omega_\alpha^2\hat{q}_\alpha^2\right), \tag{2.16}$$

We then apply Power-Zienau-Woolley (PZW) transformation [80, 81],

$$U_{PZW} = exp\left[\frac{-i}{\hbar}\hat{\boldsymbol{\mu}}\cdot\hat{A}\right], \tag{2.17}$$

to eq 2.16, in which $\hat{\boldsymbol{\mu}}$ is the dipole operator of the system, $\hat{\boldsymbol{\mu}} = \sum_i z_i\hat{\boldsymbol{r}}_{\boldsymbol{i}}$. U_{PZW} does nothing but transform matter and photon momentum,

$$\hat{P}_i - z_i\hat{A} \to \hat{P}_i, \quad \hat{p}_\alpha \to \hat{p}_\alpha + \boldsymbol{\lambda_\alpha}\cdot\boldsymbol{\mu}, \tag{2.18}$$

where $\boldsymbol{\lambda_\alpha} = \sqrt{1/\epsilon_0 V}\boldsymbol{u}_\alpha$. Thus, we have,

$$\hat{H} = \sum_i \frac{1}{2m_i}\hat{P}_i^2 + \hat{V} + \frac{1}{2}\sum_\alpha\left(\left(\hat{p}_\alpha + \boldsymbol{\lambda_\alpha}\cdot\boldsymbol{\mu}\right)^2 + \omega_\alpha^2\hat{q}_\alpha^2\right). \tag{2.19}$$

Finally, a canonical transform is applied, which leads to

$$\hat{p}_\alpha \to -\omega_\alpha\hat{q}_\alpha, \quad \hat{q}_\alpha \to \frac{1}{\omega_\alpha}\hat{q}_\alpha. \tag{2.20}$$

And we arrive,

$$\hat{H} = \sum_i \frac{1}{2m_i}\hat{P}_i^2 + \hat{V} + \hat{H}_{cav} \tag{2.21}$$

$$\hat{H}_{cav} = \frac{1}{2}\sum_\alpha\left(\hat{p}_\alpha^2 + \omega_\alpha^2\left(\hat{q}_\alpha - \frac{\boldsymbol{\lambda_\alpha}\cdot\boldsymbol{\mu}}{\omega_\alpha}\right)^2\right). \tag{2.22}$$

This form of light-matter interaction has become standard in most theoretical studies of VSC [18, 19, 82, 83]. Details on its derivation and properties [84] can also be found elsewhere [79, 84, 85]. Similarly to other studies and to facilitate comparisons, we introduce the coupling parameter $g = \lambda\sqrt{\hbar\omega_{cav}/2}$, which has units of electric field (using this relation and $\hat{q}_{cav} = \sqrt{\hbar/2\omega_{cav}}(\hat{a}^\dagger + \hat{a})$, the linear coupling term in $\hat{H}_{cav}$ reads $g\,\boldsymbol{\epsilon}\cdot\boldsymbol{\mu}\,(\hat{a}^\dagger + \hat{a})$).

Eq 2.21 shows the quantum hamiltonian when considering molecules inside the cavity. In this study, we aim to describe the cavity effect on the reactivity of the system in which the molecule is described by a multi-dimensional potential energy surface. Due to the high computational cost of the high dimensionality, we describe the reactivity of the

system through classical mechanics. Hence, the quantum Hamiltonian is transformed into a classical Hamiltonian

$$H = \sum_i \frac{1}{2m_i} P_i^2 + V + H_{cav} \tag{2.23}$$

$$H_{cav} = \frac{1}{2} \sum_\alpha \left(p_\alpha^2 + \omega_\alpha^2 \left(q_\alpha - \frac{\boldsymbol{\lambda_\alpha} \cdot \boldsymbol{\mu}}{\omega_\alpha} \right)^2 \right). \tag{2.24}$$

The classical analog description of $\hat{H}_{cav}$ is obtained by mapping position and momentum operators of quantum harmonic oscillators into corresponding classical position and momentum variables, which is equivalent to the Meyer-Miller mapping [32, 41, 59]. The Meyer-Miller mapping is carefully described in section 2.3. A classical description of the VSC regime is not new and has been successfully applied to bulk systems described by force-field potentials [25] and model Hamiltonians [19, 86]. This Hamiltonian will be used in chapter 3 and 4.

2.2 Reaction rate beyond transition state theory

2.2.1 Reactive flux method

Here, we aim to derive the rate equation, which can be utilized to describe reactions inside and outside the cavity. More details can be found in the textbook written by David Chandler [87]. Starting from a chemical reaction

$$A \iff B, \tag{2.25}$$

where both species A and B are at low concentration in the system. The phenomenological rate equations can be written as

$$\frac{dC_A}{dt} = -k_{BA} C_A(t) + k_{AB} C_B(t), \tag{2.26}$$

$$\tag{2.27}$$

and

$$\frac{dC_B}{dt} = k_{BA} C_A(t) - k_{AB} C_B(t), \tag{2.28}$$

where k_{BA} and k_{AB} are forward and backward rate constants, respectively. And $C_A(t)$ and $C_B(t)$ denote the concentration of species A and B as functions of time. Note that the number of molecules in the system is conserved, which means $C_A(t) + C_B(t) = 1$. When the system reached the equilibrium, the equilibrium concentration, $\langle C_A \rangle$ and $\langle C_B \rangle$, should

obey the detail balance condition, which means $-k_{BA}\langle C_A\rangle + k_{AB}\langle C_B\rangle = 0$. Thus one can obtain

$$K_{eq} = \frac{\langle C_B\rangle}{\langle C_A\rangle} = \frac{k_{BA}}{k_{AB}}. \tag{2.29}$$

Combining eq 2.29 and the detail balance condition, one arrives at

$$\langle C_A\rangle + \langle C_B\rangle = \frac{\tau_{rxn}^{-1}}{k_{AB}}\langle C_A\rangle, \tag{2.30}$$

where $\tau_{rxn}^{-1} = k_{BA} + k_{AB}$. Inserting it back into eq 2.26, then we have

$$\Delta C_A(t) = C_A(t) - \langle C_A\rangle = \Delta C_A(0)e^{-t/\tau_{rxn}}. \tag{2.31}$$

According to the fluctuation-dissipation theorem [87], we now have

$$e^{-t/\tau_{rxn}} = \frac{\Delta C_A(t)}{\Delta C_A(0)} = \frac{\langle \theta_A[q(0)]\theta_A[q(t)] - x_A^2\rangle}{x_A x_B}, \tag{2.32}$$

in which x_A and x_B denotes the molar fraction of A and B, respectively. Bra and ket illustrate the ensemble average. $\theta_A[q(t)]$ represent the heavside function, which gives

$$\theta[q(t)] = 1, \quad q(t) < q^{\ddagger} \tag{2.33}$$

$$\theta[q(t)] = 0, \quad q(t) > q^{\ddagger} \tag{2.34}$$

Along the reaction coordinate, q, $q^{\ddagger}$ defines the dividing surface between species A and B. In order to analyze the relation between τ_{rxn} and $\theta_A(t)$, we take the time derivative of eq 2.32, which leads to

$$\tau_{rxn}^{-1}e^{-t/\tau_{rxn}} = -(x_A x_B)^{-1}\langle \theta_A[q(0)]\dot{\theta}_A[q(t)]\rangle. \tag{2.35}$$

Here, the dot describes a time derivative. Due to the properties of the auto-correlation function, we have

$$\langle \theta_A[q(0)]\dot{\theta}_A[q(t)]\rangle = -\langle \dot{\theta}_A[q(0)]\theta_A[q(t)]\rangle. \tag{2.36}$$

Based on the chain rule, the derivative of $\dot{\theta}_A[q]$ can be expanded as

$$\dot{\theta}_A[q] = \dot{q}\frac{d\theta_A}{dq} = -\dot{q}\delta(q - q^{\ddagger}). \tag{2.37}$$

Therefore, one can obtain

$$\dot{q}\frac{d\theta_A}{dq} = -\langle \dot{q}(0)\delta[q(0) - q^{\ddagger}]\theta_A[q(t)]\rangle \tag{2.38}$$

$$= \langle \dot{q}(0)\delta[q(0) - q^{\ddagger}]\theta_B[q(t)]\rangle. \tag{2.39}$$

We note that $\theta_B[q(t)] = 1 - \theta_A[q(t)]$, and $\langle \dot{q}(0)\delta[q(0) - q^{\ddagger}]\rangle = 0$. This can be explained by that velocity, $\dot{q}(0)$, is an odd function while the ensemble average is an even function, which is independent of a given geometry. Finally, we obtain

$$\tau_{rxn}^{-1} e^{-t/\tau_{rxn}} = (x_A x_B)^{-1} \langle \dot{q}(0)\delta[q(0) - q^{\ddagger}]\theta_B[q(t)]\rangle. \tag{2.40}$$

However, the quality in eq 2.40 is not correct for all time t. The phenomenological rate can only be right on a time scale that is long enough to observe transient behavior and shorter than the relaxations of the transient behavior. That is to say $e^{-t/\tau_{rxn}} \approx 1$. And we have

$$\tau_{rxn} = (x_A x_B)^{-1} \langle \dot{q}(0)\delta[q(0) - q^{\ddagger}]\theta_B[q(t)]\rangle, \tag{2.41}$$

and

$$K(t) = k_{BA}(t) = x_A^{-1} \langle \dot{q}(0)\delta[q(0) - q^{\ddagger}]\theta_B[q(t)]\rangle. \tag{2.42}$$

As a result, in the whole study, we describe the reaction rate inside and outside the cavity by eq 2.42.

The exact reactive flux is obtained in the limit $t \to \infty$, in practice when the plateau for $K(t)$ is reached [88]. This occurs when all classical trajectories starting from the dividing surface become trapped at either the reactants or products side. For example, for the isomerization reaction of n-butane in the low-friction the environment of a van der Waals liquid this relaxation time is about 1 ps [89]. Now, since [87]

$$\lim_{t \to 0^+} K(t) = K_{TST}, \tag{2.43}$$

one can introduce a transmission coefficient $\kappa(t)$ as $K(t) = \kappa(t) K_{TST}$, which can be evaluated as the quotient of the numerically exact reactive flux and the reactive flux without recrossing, i.e. the TST assumption. K_{TST} can be evaluated conveniently using Eyring's equation [90, 91], which will be shown in later, while $\kappa(t)$ is obtained from classical trajectories.

2.2.2 Reaction rate inside and outside cavity

As has been discussed in other works [18,92,93], $K_{TST}^{(c)}$ is, to a good approximation, insensitive to cavity effects (here and in the following we use a super-index to indicate in-cavity or out-of-cavity quantities). Therefore, we consider $K_{TST}^{(c)}$ to be completely cavity-independent and describe the cavity effect on the rate through the ratio

$$R = \frac{K^{(c)}}{K^{(0)}} = \frac{\kappa^{(c)} K_{TST}^{(c)}}{\kappa^{(0)} K_{TST}^{(0)}} \approx \frac{\kappa^{(c)}}{\kappa^{(0)}}, \tag{2.44}$$

where $K^{(0)} = \kappa^{(0)} K^{(0)}_{TST}$ is the formally exact classical rate outside the cavity. Here and in the following, transmission coefficients and rate constants without a time argument refer to their plateau value. Clearly, both $\kappa^{(c)}$ and $\kappa^{(0)}$ lie in the $[0, 1]$ range whereas the ratio R can be both larger or smaller than one, corresponding to a chemical rate enhancement or suppression, respectively.

2.2.3 Reaction rate for the ensemble

It is important to define how to calculate the reactive flux with the expression in Eq. 2.42 when considering a molecular ensemble, since all coordinates of all molecules enter in the definition of the various quantities. In doing so, it is essential to realize that the fraction of activated molecules (AM), F_{AM}, those which are undergoing the chemical transformation at a specific moment in time, to non-activated molecules (NAM) is in general very small. For a unimolecular reaction with a forward rate constant K and a total of N molecules coupled to the cavity, the rate of molecules that start the transformation per unit of time is $dN/dt = KN$. Multiplying by Δ_{TS}, the amount of time the molecule spends crossing the transition state (TS), and dividing by the total number of molecules N results in an estimate for $F_{AM} = K\Delta_{TS}$. Considering a rate of about 10^{-4} s^{-1} as in the example of Ref. 94, and with $\Delta_{TS} \approx 10^{-13}$ s for a typical reaction in solution [95], one obtains $F_{AM} \approx 10^{-17}$. A rate of 10^4 s^{-1}, of the order of the HONO isomerization studied here, results in $F_{AM} \approx 10^{-9}$, still negligible compared to the fraction of spectator NAMs. Hence, when considering the modification of chemical rates for ensembles under strong coupling, one must assume that on average only one AM crosses the barrier at a time. In our classical treatment of the reactive flux, this means that the sampling of transition state configurations according to Eq 2.42 is performed for one molecule only, while the other molecules are in thermal equilibrium close to their minimum energy configurations in the reactant potential energy well. Every set of different model parameters of the simulations studied below consists of a batch of 10^4 trajectories sampled from a canonical ensemble. The simulations are built on top of the OpenMM package for customizable molecular simulation. [96]

2.2.4 Transition state rate evaluation

Although TST rates can be directly evaluated using Eq. 2.43, we find it more convenient to use Eyring's equation

$$K_{TST} = \frac{1}{\beta h} \frac{Z^{\ddagger}}{Z^R} e^{-\beta \Delta E} \tag{2.45}$$

where $Z^{\ddagger}$ and Z^R correspond to the partition function of transition state (TS) and reactant, respectively. The partition functions are evaluated as usual by optimizing the reactant and TS

stationary point geometries for each set of parameters and constructing and diagonalizing the Hessian matrix to obtain separable normal modes. Finally, the quantum mechanical partition functions for the oscillators in the reactants and TS are evaluated using the well-known textbook expressions. ΔE in Eq. 2.45 corresponds to the difference of zero-point energies between reactants and TS. Note that the dividing surface between the reactant and the product is consistent both inside and outside the cavity. Hence, K_{TST} stays consistent both inside and outside the cavity.

2.3 Meyer-Miller Mapping

2.3.1 Mapping of second quantization

The second-quantized Hamiltonian for a many-body system of fermions (electrons in our case) and bosons takes the general form

$$\hat{H} = \hat{H}^{(1)} + \hat{H}^{(2)} \tag{2.46}$$

$$\hat{H} = \sum_{ij}^{F} h_{ij} a_i^\dagger a_j + \frac{1}{2} \sum_{ijkl}^{F} V_{ijkl} a_i^\dagger a_j^\dagger a_l a_k, \tag{2.47}$$

where i, j, k and l run over all single particle states and F is the number of single-particle basis functions used to expand the Fock space. We refer to the annihilation (creation) operators as $\hat{a}_j^{(\dagger)}$ in general and specialize them to $\hat{b}_j$ for bosons and $\hat{c}_j$ for fermions whenever this distinction is needed. These operators obey the respective commutation and anti-commutation relations

$$[\hat{b}_i, \hat{b}_j^\dagger] = \delta_{ij}; \quad [\hat{b}_i, \hat{b}_j] = [\hat{b}_i^\dagger, \hat{b}_j^\dagger] = 0; \tag{2.48}$$

$$\{\hat{c}_i, \hat{c}_j^\dagger\} = \delta_{ij}; \quad \{\hat{c}_i, \hat{c}_j\} = \{\hat{c}_i^\dagger, \hat{c}_j^\dagger\} = 0. \tag{2.49}$$

As is well known, for bosons one can identify the creation and annihilation operators with the ladder operators of a set of harmonic oscillators, one for each bosonic mode, which obey the same commutation relations. The ladder operators can be expressed using the corresponding positions and momenta

$$\begin{aligned} \hat{b}_j &\mapsto \frac{1}{\sqrt{2}}(i\hat{p}_j + \hat{q}_j) \\ \hat{b}_j^\dagger &\mapsto \frac{1}{\sqrt{2}}(-i\hat{p}_j + \hat{q}_j), \end{aligned} \tag{2.50}$$

leading to a form of the bosonic Hamiltonian with a simple classical analog. Note that $\hbar$ is set to be 1 which is also applied to all the other equations in below.

In addition, it is useful to first discuss in some detail the properties of a classical approximation to the dynamics of the $\hat{H}^{(1)}$ term for bosons before considering fermions. Using the

relations (2.50) and replacing quantum operators with classical variables one arrives at the Hamiltonian function

$$H^{(1)}_{\mathrm{B;cl}}(\mathbf{p},\mathbf{q}) = \frac{1}{2}\left(\mathbf{p}^{+}\,\mathbf{h}\,\mathbf{p} + \mathbf{q}^{+}\,\mathbf{h}\,\mathbf{q}\right) - \gamma\ \mathrm{Tr}[\mathbf{h}], \tag{2.51}$$

where the column arrays **p** and **q** collect all momenta and positions, respectively, and **h** is the matrix with elements h_{ij}. The γ factor takes values between 0 and $1/2$ and it does not affect the classical equations of motion. However, it determines the amount of zero-point energy available to the classical system when sampling initial conditions [32, 97]. Hence, the results obtained with the mapping for interacting systems depend on γ. In the numerical results discussed below we have made the experience, similarly to other applications in the literature [59,60], that $\gamma \approx 0.366$ works best, and this is the value we keep throughout. This Hamiltonian is identical with the electronic part of the original MM Hamiltonian [32,41,59], although in this case the classical oscillators do not map the amplitudes of the electronic states, but instead the number of particles in each single particle state, $n_j = (p_j^2 + q_j^2)/2 - \gamma$.

2.3.2 Equation of motion

The equations of motion of the classical positions and momenta follow from the usual prescription: substitute the commutator with the Poisson bracket in the corresponding Heisenberg equations of motion, or equivalently derive Hamilton's equations directly from the classical form of the Hamiltonian. The linear Hamilton's equations arising from Hamiltonian (2.51) are

$$\dot{\mathbf{q}} = \mathbf{h}\,\mathbf{p}; \quad -\dot{\mathbf{p}} = \mathbf{h}\,\mathbf{q} \tag{2.52}$$

and they are equivalent to the time-dependent Schrödinger equation (TDSE)

$$i\dot{\mathbf{c}} = \mathbf{h}\,\mathbf{c}, \tag{2.53}$$

when the complex coefficients $\mathbf{c} = (\mathbf{q} + i\mathbf{p})/\sqrt{2}$ are introduced. This analogy between Hamilton's equations and the TDSE was already recognised by Meyer and Miller in their original work on the MM mapping [32, 59]. However, in the MM case, the coefficients in Eq. (2.53) are normalized to 1, whereas in the non-interacting bosonic case they are normalized to the number of particles, $P = \mathbf{c}^{*}\mathbf{c}$. This results in the caveat that unique Fock-space states $|\mathbf{n}\rangle \equiv |\{n_1, \ldots, n_F\}\rangle$ do not have a unique parametrization in terms of **c** (or **q**, **p**) because an arbitrary phase can be added to every element of **c** without altering $|\mathbf{n}\rangle$, whereby different parametrizations of $|\mathbf{n}\rangle$ lead to different dynamics of the expansion coefficients. This fact is illustrated numerically in some of the examples in section 5.1 of chapter 5. Remacle and Levine had already encountered the non-uniqueness of Eq. (2.52, 2.53) to describe a *many-body* system of non-interacting electrons through a *single classical trajectory*,

but a workaround was not proposed and only applications to one-electron systems were discussed [98].

This caveat can be resolved, still for non-interacting bosons, by considering the time-evolution of the corresponding Wigner density function [99, 100]

$$\dot{\rho}_W(\mathbf{q},\mathbf{p}) = -2H^{(1)}(\mathbf{q},\mathbf{p}) \sin\left(\frac{\Lambda}{2}\right) \rho_W(\mathbf{q},\mathbf{p}), \tag{2.54}$$

where $\Lambda = \overleftarrow{\nabla}_q\overrightarrow{\nabla}_p - \overleftarrow{\nabla}_p\overrightarrow{\nabla}_q$, and $A_W \Lambda B_W \equiv \{A_W, B_W\}$ indicates the Poisson bracket. Under the quadratic Hamiltonian $H^{(1)}$ only the lowest order expansion of the sine function in Eq. (2.54) contributes and one immediately arrives at the classical Liouville equation for the density,

$$\dot{\rho}(\mathbf{q},\mathbf{p}) = \{H^{(1)}(\mathbf{q},\mathbf{p}), \rho(\mathbf{q},\mathbf{p})\}, \tag{2.55}$$

which delivers the *exact* phase-space dynamics of the non-interacting system. This density can be propagated as a swarm of classical trajectories matching the quantum mechanical initial conditions, which is the same as the Wigner classical approximation of Heller [35]. For non-interacting bosons this is not an approximation, but an alternative way to compute the exact dynamics of the system.

Up to now our discussion has been centered on bosonic particles and we have not made progress yet towards our primary goal, the classical mapping of fermionic particles. Let us return to the quantum mechanical problem and consider the time evolution of the single-particle density matrix elements $\langle \hat{a}_j^\dagger \hat{a}_i \rangle$

$$\frac{d}{dt}\langle \hat{a}_j^\dagger \hat{a}_i \rangle = i \left(\sum_k^F h_{kj} \langle \hat{a}_k^\dagger \hat{a}_i \rangle - \sum_l^F h_{il} \langle \hat{a}_j^\dagger \hat{a}_l \rangle \right). \tag{2.56}$$

Equation (2.56) is a closed expression: once the F populations $\langle \hat{n}_j \rangle$ and the $F(F-1)$ off-diagonal terms $\langle \hat{a}_j^\dagger \hat{a}_i \rangle$ are specified, their evolution follows uniquely. The key observation is that Eq. (2.56) is identical for bosons and for fermions. In other words, the same initial one-body density of non-interacting bosonic and fermionic systems has the same time evolution.

The important consequence for our purposes is that the original MM mapping in Eq. (2.51) also delivers the exact quantum dynamics of non-interacting Hamiltonians for many-body fermionic systems *once the initial one-body density matrix of the fermionic state has been mapped onto the corresponding phase-space density in Eq. (2.55)*. This result will be illustrated with various numerical examples in chapter 5. Note that we have made no attempt to include the anti-symmetry of the fermions through a Jordan-Wigner transformation, [68] nor to limit the maximum occupation of the orbitals with a spin mapping (SM) model [31, 60]. As is known [69–71], the mappings based on those concepts do not deliver the *exact* dynamics in the non-interacting limit and, as we will show, they indeed perform poorly compared to the MM mapping, with and without interactions.

The exact dynamics in the non-interacting limit is reproduced as well by the LMM mapping, which is explicitly devised for fermions [69–72], but at the cost of doubling the size of the classical phase-space compared to the MM mapping. For the range of examples with interactions considered in this work, though, we could not see any significant advantage of the LMM over the MM mapping. It is worth mentioning, however, that the LMM has been developed for, and applied to, semiclassical initial value calculations, [69–71] whereas in this work we consider it in a fully linearized, classical context. For completeness, both the SM and LMM are described in the following sections.

2.4 Spin Mapping

The SM mapping has already been utilized as a classical analog for electronic degrees of freedom (DOF) for a finite set of electronic states [32, 33, 60, 101] and for interacting fermions [75]. One proceeds by first mapping the fermionic creation-annihilation operators to the angular momentum operators for spin $1/2$ degrees of freedom

$$\begin{aligned} \hat{c}_i &\mapsto \hat{\sigma}_{i,x} + i\hat{\sigma}_{i,y} \\ \hat{c}_i^\dagger &\mapsto \hat{\sigma}_{i,x} - i\hat{\sigma}_{i,y}, \end{aligned} \tag{2.57}$$

where $\hat{\sigma}_{i,z} = 1/2$ ($\hat{\sigma}_{i,z} = -1/2$) corresponds to the occupied (empty) $i-th$ one-particle state. The classical Hamiltonian function (for non-interacting particles) without Jordan-Wigner transformation (JWT) reads

$$\begin{aligned} H_{\mathrm{SM}}^{(1)}(\sigma_x, \sigma_y, \sigma_z) = &\sum_i h_{ii} \left(\sigma_{z,i} + \frac{1}{2} \right) \\ &+ 2 \sum_{i>j} h_{ij} \left(\sigma_{x,i}\sigma_{x,j} + \sigma_{y,i}\sigma_{y,j} \right). \end{aligned} \tag{2.58}$$

with classical equations of motion [60]

$$\frac{d\boldsymbol{\sigma}_i}{dt} = \frac{\partial H(\boldsymbol{\sigma}_i)}{\partial \boldsymbol{\sigma}_i} \times \boldsymbol{\sigma}_i \tag{2.59}$$

$$\boldsymbol{\sigma}_i = (\sigma_{x,i}, \sigma_{y,i}, \sigma_{z,i}). \tag{2.60}$$

On the other hand, the JWT [102] exactly maps a fermionic Hamiltonian to a spin-chain Hamiltonian that yields matrix elements with the correct fermionic phase. This transformation is also the key ingredient involved in the description of fermions in second-quantization within the MCTDH method [103, 104]. Through JWT, the anti-symmetry of the fermionic quantum-mechanical operators is transformed into an equivalent form based on spin-$1/2$

degrees of freedom,

$$\hat{c}_i^\dagger \to \prod_{k=1}^{i-1} \hat{S}_k \cdot \hat{\sigma}_i^+ \tag{2.61}$$

$$\hat{c}_i \to \prod_{k=1}^{i-1} \hat{S}_k \cdot \hat{\sigma}_i^- \tag{2.62}$$

with $S_k = \exp(i\pi\hat{n}_k)$. Here, $\hat{\sigma}_i^\pm$ are spin-$1/2$ ladder operators and $\hat{S}_k$ are sign-change operators acting locally on index k such that $\hat{S}_k|0_k\rangle = |0_k\rangle$; $\hat{S}_k|1_k\rangle = -|1_k\rangle$, and the spin states are used to indicate occupation: $|\downarrow_k\rangle \to |0_k\rangle$; $|\uparrow_k\rangle \to |1_k\rangle$. The sign-change operators can also be written as $\hat{S}_k = 1 - 2\hat{n}_k$, where $\hat{n_k} = \hat{\sigma}_k^+\hat{\sigma}_k^-$. This substitution together with the JWT relations (2.61) and the SM result precisely in the original MW mapping for fermionic Hamiltonians (cf. Eqs. 2.10 and 2.13 in Ref. 31). Thus, it seems reasonable to combine the SM with the JWT, which introduces phase operators $\hat{S}_k = \exp(i\pi\hat{n}_k)$, and then introduce the corresponding classical functions. These can take the form

$$S_k = (1 - 2n_k), \tag{2.63}$$

where the occupation $n_j(\vec{x})$ depends on the explicit classical variables $\vec{x}$ used in the corresponding mapping. The SM+JWT classical analog Hamiltonian for non-interacting particles then takes the form

$$\begin{aligned} H^{(1)}_{\text{SM+JWT}}(S_x, S_y, S_z) = &\sum_i h_{ii}\left(S_{z,i} + \frac{1}{2}\right) \\ &+ 2\sum_{i>j}\prod_{k=j+1}^{i-1} h_{ij}(1 - 2n_k)\left(S_{x,i}S_{x,j} + S_{y,i}S_{y,j}\right). \end{aligned} \tag{2.64}$$

Comparing Eq. (2.64) with the relation 2.10 in Ref. 31 shows that this procedure is equivalent to the original Miller-White mapping.

2.5 Li-Miller Mapping

The Li-Miller mapping (LMM) uses the concept of quaternion operators to capture the properties of second-quantized fermionic operators and to construct a classical mapping for them [69–71]. This results in a mapping where each fermionic DOF is mapped to two classical DOFs (two position-momentum pairs). The LMM has been introduced in the context of semi-classical initial-value representation calculations mechanics [69–71], whereas here we use it in a fully linearized context. Recent applications of a classical analog to quantum transport of fermions have modified the LMM mapping in a way that makes it

possible to describe a few extra types of fermionic operator products, and termed it complete quasicalssical mapping (CQM) [72]. In our applications, the LMM and CQM maps are equivalent. The corresponding Hamiltonian reads

$$H^{(1)}_{\rm LMM}(\mathbf{p}_x,\mathbf{q}_x,\mathbf{p}_y,\mathbf{q}_y)=\frac{1}{2}\left(\mathbf{q}_x^{+}\,\mathbf{h}\,\mathbf{p}_y-\mathbf{q}_y^{+}\,\mathbf{h}\,\mathbf{p}_x\right)+\gamma{\rm Tr}[\mathbf{h}]. \tag{2.65}$$

Furthermore, the corresponding Hamilton equations of motion for a non-interacting Hamiltonian is written as,

$$\begin{aligned}\dot{\mathbf{q}}_x&=-\mathbf{h}\,\mathbf{q}_y;\quad \dot{\mathbf{p}}_x=-\mathbf{h}\,\mathbf{p}_y\\ \dot{\mathbf{q}}_y&=\mathbf{h}\,\mathbf{q}_x;\quad \dot{\mathbf{p}}_y=\mathbf{h}\,\mathbf{p}_x.\end{aligned} \tag{2.66}$$

This indicates that each site of LMM requires 4 variables, which is two times more than the variables used in the MM mapping. The extra variables used in LMM are for fermionic properties. In chapter 5, we compare the MM to the LMM in different systems. We aim to show the extra variables used in the LMM improve little when describing fermionic dynamics.

2.6 Initial space density

Two equivalent propagation strategies are available for non-interacting systems: (i) The initial fermionic Fock-space state is mapped onto a corresponding phase-space distribution, Eq. (2.55), which can then be conveniently discretized as N phase-space trajectories, each evolving as $2F$ coupled Hamilton's equations. (ii) The one-body density matrix corresponding to the initial fermionic state is propagated according to the F^2 coupled differential Eqs. (2.56). The former strategy is our working approximation for interacting Hamiltonians. The latter strategy, propagating the one-body density matrix, becomes essentially equivalent to solving the full quantum-mechanical problem once interactions are included, and we do not consider approximations along that line.

Using the relations (2.50) with the single-particle density matrix elements $\langle\hat{a}_j^{\dagger}\hat{a}_i\rangle$ and equating expectation values to classical phase-space averages, one can write the relation

$$\begin{aligned}\langle\hat{a}_j^{\dagger}\hat{a}_j\rangle&=\frac{1}{2}\int\left(\,p_j^2+q_j^2-2\gamma\,\right)\rho(\mathbf{q},\mathbf{p})\;\;d_q^F\;\;d_p^F\\ \langle\hat{a}_j^{\dagger}\hat{a}_i\rangle&=\frac{1}{2}\int\left(\,p_jp_i+q_jq_i-ip_jq_i+iq_jp_i\,\right)\rho(\mathbf{q},\mathbf{p})\;\;d_q^F\;\;d_p^F\end{aligned} \tag{2.67}$$

between the quantum mechanical matrix element of the one-body density and the classical phase-space average of position and momenta for the MM mapping. The phase-space

density can be represented by a discrete set of N phase-space points $(\mathbf{p}^{(k)}, \mathbf{q}^{(k)})$,

$$\langle \hat{a}_j^\dagger \hat{a}_j \rangle = \frac{1}{N} \sum_{k=1}^{N} \frac{1}{2} \left(p_j^{(k)2} + q_j^{(k)2} - 2\gamma \right) \tag{2.68}$$

$$\langle \hat{a}_j^\dagger \hat{a}_i \rangle = \frac{1}{N} \sum_{k=1}^{N} \frac{1}{2} \left(p_j^{(k)} p_i^{(k)} + q_j^{(k)} q_i^{(k)} - i p_j^{(k)} q_i^{(k)} + i q_j^{(k)} p_i^{(k)} \right).$$

It is more convenient to discuss the sampling of initial conditions in terms of the corresponding action-angle variables, [32, 97] whose relation to (q_j, p_j) follows compactly as

$$q_j + i p_j = \sqrt{2(n_j + \gamma)} e^{i\phi_j}. \tag{2.69}$$

Using Eq. (2.69), Relation (2.68) becomes

$$\langle \hat{a}_j^\dagger \hat{a}_j \rangle = \frac{1}{N} \sum_{k=1}^{N} n_j^{(k)} \tag{2.70a}$$

$$\langle \hat{a}_j^\dagger \hat{a}_i \rangle = \frac{1}{N} \sum_{k=1}^{N} \sqrt{(n_j^{(k)} + \gamma)(n_i^{(k)} + \gamma)} e^{i(\phi_i^{(k)} - \phi_j^{(k)})}. \tag{2.70b}$$

Let us consider first the simple case that the initial state in Fock space corresponds to a single configuration with one single electron, $|j\rangle \equiv |0_1, \ldots, 1_j, \ldots 0_F\rangle$, in the occupation number representation. In this case $\langle \hat{a}_j^\dagger \hat{a}_j \rangle = 1$ and all other matrix elements of the one-body density matrix are zero. Therefore the one-body density matrix can be mapped to a single phase-space point with action variables $n_j = 1$, $n_l = 0$ for $l \neq j$ and all angle variables $\phi_m = 0$. Integrating the corresponding classical trajectory is of course equivalent to solving the corresponding TDSE, Eq. (2.53). Another illustrative example is the single-electron case where the initial state is a linear superposition of configurations

$$|\Psi\rangle = \sum_{j=1}^{F} C_j |j\rangle \tag{2.71}$$

where C_j are complex expansion coefficients and $|j\rangle$ are the single-electron configurations defined above. Now, by setting $\gamma = 0$, Eqs. (2.70) can be fulfilled simultaneously by a single phase-space point where the action-angle variables are chosen such that $C_j = \sqrt{n_j} e^{i\phi_j}$. This situation is analogous to setting $\gamma = 0$ in the original MM mapping for electronic states, which then reverts to an Ehrenfest model with a single trajectory. If $\gamma \neq 0$, the one-body density of the single-electron state (2.71) cannot be described, in general, by a single phase-space point according to Eqs. (2.70).

A more useful case corresponds to a single-configuration many-body state of the form $|1_1, 1_2, \ldots, 1_m, 0_l, \ldots, 0_F\rangle$, for example a Hartree-Fock approximation of the ground electronic state or an excited state that can be initially well described as a single configuration.

	ϕ_1	ϕ_2	ϕ_3
Trj 1	0	$\pi/4$	$3\pi/4$
Trj 2	0	$3\pi/4$	$\pi/4$
Trj 3	0	$5\pi/4$	$7\pi/4$
Trj 4	0	$7\pi/4$	$5\pi/4$

Table 2.1. In a system with 3 DOFs, an instance is presented by solving Equation (2.68).

For such a state, the one-body density matrix is diagonal with $\langle \hat{a}_j^\dagger \hat{a}_j \rangle = n_j$. Independently of the choice of γ, it is clearly impossible to fulfill, e.g., that

$$\langle \hat{a}_1^\dagger \hat{a}_1 \rangle = \langle \hat{a}_2^\dagger \hat{a}_2 \rangle = 1 \tag{2.72a}$$

$$\langle \hat{a}_2^\dagger \hat{a}_1 \rangle = 0 \tag{2.72b}$$

with one single phase-space point. One can think of different ways to sample initial conditions that fulfill Eqs. (2.70), for example by introducing a specific number N of initial phase-space points and then solving Eqs. (2.70) for all unknown $n_j^{(k)}, \phi_j^{(k)}$ parameters. For instance, it is possible to set all $n_j^{(k)}$ of each k-point equal to the corresponding spin-orbital populations, Eq. (2.70a), while the remaining angle variables of each k-point must then be determined such that the remaining sum of phases in Eq. (2.70b) vanishes. This corresponds to determining $F \times N$ unknowns for the corresponding set of $F(F-1)/2$ non-linear equations and it is not clear, *a priori*, what is the smallest number N of phase-space points needed to map a specific density. We have made no attempt to systematically solve Eq. (2.70b) for the angles of general initial states. We illustrate the concept with a simple example with $F = 3$ spin-orbitals and 2 particles, which will be considered later numerically. Starting with state $|1, 1, 0\rangle$, one needs at least $N = 4$ points (trajectories) to reproduce the corresponding one-body density matrix and one can easily verify that the angles in Table 2.1 result in the cancellation of the phase factors in Eq. (2.70b). Clearly, the choice of angles in Table 2.1 is not unique, only the angle differences between each DOF matter.

Alternatively to the discrete sampling just introduced, it is possible to perform a random sampling of the initial angle variables. For single-configuration initial states, where all off-diagonal matrix elements of the one-body density matrix are zero, this is the most straightforward way to determine initial conditions. The disadvantage is that one may end up propagating more classical trajectories than strictly needed. For systems with many single-particle states (orbitals) F, this is however a straightforward way to proceed, as compared to solving Eq. (2.70b) for some specific discretization N. In section 5.1, we numerically illustrate how, for non-interacting systems, both a small set of trajectories with initial angles chosen to fulfill Eq. (2.70b), and a randomly sampled ensemble with a larger number

of trajectories, yield the exact one-body dynamics of the system. In section 5.1, for interacting Hamiltonians, Eq. (2.55) is not equivalent to Eq. (2.54) and therefore the former does not reproduce the exact dynamics of the one-body density. Moreover, different classical phase-space distributions representing the same initial one-body density result in different time evolutions.

Finally, multi-configurational many-body states have, in general, a non-diagonal one-body density matrix that cannot be factorized. Because the off-diagonal elements are not necessarily equal to zero, the random sampling strategy cannot be applied, and one is left with the alternative of solving Eqs. (2.70) to determine the initial ensemble of phase space points. In this study, we focus instead on single-configuration initial states.

Chapter 3

Dynamics of molecules with fixed orientation inside cavity

Ground state reaction in cavity with vibronic strong coupling (VSC) has been developed recently in polaritonic chemistry since the pioneering demonstrations of Rabi splitting in the infrared domain in Fabry-Perot configurations [8, 94, 105]. Due to its potential to modify and ultimately manipulate the mechanisms and thermal reaction rates through the vaccum fields of cavities [106–108]. Besides important breakthroughs in the linear and non-linear spectroscopy of VSC systems [106–109], the more spectacular results remain the experiments reporting the modification of chemical rates in cavities by the Ebbesen group and others [15–17, 110–112]. These experiments have triggered the proposal of several theoretical models to explain how the cavity modifies the ground electronic state structure [113] and spectroscopy [114] and, more recently, how it modifies reaction rates [18–20, 28, 83, 92, 93]. Theoretical models based on the Grote-Hynes theory [115] predict the suppression of the transmission coefficient with increasing cavity coupling due to increased friction at the top of the reaction barrier [19, 20, 83]. How cavities can enhance chemical reactions [17, 29], how sharp resonances of the cavity with vibrational modes affect the mechanism [16, 17], and how these effects survive in the collective VSC regime, have remained poorly understood questions.

In this chapter, we theoretically demonstrate that both enhancement and suppression of reaction rates are possible within a cavity for realistic chemical processes. The molecules are kept at a fixed orientation with respect to the polarization direction of the cavity mode. We first focus on the coupling of the μ_x dipole component to the cavity polarizaton. Although we rely on classical rate theory [91], we note that tunneling correction for hydrogen abstraction reactions at 300 K result in variations of the rate within the same order of magnitude [116]. For reactions involving heavier elements, quantum corrections to the rates are even more insignificant. Along these lines, there is no reason to assume, a priori, that photonic mode

with frequencies similar to the atomic vibrations, and in thermal equilibrium, shall result in significant quantum effects that affect the general conclusions derived from classical rate theories for VSC systems. This does not exclude situations where quantum effects may be important for quantitative descriptions of cavity-modified rates in reactions involving light atoms, as it is sometimes the case for rates outside cavities [116–118].

3.1 HONO inside cavity

3.1.1 isomerization of HONO

The simplicity of the unimolecular reaction mechanism in HONO makes it an ideal benchmark system to understand how dynamical cavity effects can modify chemical rates as compared, e.g., to bimolecular reactions in solution [16, 119]. We base our study on the CCSD(T)-quality *ab initio* potential energy surface (PES) of Richter et al. [120], which features a reaction barrier height of about 0.51 eV (49 kJ/mol) and where the *trans* isomer is 11 meV more stable than the *cis* one. Quantum dynamics studies of the HONO isomerization triggered by strong laser pulses have been based on this PES [121, 122]. Despite its simplicity, this chemical reaction constitutes a fully coupled and rich dynamical system. Similarly to other isomerization reactions, e.g. involving hydrocarbons [89, 123, 124], it takes place in the underdamped regime. A corresponding diagram illustrating the reaction coordinate and the *cis* and *trans* configurations is found in Fig. 3.1 in the form of a Newman diagram with the central N-O bond perpendicular to the plane of the paper and at the origin of the (x, y)-plane.

3.1.2 Cavity Hamiltonian of HONO inside cavity

In section 2.1 of chapter 2, the Hamiltonian is derived from the Coulomb-gauge light-matter interaction Hamiltonian by taking the long wave approximation followed by a unitary transformation to the length form [18, 79, 125]. To describe how the isomerization reaction is affected by the cavity mode, we start from a classical analog of Hamiltonian for a molecular ensemble coupled to one cavity mode

$$H = \sum_{l=1}^{N} H_{mol}^{(l)} + H_{cav} \tag{3.1}$$

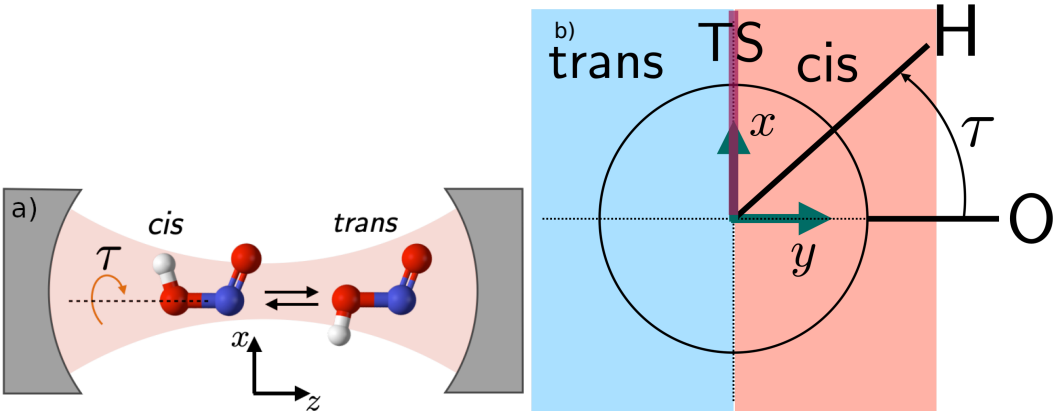

Figure 3.1. a) *cis-trans* isomerization reaction in HONO. The axes indicate the body-fixed frame of the molecules in the simulation. The presence of the cavity is indicated schematically and is not to scale. HONO is characterized by 6 vibrational coordinates: 3 stretching modes, O−H, O−N and N=O; 2 bending modes, H−O−N and O−N=O; 1 torsion mode τ, the isomerization reaction coordinate. b) Newman diagram of the HONO molecule showing the definition of the body-fixed axes. The hydrogen atom is on the front side, the terminal oxygen atom is on the back, and the remaining oxygen and nitrogen atoms lie at the origin of the diagram along the perpendicular z-axis. The (y, z)-plane is determined by the ONO atoms, and the reaction coordinate τ corresponds to the dihedral rotation of the H-atom around the z-axis and on the (x, y)-plane. Its origin is set at the minimum energy configuration of the *cis* region. The transition state lies at about 90 and by symmetry also at about 270 degrees.

with

$$H_{mol}^{(l)} = \sum_{j_l=1}^{F} \frac{P_{j_l}^2}{2M_{j_l}} + V(R_{1_l} \dots R_{F_l}), \tag{3.2}$$

$$H_{cav} = \frac{1}{2}\left[p_{cav}^2 + \omega_{cav}^2 \left(q_{cav} + \frac{\boldsymbol{\lambda}}{\omega_{cav}} \cdot \sum_{l=1}^{N} \hat{\boldsymbol{\mu}}^{(l)}\right)^2\right]. \tag{3.3}$$

$V(R_{1_l} \dots R_{F_l})$ denotes the ground electronic state potential energy surface (PES) of the l-th molecule with momenta P_{j_l} and positions R_{j_l}. Hence, the Born-Oppenheimer (BO) approximation is assumed within each molecule, and $\boldsymbol{\mu}^{(l)} \equiv \boldsymbol{\mu}^{(l)}(R_{1_l} \dots R_{F_l})$ is the permanent dipole vector of the l-th molecule.

3.1.3 Dipole of HONO

In this chapter, the molecules are kept at a fixed orientation with respect to the polarization direction of the cavity mode(Fig. 3.1a). In this way, we focus on the coupling of a specific dipole component to the cavity polarization. The permanent dipole moment of HONO

has been evaluated at the MP2 level of theory using the atomic basis 6-311g++(d,p) and is described as a function of the reaction coordinate or the torsion coordinate. In this treatment, we approximate the dipole strongly depends on the reaction coordinate, and neglect the modulation of the dipole due to other internal coordinates.

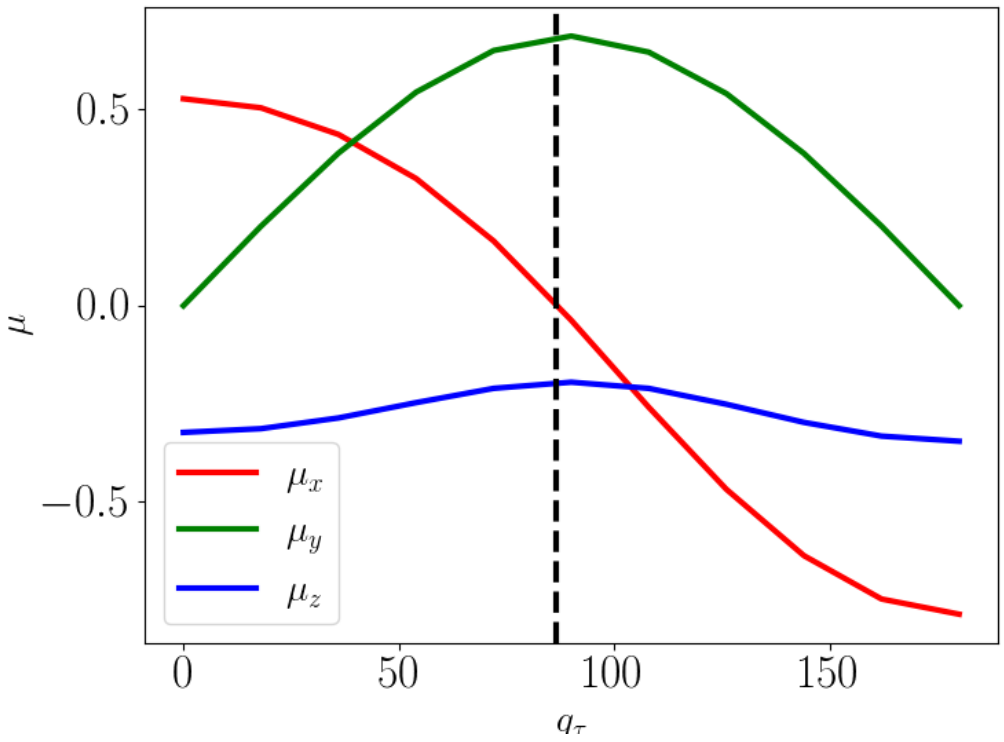

Figure 3.2. Permanent dipole of the HONO molecule in atomic units as a function of the torsion coordinate τ. The axes are referred to as the molecular frame axis in Fig. 3.1a.

3.1.4 Reactive flux rate of HONO isomerization

The *cis-trans* reaction rate is described with the reactive flux method for the classical rate constant [87–89, 123, 124]

$$K(t) = x_{cis}^{-1} \langle \dot{\tau}(0)\, \delta[\tau(0) - \tau^{\ddagger}]\, \theta[\tau(t)] \rangle, \tag{3.4}$$

where x_{cis} is the equilibrium fraction of HONO at the *cis* geometry, $\dot{\tau}(0)$ is the initial velocity of a phase-space point perpendicular to the dividing surface between reactants and products, and $\tau^{\ddagger}$ is the torsion angle corresponding to the transition state geometry. The derivation of the reactive flux method is shown in section 2.2 of chapter 2. The brackets indicate the canonical ensemble average over trajectories, where we considered a temperature of 300 K throughout. The Heaviside function $\theta[\tau]$ is defined to be one for the *trans* configurations,

and zero otherwise. The exact rate is obtained when $K(t)$ reaches the plateau value. As mentioned in section 2.2 of chapter 2, we choose the same dividing surface between *cis* and *trans*. Hence, a consistent K_{TST} is expected, which is shown in fig 3.3. The modification of the reactivity is reflected by the transmission coefficient, κ.

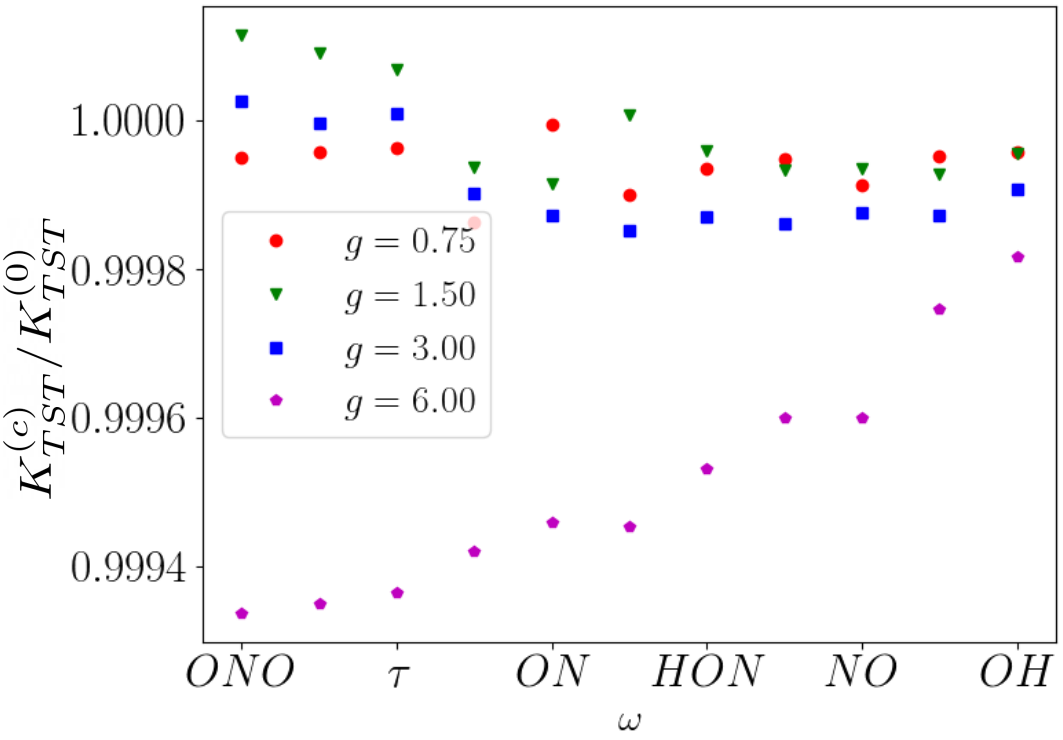

Figure 3.3. The ratio of $K^{(c)}_{TST}$ and $K^{(0)}_{TST}$ is presented. $K^{(0)}_{TST}$ is transition state theory rate outside the cavity while $K^{(c)}_{TST}$ is the transition state theory rate inside the cavity. K_{TST} is calculated using Eyring's equation. The frequencies for ω_{cav} are taken to be resonant with the harmonic vibrational frequencies of HONO.

3.2 x-polarized

3.2.1 Single molecule inside cavity

We first consider a single HONO molecules coupled to a cavity mode which is x-polarized with respect to the molecular frame. Under this circumstance, the largest variation of the dipole moment occurs at the transition state (TS) of the reaction coordinate i.e. $\tau^{\ddagger} \approx \pi/2$(shown in fig 3.2). Outside the cavity, $\kappa^{(0)} \approx 0.23$ at 300 K, the plateau value of the black curve in Fig. 3.4a. This low transmission can be explained by that the activated trajectories have a slow intra-molecular vibrational energy redistribution (IVR) rate in the

underdamped regime. As the HONO molecule is inside the cavity, the plateau value stabilizes at a larger total transmission $\kappa^{(c)}$ is observed, which is shown in the red, blue and green curves of Fig. 3.4a. The increasing $\kappa^{(c)}$ implies that the cavity enhances the chemical reaction, which is illustrated by the ratio of the total transmission coefficient compared to $\kappa^{(0)}$, i.e. R. This is summarized by the red trace in Fig 3.4c. In addition, one observes R firstly increases as coupling strength, g, increases. This enhancing reaction rate can be explained by our theoretical framework: the cavity provides an extra energy redistribution pathway for a system with a low-friction reaction coordinate. However, as the cavity coupling to the torsion coordinate further increases, a turning point is reached for $g > 3$ V/nm. The amount of recrossing at the barrier keeps increasing as well, thus finally reverting the trend and decreasing the transmission again. This has been pointed out as the Kramers turning point [115], which, e.g., was predicted long ago for the isomerization of cyclohexane as a function of solvent viscosity [124]. Figure 3.4a illustrates its origin in the quick drop of $\kappa^{(c)}(t)$ at short times for the strongest cavity coupling.

3.2.2 Single molecule inside cavity with bath mode

We have already discussed the case of gas-phase HONO and how its reaction rate is influenced by the presence of a cavity. Now, we want to explore the effect of the cavity on the reaction rate of HONO in the solution phase, which requires introducing an external bath. By coupling HONO to an external bath, the overdamped regime of the Grote-Hynes theory is achieved. Figure 3.4b shows how now $\kappa^{(c)}(t)$ and $\kappa^{(0)}(t)$ quickly reach their plateau value within a few tens of femtoseconds, meaning that activated trajectories visit the region of the TS only once or twice. Since the plateau is reached quickly, the cavity's influence is limited to a short period near the top of the barrier, where it can enhance the recrossing rate and lower the transmission coefficient As illustrated in Fig.3.4c by the green trace, now $R < 1$: the chemical rate in the cavity is reduced for all coupling strengths. This is the regime captured in Refs 19, 20, 83.

3.2.3 Cavity with various cavity frequency

In this section, we focus on the case of sharp resonant effects, which occur when a specific cavity frequency causes a significant modification of the chemical rates. The resonance between the cavity and vibrational modes of the molecule can affect the outcome of reactive events, as shown by trajectory calculations. However, the connection between this resonance and the actual change in chemical rates is still unknown [82, 126]. Our simulations of the transmission coefficient in the underdamped, slow IVR regime reveal sharp resonances in the rate constant effect as a function of ω_{cav}. As already discussed, in this regime the ef-

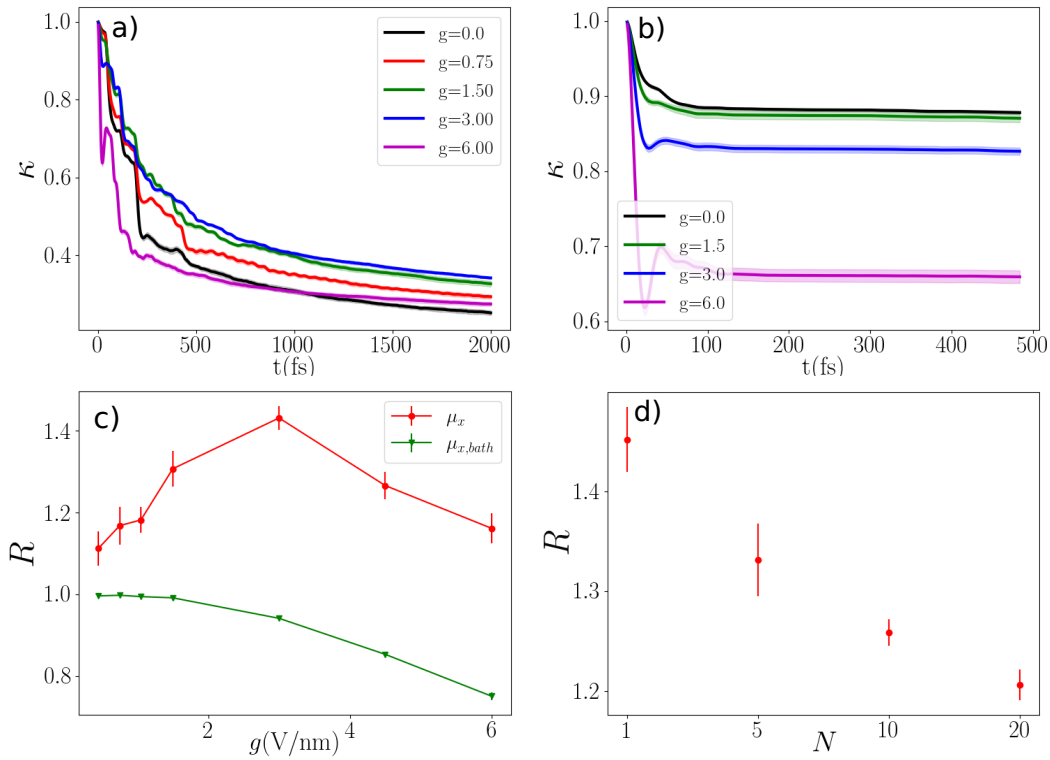

Figure 3.4. a) Transmission coefficient $\kappa^{(c)}(t)$ for various cavity-coupling strengths g (V/nm) for $N = 1$, $\omega_{cav} = 640$ cm-1 and the cavity polarization aligned with HONO's x-axis. The asymptotic values have been obtained by extrapolating the last 1500 fs with an exponential decay and read $\kappa = (0.23, 0.27, 0.30, 0.33, 0.27)$ for the coupling strengths $g = (0, 0.75, 1.5, 3.0, 6.0)$, respectively. b) same as a) but with the HONO molecules coupled to a bath. The shaded area on top of the solid lines indicates the standard deviation of the average over trajectory runs. c) Asymptotic $R = \kappa^{(c)}/\kappa^{(0)}$ for the curves in a) (red) and b) (green). d) R for increasing number of molecules at constant total polaritonic coupling.

fect of the cavity is to introduce extra energy redistribution pathways, whereby the effect at short times while passing the TS barrier region is not so important. Thus, when the cavity is resonant with a vibrational mode that happens to be strongly coupled to the reaction coordinate, the enhancement of the rate is more prominent. As seen in Fig. 3.5, $R \approx 1.8$ when ω_{cav} is resonant with the O-N stretching mode at 900 to 1000 cm^{-1}. This can be connected to the peak observed in the spectrum of the velocity-velocity auto-correlation function, which will be discussed in the next chapter.

3.2.4 Collective regime with fixed rabi splitting

In experiments reporting modifications of chemical rates in Fabry-Perot configurations, a collective of molecules are prepared inside the cavity. Due to the computational cost, theoretical studies often assume a single molecule with ultra-strong coupling to the cavity to

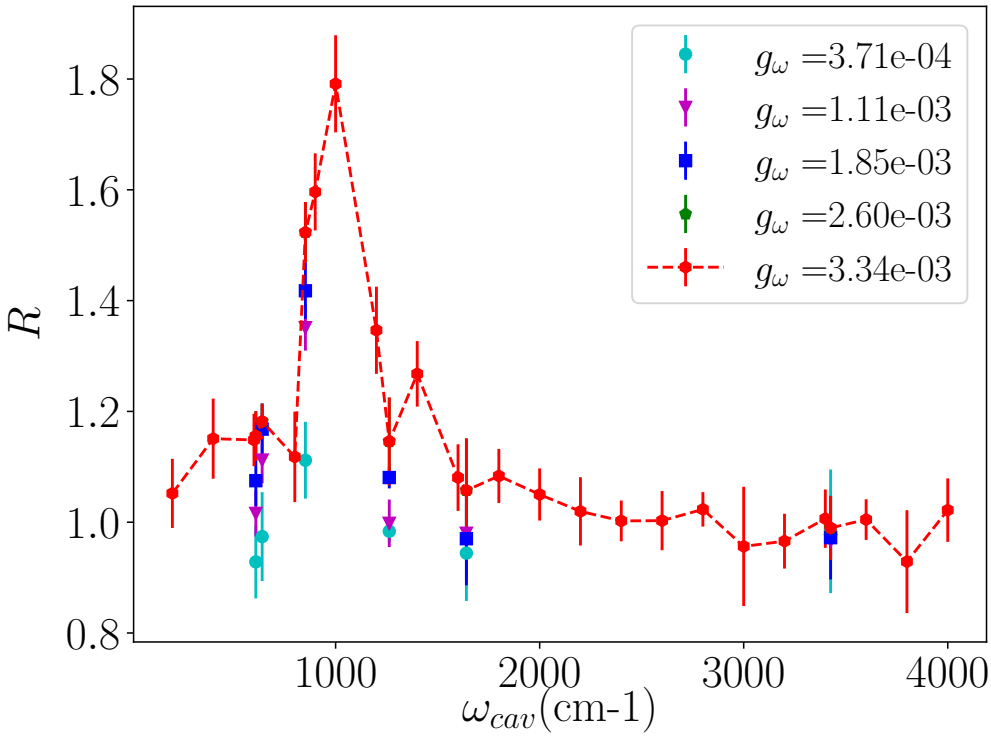

Figure 3.5. Rates ratio R for various coupling strengths $g_\omega = g\mu_x^\ddagger/\omega_{cav}$ as a function of ω_{cav}, where $\mu_x^\ddagger$ is μ_x at the TS. Vertical bars represent standard deviations over the run trajectories. For $g_\omega = 3.34\text{E}{-}3$, ω_{cav} is scanned in steps of 200 cm^{-1} and the red dashed line is meant to guide the eye. For the other coupling strengths ω_{cav} is chosen to be resonant with the fundamental vibrational modes of HONO: $\omega_{ONO} = 609$, $\omega_\tau = 640$, $\omega_{ON} = 852$, $\omega_{HON} = 1263$, $\omega_{NO} = 1641$, and $\omega_{OH} = 3426$ cm^{-1}.

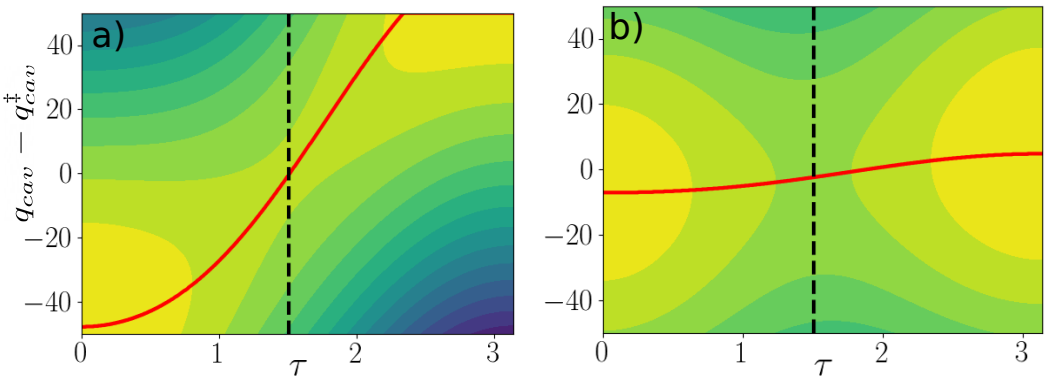

Figure 3.6. Potential energy surface cut for a) 1 and b) 100 HONO molecules as a function of the reaction coordinate τ and the cavity displacement $q_{cav} - q^{\ddagger}_{cav}$ ($q^{\ddagger}_{cav}$ is the cavity displacement at the TS). For $N = 1$ the light-matter coupling is $g = 8$ V/nm. The cavity coupling in b) is scaled by $1/\sqrt{N}$ to keep a constant overall light-matter interaction. The color levels start at 0 for the lightest tone and increase in steps of 0.2 eV. The red line indicates the minimum energy path. The vertical dashed line separates the *cis* and *trans* configurations.

reach the same Rabi splitting reported in experiments. The gap between a single molecule and a collective molecules inside the cavity with the same Rabi splitting is still an open question. To shed some light on this issue, we have performed trajectory calculations of the transmission coefficient for an increasing number of molecules N coupled to the cavity, again without an extra bath. The coupling per molecule is scaled as usual by a factor $N^{-1/2}$ as a means to keep the overall light-matter coupling constant [127]. Starting from $N = 1$, $g = 1$ V/nm, and $\omega_{cav} = 852$ cm-1, one sees in Fig. 3.4d how, for increasing N, the cavity effect gradually fades away. Responsible for the gradual trend $R \to 1$ is the decoupling of the reaction coordinate from the cavity displacement with increasing N, as seen by comparing the curvature of the minimum energy path (MEP) in Figs. 3.6a, $N = 1$, and 3.6b, with $N = 100$. This reduction of the MEP curvature as N increases, and thus the reduced friction caused by the cavity, implies that in the large N limit the cavity is not able to "cage" the TS and induce a decrease of the transmission coefficient through this mechanism. This indicates that with the fixed Rabi splitting, a single molecule inside the cavity describes a significantly different PES from a collective of molecules inside the cavity, which may lead to different mechanisms of dynamics.

3.3 Other polarized direction

Following the calculations in the previous section, a single HONO inside a cavity with either y or z-polarized is performed. Fig. 3.7 shows R as a function of cavity frequency with either

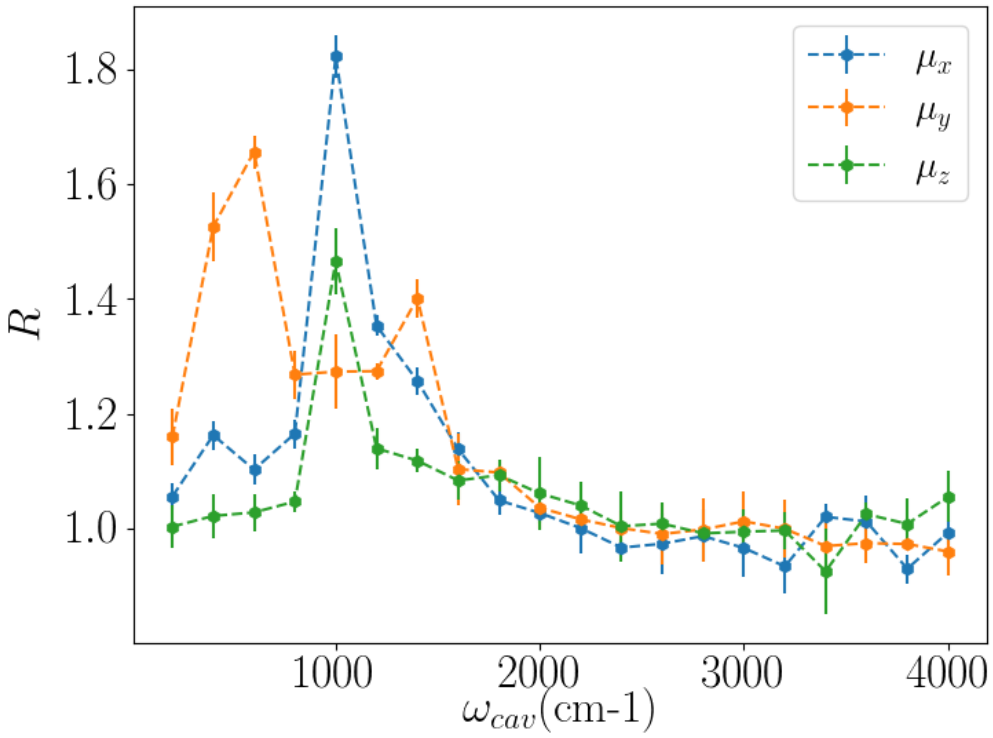

Figure 3.7. Rates ratio R as a function of ω_{cav} with fixed $g_\omega = 3.34\text{E}{-3}$. Vertical bars represent standard deviations over the run trajectories.

y or z-polarized. Compared with x-polarized, the enhancement of the rate is prominent when ω_{cav} is resonant with the torsion mode of the reaction coordinate at 600 cm^{-1} and 1200 cm^{-1} when the cavity is y-polarized. On the other hand, as the cavity is z-polarized, the enhancement of the rate is prominent at 1000 cm^{-1} which is similar with the x-polarized results. The different results between the three polarized cavities can be attributed to the spectrum of the dipole-dipole auto-correlation function, which will be discussed in chapter 4. We stress that the enhancement of the reaction rate is highly correlated to the polarized direction of the cavity. In experiments, molecules can freely orientate in solutions. The actual dipole component coupled to the cavity varies as time evolves. In the next chapter, we will focus on molecules, which randomly orientate inside the cavity.

3.4 Conclusion

In this chapter, we theoretically demonstrate that both enhancement and suppression of reaction rates are possible within a cavity for realistic chemical processes. The molecules are kept at a fixed orientation with respect to the polarization direction of the cavity mode. We first focus on the coupling of the μ_x dipole component to the cavity polarization. The

modification of the reaction rate is connected to the interaction between the reaction coordinate and the surroundings. The weak(strong) interaction leads to the reaction occurring at under-damped(over-damped) regime, which enhances(suppresses) the reaction rate. In the under-damped regime, sharp resonant effects are observed with different polarized cavities. We emphasize that the enhancement of the reaction rate is relevant to the dipole component coupled to the cavity.

Chapter 4

Dynamics of multiple molecules with random orientation inside cavity

In this chapter, we extend our study in chapter 3, which focuses on a single HONO molecule with fixed orientation to ensembles of freely rotating HONO molecules in the gas phase (shown in fig 4.1) and explore the collective effects on the reaction rate. We choose a coupling strength such that an effect is seen for one single molecule, but such that the Rabi splitting is still buried within the linewidth of the molecular infrared absorption. Under such conditions, we investigate the scenario where the addition of molecules with a fixed coupling strength leads to the appearance of vibropolaritonic bands. We aim to demonstrate that the resonant interaction of the activated molecule with the vibropolaritonic bands has the same effect as the direct interaction of a single molecule with the cavity mode. Moreover, we show in detail how their orientation of the activated and non-activated molecules may differ for optimal interaction with the cavity, and the resonance may frequency may shift for the activated molecule due to its higher energy content. To improve computational efficiency of simulating an ensemble molecules inside the cavity, OpenMM package is used. More details of OpenMM can be found in Appendix A.

4.1 HONO cluster inside a cavity

4.1.1 HONO cluster

As mentioned in section 2.2 of chapter 2, thermally activated molecules passing the top of the barrier is a rare event. Consider N HONO molecules inside the cavity, 1 HONO is an activated molecule(AM) while $N-1$ HONO molecules are non-activated molecules(NAMs) when preparing a set of trajectories(shown in fig 4.1). We assume the reaction occurs in the gas phase, which means the interactions between HONO molecules are neglected. Since we

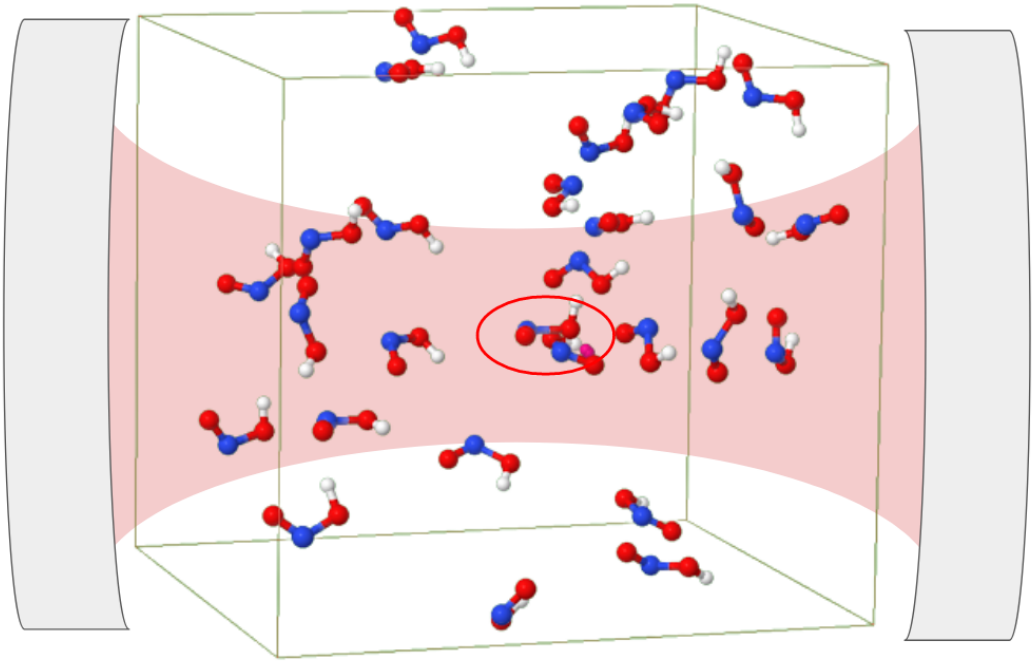

Figure 4.1. HONO molecules in a cavity. One activated molecule (Red circle) is presented, while the others are non-activated molecules. The presence of the cavity is indicated schematically and is not to scale.

investigate the reaction rate in an underdamped regime, an enhancement of the reaction rate is expected as N increases with a fixed coupling strength based on the results in chapter 3.

4.1.2 Dipole of HONO

In this chapter, we consider HONO molecules freely orientate inside the cavity. Also, we aim to include the contribution of all the nuclei coordinates to the dipole. To reduce computational cost of simulations, we use a simple partial charge model of the dipole(fig 4.2) for its three components that agrees qualitatively well with calculated cuts of the *ab initio* dipole surfaces(fig 3.2).

In the partial charge model, the dipole of a molecule can be described as a sum of dipoles contributed by atoms of the n-th molecule, which is expressed as:

$$\boldsymbol{\mu}_{\text{mol}}^{(n)} = \sum_i \delta_i \boldsymbol{R_i}^{(n)}, \tag{4.1}$$

where δ_i and $\boldsymbol{R_i}$ represents the partial charge and the position of atom i, respectively. And index i runs over all atoms of the molecule. Note that $\boldsymbol{\mu_{mol}}$ and $\boldsymbol{R_i}$ are vectors. If the system

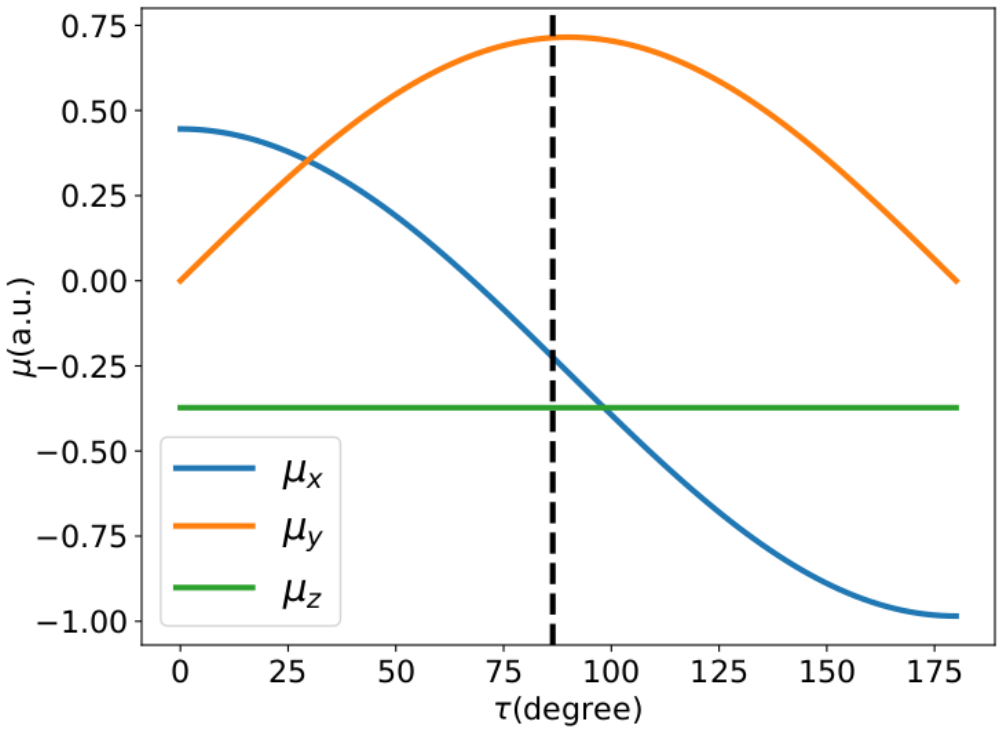

Figure 4.2. Under cartesian coordinates, three dipole components are plotted as a function of the reaction coordinate.

includes more than one molecule, the dipole of the system is expressed by:

$$\boldsymbol{\mu}_{\text{sys}} = \sum_{n} \boldsymbol{\mu}_{\text{mol}}^{(n)}. \tag{4.2}$$

The partial charge of HONO is listed in Table 4.1. O1 represents the oxygen atom connected with the hydrogen and the nitrogen atom while O2 represents the other oxygen atom connected with the nitrogen atom only.

The three spatial directions of the dipole in the body-fixed molecular frame along the reaction coordinate τ are shown in Fig 4.2. The modulation of the μ_z component is very small as a function of τ and its largest modulation occurs instead in the stretching and bending modes of the molecular skeleton.

Table 4.1. Partial charge of HONO molecule

	H	O1	N	O2
partial charge (a.u.)	0.401	-0.373	0.103	-0.131

4.2 Cavity effect in collective regime with fixed coupling strength

We perform 3 different cases describing the coupling between the cavity and the HONO molecules. The first case is the molecules are kept at a fixed orientation with respect to the polarization direction of the cavity mode. In this way, we focus on the coupling of the μ_x dipole component to the cavity polarization. The second case follows the first one, but we focus on the coupling of the μ_y dipole component to the cavity polarization, instead. The third case is the molecules randomly orientate at every time step. The actual coupling of the dipole component to the cavity polarization is a linear combination of μ_x, μ_y, μ_z, which should be evaluated based on the orientation of each molecule.

In fig 4.3a, we demonstrate transmission coefficients as a function of N in which the HONO molecules randomly orientate. Outside the cavity, $\kappa^{(0)} \approx 0.23$ at 300 K is the plateau value of the black curve. This relatively low transmission is caused by a slow rate of intra-molecular vibrational energy redistribution (IVR) of the activated trajectories in the underdamped regime, which has been mentioned in chapter 3. For a single molecule ($N = 1$) inside the cavity with fixed $g = 0.4$ V/nm, one sees the plateau values stabilizes at a larger value. As N increases, $\kappa^{(c)}$ is further enhanced according to the orange, blue curves. The cavity accelerates the chemical reaction by increasing the total transmission coefficient compared to $\kappa^{(0)}$, i.e. $R > 1$. This is illustrated by the blue trace in Fig 4.3b.

Next, we consider $N = 64$, where one molecule corresponds to the AM while $N - 1$ are NAMs. Rather than fixing the macroscopic Rabi splitting by multiplying the coupling strength with the $1/\sqrt{N}$ factor, we keep it constant to $g = 0.4$ V/nm. Hence, the AM is coupled to the cavity with the same coupling strength in both the $N = 1$ and the $N = 64$ cases. This way, we ensure a genuine collective modification of the dynamics of the AM through the presence of non-activated molecules by avoiding an artificial re-scaling of the cavity to single-molecule coupling. And these molecules are indirectly coupled to the AM through the cavity mode. For $N = 64$, $\kappa^{(c)}$ is further enhanced, as seen by comparing the orange and blue curves in Fig 4.3a. The cavity plus NAMs further accelerate the chemical reaction by increasing the total transmission coefficient compared to $\kappa^{(0)}$ and to $\kappa^{(c)}(N = 1)$ i.e. $R > 1$.

The plateau value as a function of the number of molecules is shown in Fig 4.3a. One observes that the effect stagnates at $N \approx 36$ for the choice of model parameters. As such, the reported modification does not explain the macroscopically large N limit, which remains a standing unresolved issue in the field, but which is not the focus of this contribution. However, our simulations shed important light on the distinct roles played by the AM and NAMs in the few molecules, vibrational strong coupling regime. Thus, in the following

our goal is to explain the mechanisms by which the added NAMs modified the reaction rate of the AM, even though the AM and NAMs not directly coupled and only see each other indirectly through the cavity degree of freedom.

Let us first compare the simulations with randomly oriented initial conditions to simulations performed with aligned molecules, which is defined in chapter 3. When all molecules have their x-aligned with the cavity polarization the collective effect disappears, as illustrated by the orange trace in Fig 4.3b. On the other hand, when the cavity polarization is aligned with HONO's y-axis, the enhancement of the reaction rate with increasing N is even more pronounced as compared with the randomly oriented case. When $N = 1$, R is similar for all three cases. However, when $N > 1$, a modification of reaction rate is only observed for randomly oriented and y-aligned cases. This observation indicates them importance of the orientation of the molecules with respect to the cavity polarization. Also, the AM and the $N - 1$ NAM (spectators) play different roles in connection with their orientation inside the cavity.

As molecules are x-axis oriented with respect to the cavity polarization, the largest variation of the permanent dipole occurs at the transition state region, which is shown in blue trace in Fig. 4.2b. Hence, the AM efficiently couples with the cavity in this orientation. On the other hand, the AM also couples efficiently with the cavity when its y-axis is oriented with the cavity polarization. Here, the most efficient coupling will occur when the AM visits the *cis* or *trans* regions of the configurational space (see orange trace in Fig. 4.2), which occurs just a few femtoseconds before or after having passed the TS. This situation is radically different for the NAMs. The energy content of the NAMs along the reaction coordinate is thermal and much lower than the AM, which leads to that the NAMs are not able to visit the TS region. Thus, they are confined to oscillate close to the potential energy minimum, where, in the case of HONO, $\partial\mu_x/\partial\tau = 0$. Thus, when the cavity is tuned to the frequency of the HONO torsion, only y-aligned NAMs can participate, whereas x-aligned NAMs are literally invisible to the cavity. Summarizing, both the AM and the $N - 1$ NAM must be efficiently coupled to the cavity for collective effects to take place, which may not necessarily occur for the same orientation, or even cavity frequency, as we illustrate in the next section.

4.3 Collective effect with different cavity frequency

In the previous section, we have already shown the modification of reaction rate arising from molecular orientation. The mechanism by which the NAMs modulate the reaction rate is not obvious and requires further exploration. Figure 4.4 shows R as a function of ω_{cav} from 400 cm-1 to 800 cm-1. Interestingly, the rate modification peaks at a different

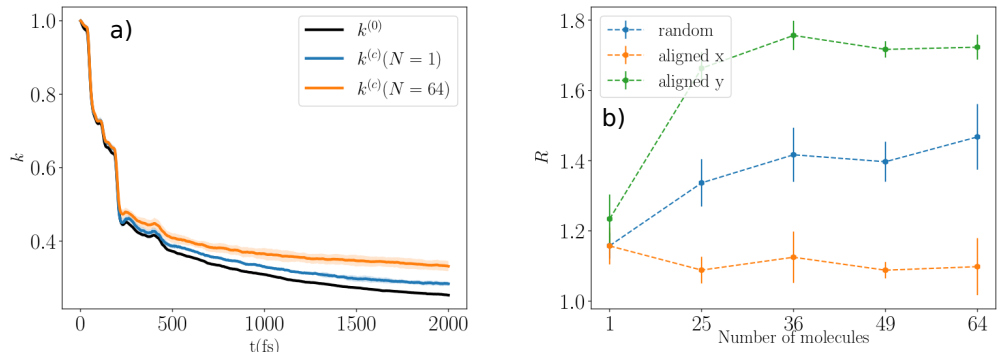

Figure 4.3. a) Transmission coefficient $\kappa^{(c)}(t)$ with fixed $g = 0.4$ (V/nm) with different N, $\omega_{cav} = 640$ cm-1 b) R for increasing number of molecules with fixed $g = 0.4$ V/nm (see text for details). Random case means that all molecules always randomly orientate when evolution. Aligned $x(y)$ molecules mean that the cavity polarization is aligned with HONO's $x(y)$-axis and orientations of all HONO are fixed at all time.

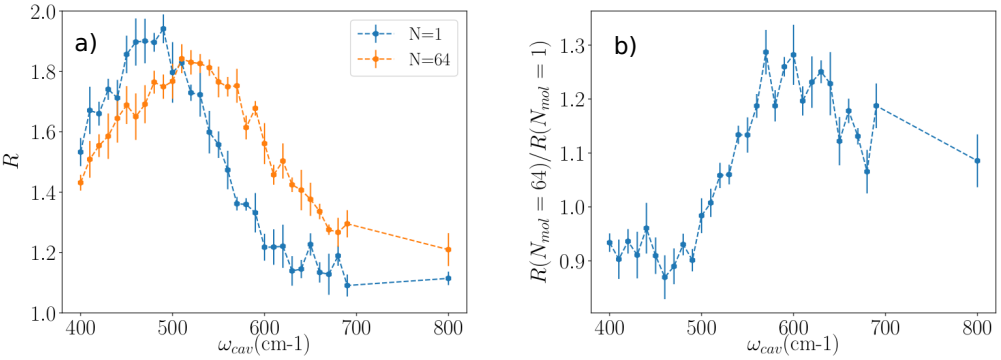

Figure 4.4. a) R for various cavity frequency from 400 to 800 cm-1. $g = 0.4$ V/nm and $T = 300$ K for all calculations. b) A ratio of $R(N = 64)$ and $R(N = 1)$

frequency for the cases $N = 1$, 490 cm^{-1}, and $N = 64$, 510 cm^{-1}, with the single molecule case (thus necessarily the AM) being red-shifted by roughly 20 cm^{-1}. Considering the ratio of $R(N = 64)/R(N = 1)$, one sees that the maximum collective effect peaks at $\omega_{cav} \approx 600$ cm^{-1}. The difference observed in figure 4.4 implies that the reaction rate can be altered by the resonance condition between the cavity and the AM, which is influenced by the NAMs. To shed light on this matter, we present spectrum of molecules and cavities in the next section.

4.4 Spectrum of HONO and cavity

Fig. 4.5a compares the spectrum of the velocity-velocity correlation function of the reaction coordinate, $I_{vv}(\omega)$, for AM and NAM i.e. for HONO trajectories sampled from a thermal

distribution at the TS dividing surface, and for HONO molecules in thermal equilibrium around the *cis* configuration, respectively. Fig. 4.5a shows that the vibrational frequency of the AM along the reaction coordinate is red-shifted compared to the NAM, which is caused by the anharmonicity of the potential well along this coordinate and the higher energy content of the AM. Quantum mechanically, the anharmonic vibrational energy levels with the excitation localized along the reaction coordinate become closer, in particular $\tilde{\nu}_{01} = 632$, $\tilde{\nu}_{12} = 581$, $\tilde{\nu}_{23} = 555$, $\tilde{\nu}_{34} = 515$, and $\tilde{\nu}_{45} = 467$ cm^{-1} [120, 122], which classically results in a longer oscillation period at higher energy. The velocity-velocity spectrum of the NAMs can be compared with the spectrum of the dipole-dipole correlation function [128, 129], $I_{\mu\mu}(\omega)$, confirming that the peak at about 600 cm^{-1} in $I_{vv}(\omega)$ corresponds to the vibrational frequency of the NAM along the reaction coordinate. To validate the classical spectra we compare to an anharmonic quantum mechanical spectrum calculated with the MCTDH approach using the Heidelberg package [130, 131] and showing qualitatively good agreement(shown in fig 4.6).

The velocity-velocity spectrum of the NAMs explains the observed peak in fig 4.4a as $N = 1$. As $N = 1$, only the AM is inside the cavity, one can reach the largest rate modification by tuning the cavity to be resonant with the vibrational frequency of the AM. However, as N increases, the largest rate modification occurring toward higher cavity frequencies cannot be directly explained by this blue-shifted vibrational frequency of the NAMs compared to the AM. As ω_{cav} shifts to the blue, the AM should go off-resonance while the NAMs are not undergoing the chemical reaction, so the fact that they are resonant with the blue-shifted cavity should not change the transmission coefficient of the AM unless this has some direct effect on it. Figures 4.5b and 4.5c show the spectrum of the velocity-velocity correlation function, $I_{vv}(\omega)$, for the cavity mode for $\omega_{cav} = 490$ and 640 cm^{-1}, respectively, and for 0, 1 and 64 molecules in the cavity. At $\omega_{cav} = 490$ cm^{-1}, $I_{vv}(\omega)$ presents a single peak at 490 cm^{-1} in all cases, without the formation of polaritonic peaks due to the relatively small single-molecule coupling, and with just a small red-shift for $N = 64$. On the other hand, and in stark contrast, $I_{vv}(\omega)$ presents two polaritonic peaks for the $N = 64$ case and $\omega_{cav} = 640$ cm^{-1}. Indeed, we want to emphasize that our choice of single-molecule coupling strength has been made such no polaritonic branches exist for one single molecule but they develop while increasing the number of molecules at fixed coupling from $N = 1$ to $N = 64$, and still strong enough that the isomerization rate is affected for $N = 1$. Hence, at $\omega_{cav} = 640$ cm^{-1} the cavity is resonant with the NAMs and the collective coupling is strong enough to split the cavity frequency in an upper (UP) and lower polaritonic (LP) resonance. The LP is resonant with the frequency of the AM, which leads to an efficient coupling and to the corresponding modification of the rate. Thus, the following conclusions can be drawn: (1) For an effective modification of the rate in the single-molecule, strong coupling regime,

the AM must be efficiently coupled and resonant with the cavity. This can be through the reaction coordinate directly or through other modes anharmonically coupled to the reaction coordinate, as we have demonstrated in chapter 3. (2) In the collective $N >> 1$ strong-coupling regime, the AM must be resonant with the cavity mode dressed by the NAMs, meaning for example resonances of the AM with polaritonic modes formed by the $N-1$ spectators and the cavity.

4.5 Energy distribution between molecules and cavity

Until now, we have performed the spectra to illustrate how the reaction rate and ω_{cav} is affected by including the NAMs inside the cavity. The underlying physical mechanism by which the cavity plus NAMs change the reaction rate of AM is still not fully understood. For this, we focus on the total energy variation of the AM after it has passed the transition state, $\Delta E = E(t) - E(0)$, as a function of time as plotted in Fig 4.7. The total energy of the cavity plus all molecules is divided into three subsystems, the AM, the NAMs and the cavity, and we consider the case for random molecular orientation. The energy barrier is about 4000 cm^{-1} or 20 $k_B T$ at $T = 300$ K.

The fastest energy loss from the AM occurs for $N = 1$ and $\omega_{cav} = 490$ cm-1, closely followed by $N = 64$ and $\omega_{cav} = 490$ cm-1 (blue and orange traces). The corresponding relative change in rate is $R = 1.9$ and $R = 1.8$, respectively (cf. Fig. 4.4b). The energy loss from the AM is slower at $\omega_{cav} = 640$ cm-1 than at $\omega_{cav} = 490$ cm-1. At $\omega_{cav} = 640$ cm-1, the $N = 64$ case loses AM energy faster than $N = 1$, since in the latter situation the resonance of the AM is largely detuned from the cavity, whereas for $N = 64$ the AM is resonant with the lower polaritonic state. The corresponding relative changes in the reaction rate are $R = 1.4$ and $R = 1.2$ for the $N = 64$ and $N = 1$ cases, respectively. Thus, the relative change in rate and the energy loss from the AM at short times are directly correlated. The better the AM is resonant with a mode of the cavity plus NAMs, the fastest the energy exchange of the AM with the rest of the system at short times after crossing the TS, and the largest relative change in the chemical reaction rate. Only the energy transfer at short times is relevant since $\kappa^{(c)}(t)$ reaches its plateau value when the AM becomes, on average, trapped in the reactant or product wells due to energy loss.

4.6 Cavity with friction

Based on the result of Fig 4.3 and 4.7, the key factor of enhancing the reaction rate is relevant to the energy transfer efficiency between the cavity and AM. We expect that cavity loss might also help the cavity take energy from the AM. To confirm this, a single HONO is considered

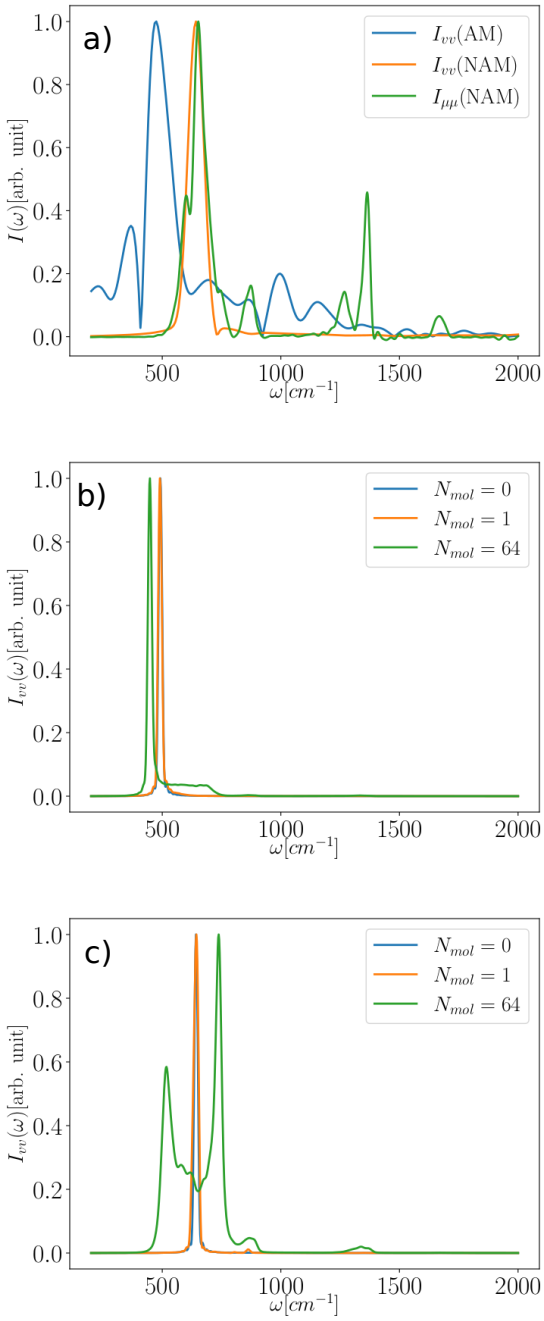

Figure 4.5. a) IR spectrum of non-activated HONO(NAM) and activated HONO(AM). The spectra are shown in absolute value. b) Velocity-velocity correlation spectrum of the cavity mode for $\omega_{cav} = 490$ cm^{-1}. c) Same as b) for $\omega_{cav} = 640$ cm^{-1}. $g = 0.4$ V/nm and $N_{mol} = 0, 1, 64$.

inside a cavity with friction. That is to say, the lifetime of the cavity is no longer infinite. Describing the cavity loss through the lifetime of the cavity is nothing new. The lifetime of the cavity has been used to study the relaxation of polariton states [132].

In our simulation, a cavity with friction is equivalent to a damping oscillator. A wave

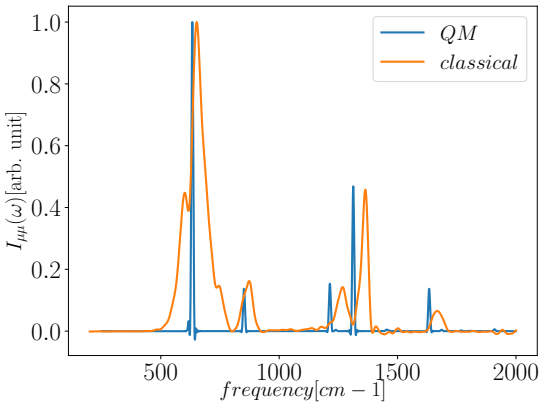

Figure 4.6. A comparison of quantum and classical IR spectra of spectator molecules. The classical one is obtained by the Fourier transform of dipole-dipole autocorrelation function.

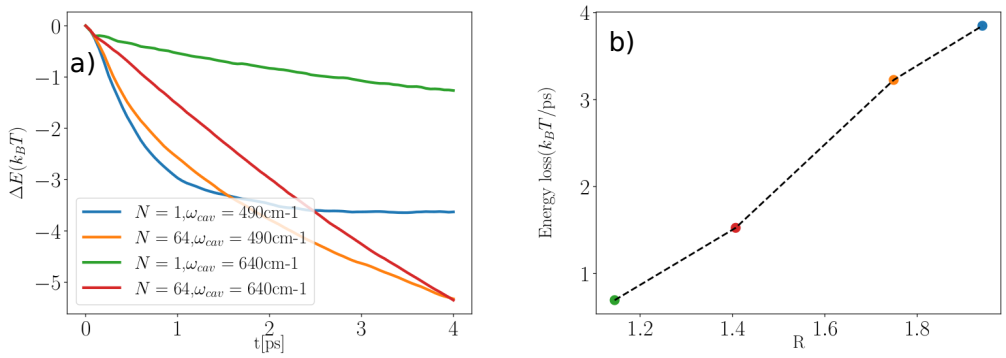

Figure 4.7. a) The energy difference, $\Delta E = E(t) - E(0)$, of AM as a function of time is plotted with $g = 0.4$ V/nm and $T = 300$ K for all calculations. b) The average energy loss, $E(t) - E(0)/t$, of AM within the first 0.5 ps is plotted as a function of R. The color of each point corresponds to the conditions shown in a).

packet of a damping oscillator can be described by $Ae^{-t/\Gamma}$, where A and T are constant. And the friction is defined as $1/\Gamma$. This implies that an open system is generated when put molecules inside the cavity with friction. An irreversible IVR pathway occurs and one can expect the cavity can efficiently take energy from the AM. Considering the random orientated case with fixed $\omega_{cav} = 640$ cm-1 and $g = 0.4$ V/nm, one sees in fig 4.8 that R is largely enhanced when the friction on the cavity increases, which provides a similar behavior with the results in fig 4.3. This confirms that the reaction rate inside the cavity can be enhanced by the cavity loss or an irreversible energy pathway. Hence, the energy transfer efficiency in the short term plays a critical role when altering reactivity.

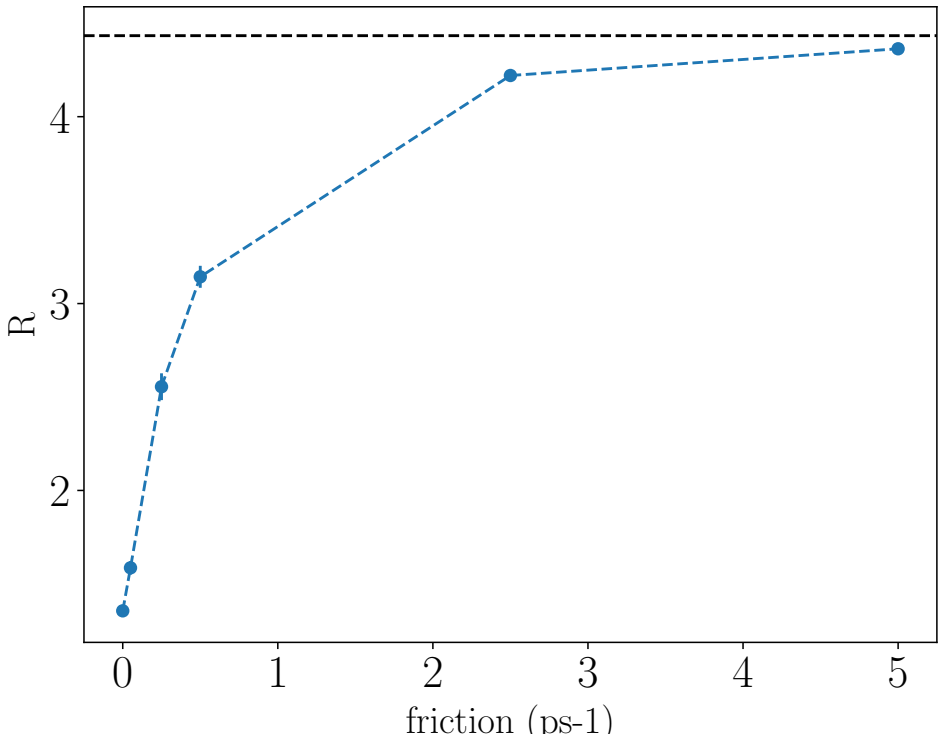

Figure 4.8. R for various friction on cavity for $N_mol = 1$ with fixed $g = 0.4$ V/nm, $\omega_{cav} = 640$ cm-1. Black dashed line represents the maximum of R.

4.7 Conclusion

In this chapter, we increase the number of molecules inside the cavity with fixed coupling strength. This treatment leads to that the Rabi splitting increases as the number of the molecules increases. In the y-aligned and free-orientated case, an enhancement of the reaction rate is observed. However, in the x-aligned case, the reaction rate changes little when adding molecules inside the cavity. The difference between each case can be explained by the modulation of the dipole. The largest modulation in the transmission coefficient occurs when the reaction coordinate in the activated molecule becomes resonant with the cavity or a polaritonic resonance of the cavity with the non-activated molecules. We stress that the enhancement of the reaction rate is sensitive to the energy transfer efficiency from the activated molecule to the cavity. This is also observed when adding friction to the cavity.

Chapter 5

Meyer-Miller mapping for fermionic dynamics

In this chapter, in order to explore the application of MM mapping of fermions, we compare the MM mapping with exact quantum results and with different mappings explicitly designed for fermions including the SM and the LMM in both non-interacting and interacting systems. Except in the discussion of Fig 5.3a, where an explicit comparison between discrete and random sampling is made, the initial conditions for all classical mapping calculations and for all benchmarked mappings are generated by random sampling of the angle variables. All quantum calculations are obtained using the multi-configuration time-dependent Hartree (MCTDH) approach [130,131,133] in the second-quantization representation (SQR) formulation [103,104,134], which is equally applicable to fermions and bosons. In Section 5.1, we address several many-body systems without interactions, where the performance of different mapping are discussed. We then demonstrate different sampling methods in 3-site system to illustrate the perfomance of the MM mapping of fermions is attributed to the description of the density matrix. In Section 5.2, we compare Hubbard and impurity Hamiltonians, with interactions, and consider as well a model for excitonic energy transfer between chromophores. In this model with interactions we show that the classical MM mapping is able to capture interference effects caused by the presence of different energy transfer pathways leading to the same final state, both when the interferences are constructive and destructive.

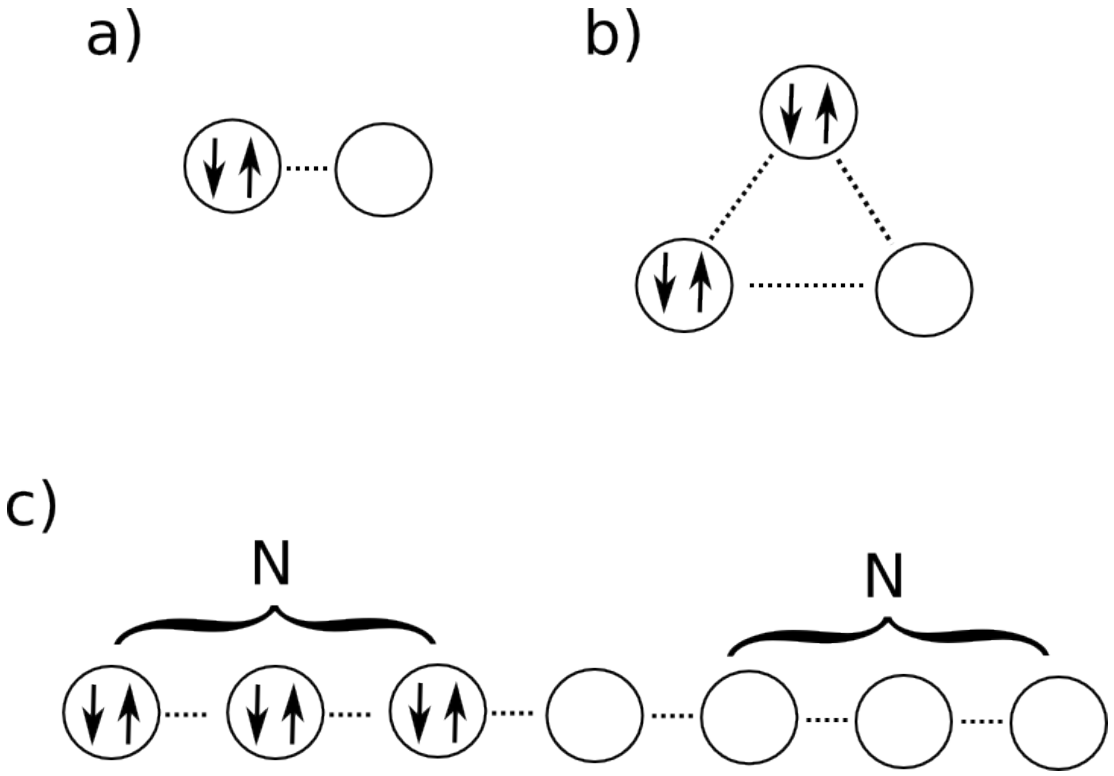

Figure 5.1. Structure of a) 2-site and b) 3-site tight-binding systems. The arrows indicate the occupation of the orbitals at $t = 0$ and the dashed lines represent the one-body transfer integrals h_{ij}.

5.1 Non-interacting system

We start from comparing the MM and SM mapping with the exact electron dynamics in 2- and 3-site tight-binding Hamiltonians

$$\hat{H}_{\text{tb}} = \sum_{\langle i,j \rangle}^{F} \sum_{\sigma=\alpha,\beta} T(\hat{c}^{\dagger}_{j,\sigma}\hat{c}_{i,\sigma} + \text{h.c}), \tag{5.1}$$

where $\langle i, j \rangle$ indicates that the sum runs over nearest neighbors only. A diagram indicating the interactions between the sites is shown in fig 5.1, where orbital interaction terms are marked with a dotted line and are all set to $T = -0.05$ Hartree.

For the MM mapping, the relations(eq 2.50) is applied to Hamiltonian(eq 5.1) to reach the classical Hamiltonian function. For the spin mapping, Jordan-Wigner transformation is applied to the fermionic quantum-mechanical operators(eq 2.61) and we arrive at the classical Hamiltonian at the basis of spin-$1/2$(eq 2.64). Moreover, for the Li-Miller mapping, the concept of quaternion operators is used to capture the properties of second-quantized fermionic operators, which arrives at the Hamiltonian in eq 2.65.

5.1.1 2-site system

We examine now the population dynamics of the 2-site tight-binding model starting with site 1 fully populated, fig 5.1a. Note that when applying the JWT to the tight-binding binding Hamiltonian (5.1) with linear topology one arrives at a pure spin-$1/2$ Hamiltonian where all $\hat{S}_k$ operators have canceled. Therefore, SM and MW (meaning JWT+SM) are equivalent. Fig 5.2 shows that the MM representation yields the exact dynamics. This is not surprising since the MM mapping describes the exact dynamics in the non-interacting case, which has been shown in section 2.3 of chapter 2.

On the other hand, one may think a classical SM representation should also deliver an accurate approximation to the quantum dynamics or even be superior to the MM mapping since we are dealing with a quantum spin Hamiltonian. Fig 5.2 shows how the SM fails to reproduce the exact population dynamics. In fact, the equations of motion of the SM model are not fully linear, which leads to continuous dissipation of the classical trajectories in phase space, and hence to their failure to reproduce the correct amplitude of the population oscillations. This observation is not new, and the reason why Miller and collaborators have developed the LMM Cartesian (oscillator-based) version of the original MW mapping in recent years [69–72].

5.1.2 3-site system

Uniform sampling

Matters turn more interesting when considering a 3-site tight-binding Hamiltonian with cyclic topology, where the initial occupation of the sites is shown in fig 5.1b. Now, the sign-change operator $\hat{S}_2$ of the JWT survives in the term proportional to h_{13}, meaning that the SM and SM+JWT mappings result in different classical Hamiltonians. As expected from our theoretical considerations, the MM mapping reproduces the exact population dynamics, even if now the JWT yields a sign-change operator(cf. fig 5.3a). The same is found to be true for the LMM, which explicitly considers the anti-commutation relations of the fermionic operators. The SM+JWT mapping, instead, again fails to represent the correct site-population dynamics, now even more dramatically than before.

Discrete sampling

For comparison, we also examine the dynamics of the same 3-site Hamiltonian(6 DOFs) but now the initial one-body density matrix is mapped to $N = 8$ trajectories. The population dynamics in fig 5.3b shows that MM and LMM reproduce the quantum results while the SM and SM+JWT mapping fails to describe the time evolution of the populations and even

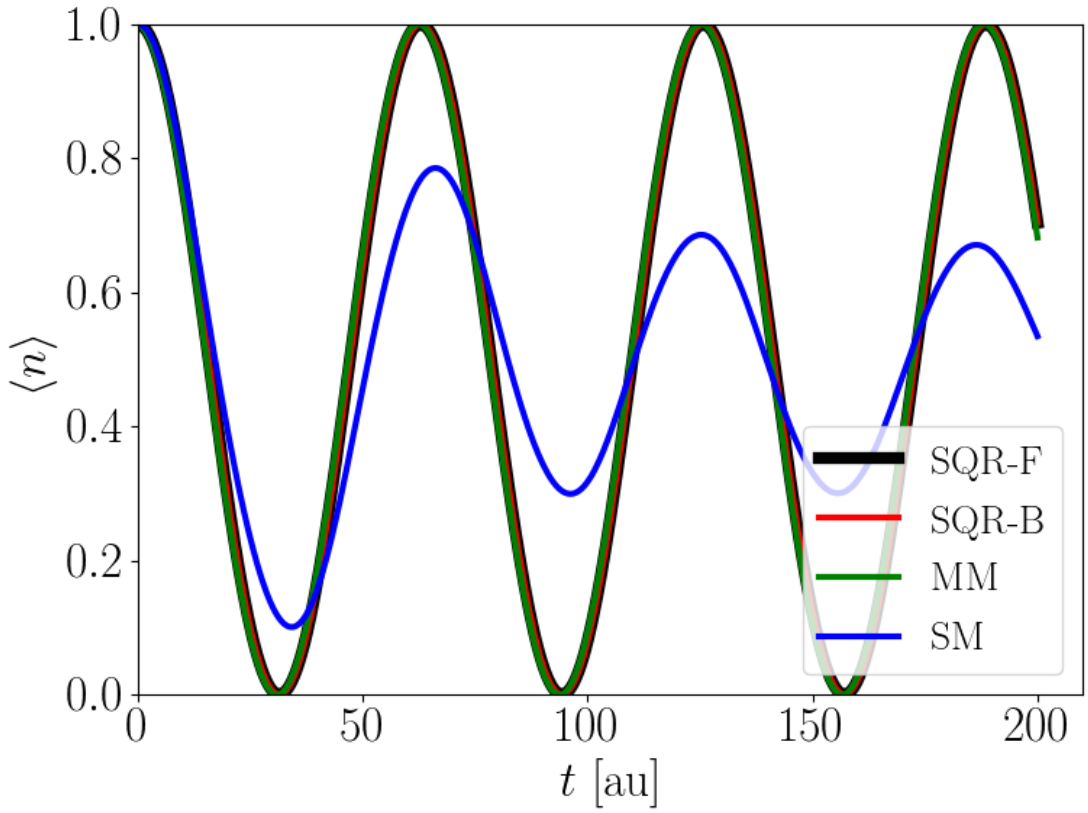

Figure 5.2. Time-dependent population of site 1, $n_{1\alpha}$, in the 2-sites tight-binding system for exact fermionic and bosonic dynamics, and for the MM and SM mapping approaches. The transfer integral is set to $T = -0.05$ Hartree.

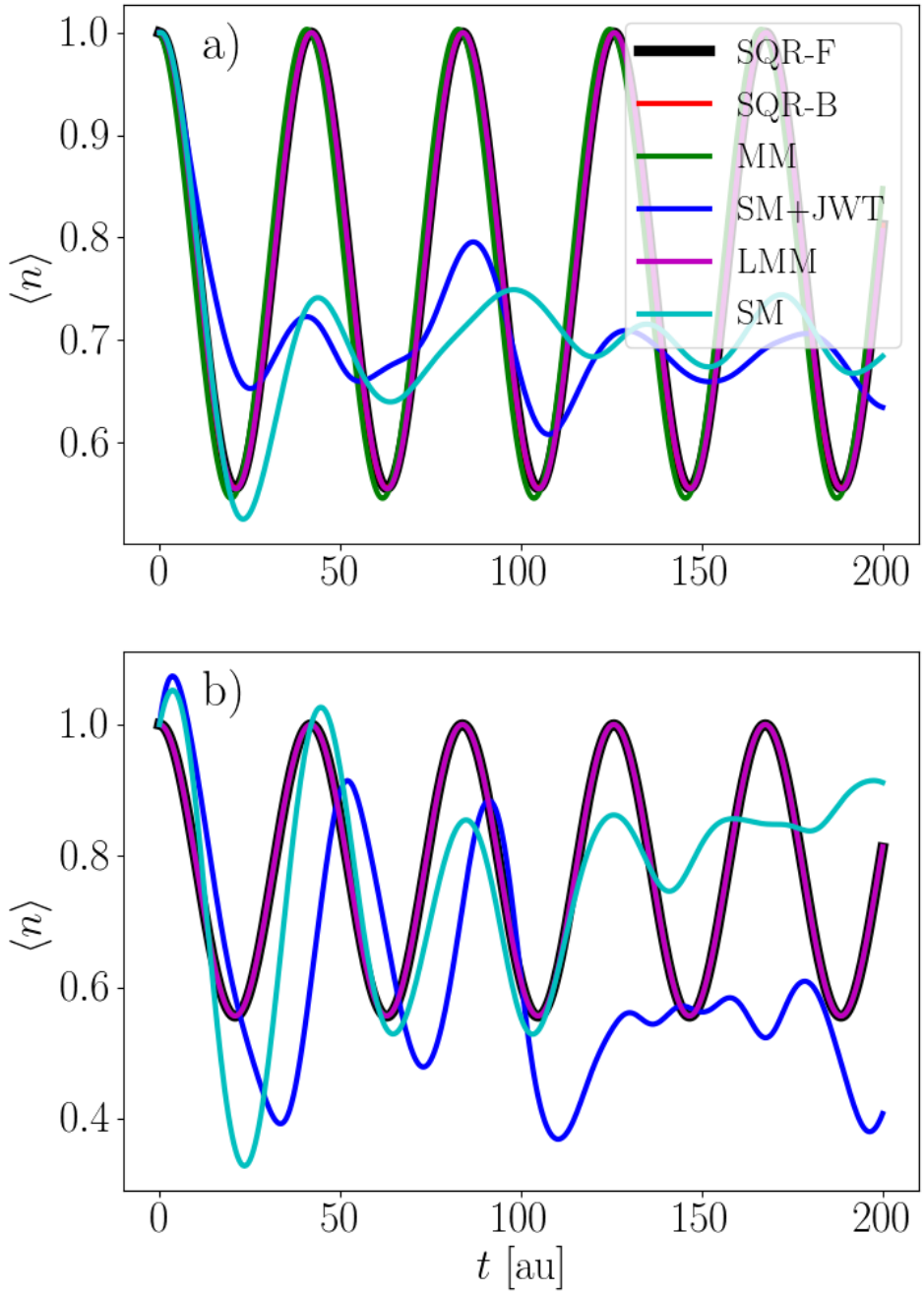

Figure 5.3. Time-dependent population of site 1, $n_{1\alpha}$, in the 3-sites cyclic tight-binding system for exact fermionic and bosonic dynamics, and for the MM, SM, SM+JWT and LMM mapping approaches. (a) initial conditions generated by homogeneous random sampling. (b) discrete sampling initial conditions with $N = 8$ trajectories. In both cases all approaches yield the exact result, except the SM and SM+JWT ones.

maintain the oscillatory behavior in the long-term. The two SM-based mappings yield different results when compared among themselves and the SM mapping follows more closely the oscillations of the quantum mechanical population dynamics. From this observation, we obtain a first hint at the fact that, including antisymmetry with a JWT before performing the classical mapping, which is implicit in the MW and LMM treatments [31, 72], may not actually be relevant to the mapping of fermions and may indeed be counterproductive, resulting in a classical Hamiltonian with higher-order interactions than simpler mappings and a more chaotic classical dynamics that deviates earlier from the correct quantum result. Comparing the random and discrete sampling results of SM-based mappings in fig 5.3a and 5.3b, we also notice that the discrete mapping based on $N = 8$ trajectories leads to a better description of the oscillations of the populations than the random-sampling results, since fewer trajectories hinder dissipation (through averaging) in the classical phase-space.

Populations of individual trajectories

Here, we want to examine the population dynamics in the 3-site system from the perspective of the *individual* trajectories in the random-sampling case. The population of site 1 for each of 1000 trajectories can clearly grow above $n_1 = 1$ both for the LMM and MM mappings as seen in fig 5.4. Nonetheless these trajectories reproduce in average the exact population dynamics. The common wisdom is that fermionic mappings need to be limited by the construction of the maximum value of the classical action variables at the trajectory level because there can be no more than one fermion per spin-orbital. We see, however, that imposing this restriction at the level of individual trajectories is not required for many-body systems without interactions, as only the average value from all trajectories can be given a physical meaning. Even the fermion-tailored LMM can reach populations larger than 1 (cf. fig 5.4b) and still yield the exact averaged population dynamics.

5.2 Interacting system

In the previous section, we show that the MM mapping is in good agreement with the exact electron dynamics in non-interaction systems as our expectation. We note that the MM mapping reproduces the exact quantum dynamical results whenever the initial phase space distribution matches the initial one-body density of the system. Next, we benchmark the performance of the MM mapping in interacting systems against other mappings, and against exact quantum dynamical results. We consider first the Hubbard Hamiltonian, which consists of a tight-binding Hamiltonian plus an on-site repulsion $U\hat{c}^\dagger_{i,\alpha}\hat{c}_{i,\beta}\hat{c}^\dagger_{i,\alpha}\hat{c}_{i,\beta}$. The classical mapping for the Hubbard interaction term takes the form $Un_{i\alpha}n_{i\beta}$, where $n_{i\sigma}$ are functions of the classical phase-space variables. We have already seen the limitations of SM

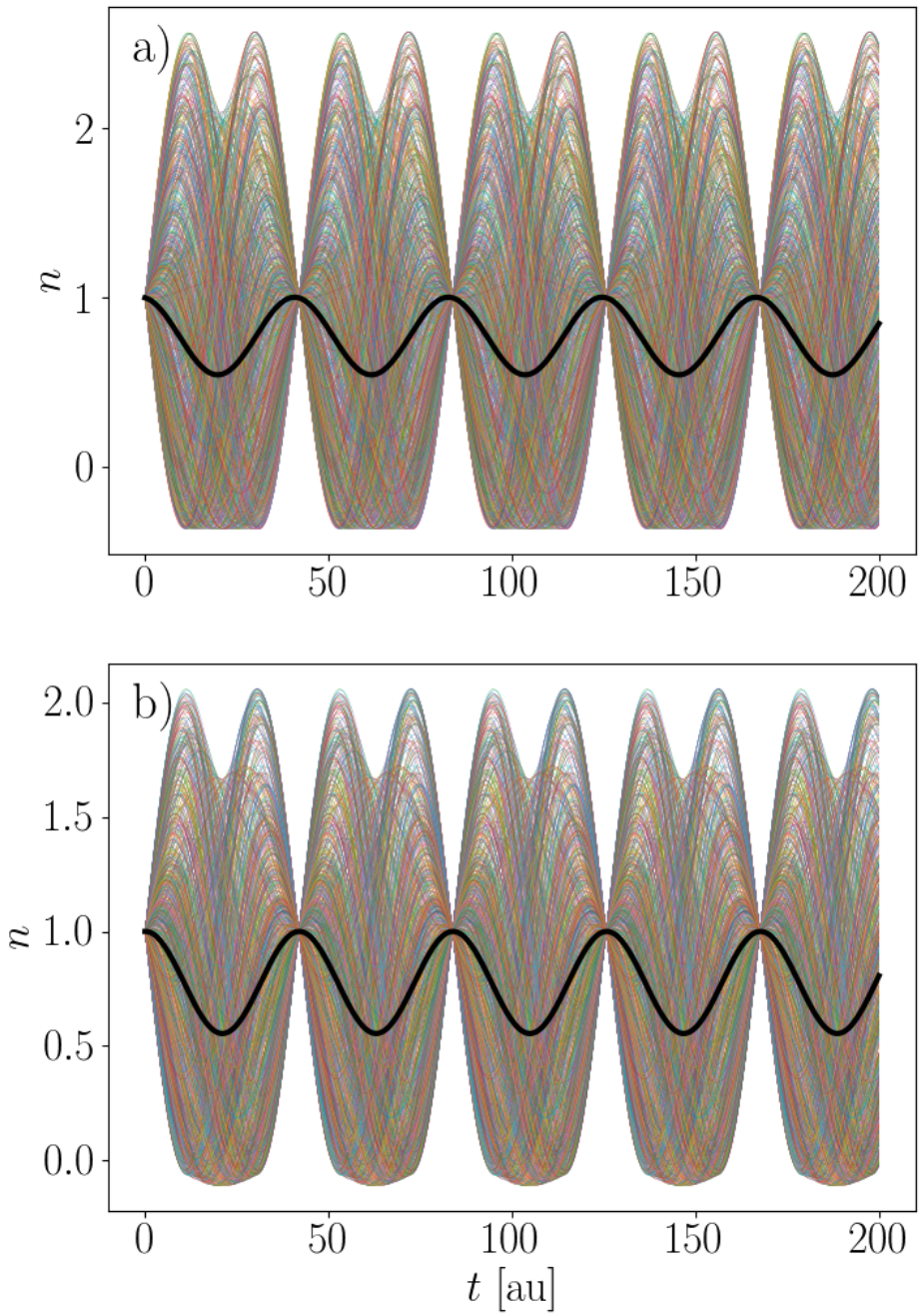

Figure 5.4. Time-dependent population of site 1, $n_{1\alpha}$, for each single trajectory in the 3-sites cyclic tight-binding system for a) the MM model and b) the LMM model. Both sets of trajectories yield the same exact expectation value of the population for this non-interacting Hamiltonian. The expectation value $\langle n_{1\alpha} \rangle$ over the trajectories is shown as a thick black line.

and SM+JWT in the non-interacting systems. Here, we mainly focus on the comparison of MM, LMM and the exact quantum results. We start from a 3-site cyclic chain with on-site repulsion terms followed by the simulation of different impurity Hamiltonians. Again, the topology of the systems is shown in fig 5.1. Afterwards, we compare the mappings in their ability to describe excitonic energy transfer between model chromophores.

5.2.1 3-site cyclic system

Figure 5.5a shows the time evolution of the $n_{1\alpha}$ population in the 3-site cyclic system for the ratio $|U/T| = 1$ between the transfer integral and the on-site repulsion. The initial state is the same as for the bosonic and fermionic exact dynamics (Fig 5.1b) and their population dynamics remain practically identical for more than one period of oscillation. Naturally, fermionic and bosonic population dynamics diverge as time progresses and follow a completely different time evolution already after about two periods of oscillation. Both the MM and LMM capture the period of the first oscillation, and the MM follows more closely the trace of both exact fermions and bosons. Incidentally, the MM mapping follows more closely the fermionic than the bosonic population, whereas the LMM is closer to the bosonic than to the fermionic trace after a few oscillations. These results are constrained to this particular system and parameters. The applicability of the observation requires further investigations. Two important aspects that we are going to explore with further numerical examples: i) The MM, which one could consider as the genuine mapping for bosons, does not necessarily reproduce the bosonic dynamics better than the fermionic one. ii) The LMM, which is designed to reproduce certain aspects of fermionic systems, can indeed in some instances yield results closer to the bosonic time evolution and does not necessarily reproduce the fermionic dynamics more accurately than the simpler MM prescription.

For non-interacting systems, we have seen how a set of trajectories yields the exact evolution of the populations and one-body correlations. The choice of the set of trajectories is not unique and the only condition is that the set of trajectories exactly maps the initial one-body density of the quantum system. For interacting systems, this is not the case anymore. Different initial ensembles encode different two-body densities, and these evolve differently under interactions. The population dynamics in fig 5.5b corresponds to the same parameters as in fig 5.5a but now the initial density one-body density is mapped with only $N = 8$ trajectories, instead of a uniform sampling. Both MM and LMM are found to perform worse in comparison with the quantum mechanical results than the uniform sampling results. However, compared to the uniform sampling, the ensemble dynamics of the discrete sampling retains oscillations for a longer time because a smaller number of phase-space points are being averaged. This indicates that a possible strategy to improve on these results might in-

volve mapping both the one- and two-body densities of the quantum system to the smallest possible number of trajectories, but we are not pursuing this strategy here and instead use the uniform sampling strategy in the following.

In the strong repulsion limit, $U >> T$ the fermionic and bosonic exact quantum dynamics in Fig 5.5c quickly diverge. It is surprising that both MM and LMM mappings still reproduce the fermionic dynamics rather well at early times, and we have not been able to develop an intuitive explanation for this fact. An extreme example consists of a system with all spin-orbitals occupied. Under fermionic statistics, such a system is blocked: all its orbital populations remain equal to 1 at all times. Its bosonic counterpart, though, does not experience this Fermi blockade and its populations can present fluctuations. These fluctuations vanish for a non-interacting system, or in the case that the transfer integrals and on-site repulsions are fully symmetric. Figure 5.5d shows the populations of the fully-occupied Hubbard system with $|U/T| = 1$ (with $U = 0$ for site 1 only). Whereas the quantum fermionic populations remain constant, the bosonic populations fluctuate and so do the populations calculated with both mappings to within a similar range. Intriguing are the fluctuations of the LMM, which is devised to reproduce the behaviour of fermions. This indicates again that the LMM is not superior to the simpler MM prescription at reproducing the dynamics of a fermionic system, and they perform similarly in this connection.

5.2.2 Impurity Hamiltonian

Impurity models describe electron transport processes and have been approached by classical mappings in recent works [72]. Here we consider two tight-binding chains (left and right) of N conduction orbitals coupled to a central single-impurity orbital with a local interaction term U (fig 5.1c). In total each model consists of $2N + 1$ sites and we consider chains with $N = 3, 10$.

Simulations in the $N = 3$ system (7 sites) can still be easily performed quantum mechanically and comparisons with the classical mappings are shown in Fig 5.6. Simulations with $N = 10$ are only approached using the classical mappings. We consider weak and stronger interaction regimes, $|U/T| = 0.1$ and $|U/T| = 1$, respectively, and set all electrons to be on the left conduction chain of the impurity model at $t = 0$. These are quite extreme initial conditions in terms of chemical potential if one compares with simulations aimed at reproducing steady-state conditions of the impurity model [72]. We emphasize that our goal is to benchmark and characterize the performance of the mappings against full quantum results, rather than reproduce specific experimental conditions.

The population (number of electrons) of the left conduction chain and of the central impurity site for the $N = 3$ are shown for the two coupling strengths in Fig 5.6. The quantum

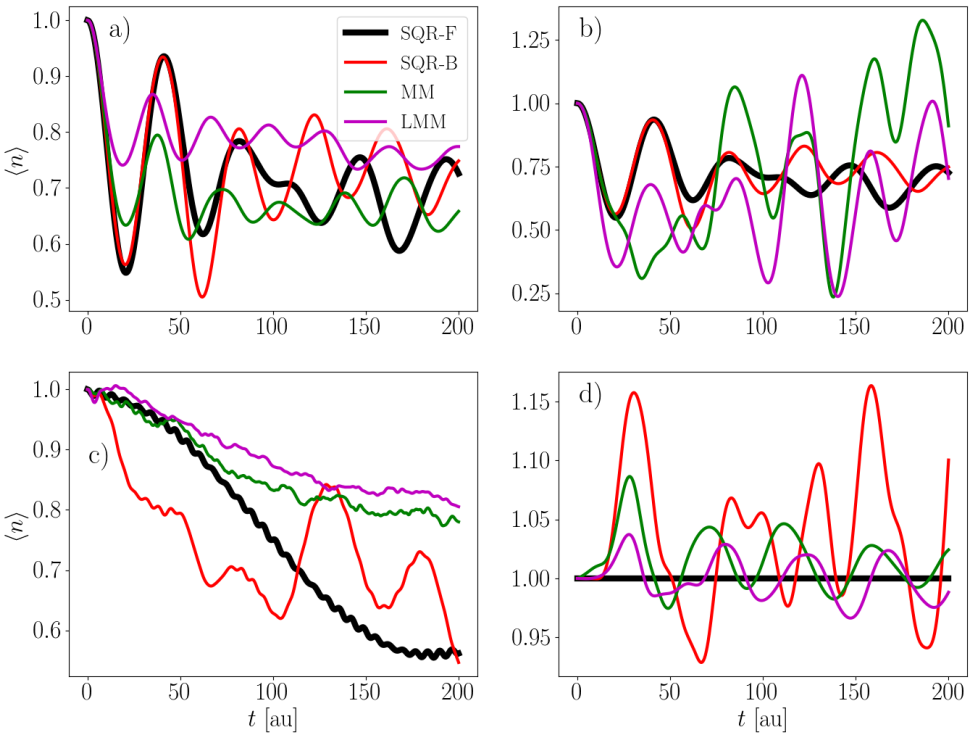

Figure 5.5. Population dynamics of $n_{1\alpha}$ for the 3-site cyclic Hubbard model with $T = -0.05$ and $U = 0.05$, except c) where $U = 0.5$. In d), the energy of each is site is slightly tilted. $E_1 = -0.02$, $E_2 = 0.0$, and $E_3 = 0.02$. a) uniform sampling; b) discrete sampling; c) strong interaction; d) all spin-orbitals initially populated.

fermionic and bosonic dynamics are similar for both coupling strengths when starting from a fermionic initial state. The exact fermionic calculations require 64 single particle functions (SPF) to span the corresponding sub-Fock spaces of the left and right conduction chains and 4 SPFs for the middle site [104]. The truncated fermionic calculation uses a basis of 40 SPFs for the left and right sites and 4 SPFs for the middles site.

In the case of weak interaction, both the quantum bosonic and fermionic dynamics (red and black traces) remain very similar and both the MM and LMM mappings reproduce the population dynamics extremely well, as seen in Fig 5.6a and Fig 5.6c. The worst result corresponds to the non-exact quantum mechanical calculation with 40 SPFs (blue trace). The reason for this is easily understood. In calculations based on a second-quantization representation [103, 104], the correlation between the computational degrees of freedom (i.e. the orbital occupations) depends on the hopping integrals T, not on the on-site electron repulsion U. Indeed, the case of stronger electron-electron repulsion is comparatively better described by the approximate quantum calculation as compared to the exact result.

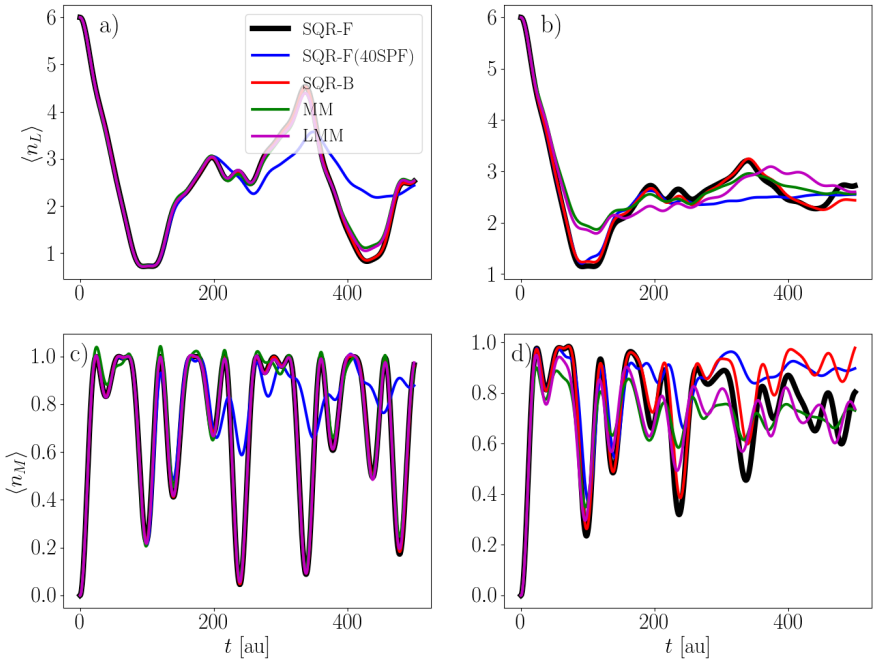

Figure 5.6. In a linear chain system($N = 3$), a) & b) n_L and c) & d) n_M are described. In the system, a) & c) $(T, U) = (-0.05, 0.005)$ while b) & d) $(T, U) = (-0.05, 0.05)$. For all classical mappings, trajectories are generated by the uniform sampling.

Even in the case of stronger coupling, $|U/T| = 1$, both classical mappings are able to reproduce the population of the conduction chains and impurity site remarkably well (fig5.6b and 5.6d). Interestingly, the population of the impurity never surpasses $\langle n_M \rangle = 1$ for either classical mapping even when the electronic flux towards the right conduction chain is maximal during the first 100 au of time. This again strengthens the observation that enforcing a limitation of the maximal population of the fermionic degrees of freedom via the classical mapping (e.g. using classical spin DOFs) is unnecessary, and that the MM performs similarly as LMM while using half the number of classical DOFs.

Finally, we consider an impurity model with $N = 10$ sites in each conduction chain and show its population dynamics, in Fig 5.7. where we compare the MM and the LMM for both interaction strengths. As the number of sites increases, the averaged populations of the left, central and right sites becomes more similar between both mappings. The small fluctuations of the central impurity in fig 5.7 are perfectly captured and the population of the impurity does not grow above 1.

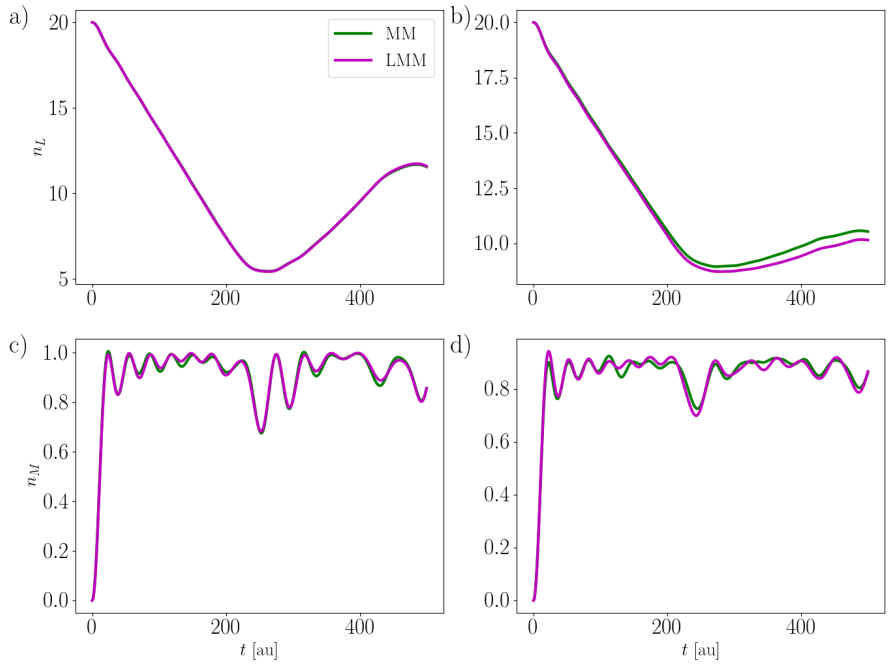

Figure 5.7. In a linear chain system($N = 10$), a) & b) n_L and c) & d) n_M are described. In the system, a) & c) $(T, U) = (-0.05, 0.005)$ while b) & d) $(T, U) = (-0.05, 0.05)$. For all classical mappings, trajectories are generated by uniform sampling.

5.2.3 Exciton energy transfer

In the previous section, we have shown that the MM mapping can be accurate in systems with weak and medium interactions. Here, we benchmark the applicability of the MM mapping to a second-quantization model for inter-molecular energy transfer between electronically excited molecules mediated by dipole-dipole interactions, i.e. excitonic energy transfer (EET). Although EET has been very successfully described by variational full quantum simulations, for example based on the MCTDH approach [135], realistic excitonic complexes may consist of many thousands of degrees of freedom, in which case mapping-based approaches might be a useful alternative.

We benchmark the MM and LMM to EET on ethylene clusters (fig5.8) in various configurations, while keeping the nuclei fixed. Each ethylene molecule is described within an orbital approximation and the construction of the EET model parameters for each cluster proceeds as follows: Localized molecular orbitals are obtained for each ethylene molecule through a separate Hartree-Fock calculation using a minimal atomic basis. Only the highest occupied molecular orbital (HOMO) and lowest occupied molecular orbital (LUMO) in each subsystem are further considered to describe the EET. Hence, each model consists of $4N$ spin-orbitals, where N is the number of ethylene molecules. The electrons are considered independent within each monomer and interact with the electrons of the other monomers via the two-electron Coulomb integrals involving the HOMOs and LUMOs of each monomer pair. Exchange terms are negligible due to distance between the monomers. The one- and two-body electronic integrals for each cluster configuration are provided as supporting information.

Energy transfer in a dimer system

We first consider two ethylene molecules facing each other and separated by 10 Å (fig5.8a). The initial state consists of one of the molecules singly excited (HOMO→LUMO) and the other molecule in its ground electronic state. The two localized excitonic states are resonant, resulting in a simple periodic EET with a period of about 200 fs. The direct Coulomb repulsion integrals between HOMO and LUMO orbitals in different monomers have values of roughly 1 eV, which contribute to energy shifts of the orbitals. The Coulomb integrals of the form $V_{L_I,H_{II}}^{L_{II},H_I}$ directly drive the exchange of excitation between the monomers and have a value of roughly 50 cm^{-1}. The EET dynamics is approximately captured by the MM and LMM mappings during the first period as seen in Figure (5.9), where the energy of the acceptor molecule is shown in units of the HOMO-LUMO energy gap. Both mappings fail to capture the full recursions of the exact dynamics due classical phase space dissipation of the ensemble of trajectories. Crucially, however, MM reproduces the initial rate of energy

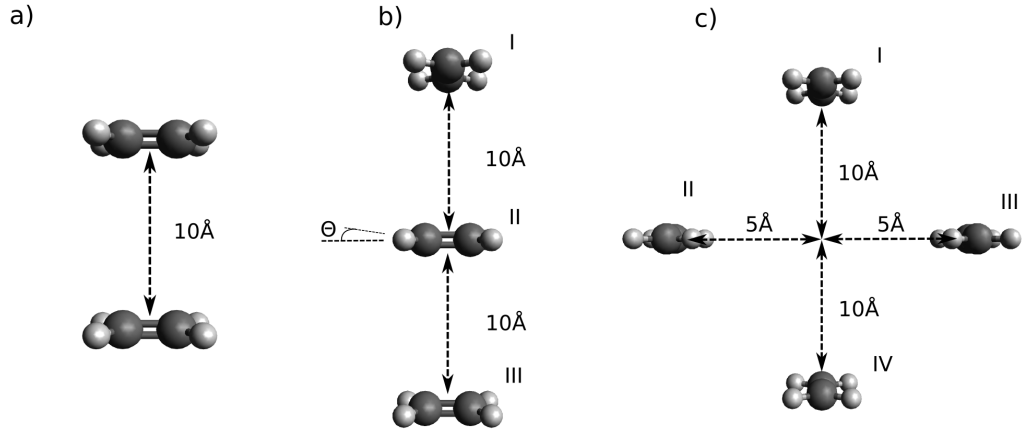

Figure 5.8. Ethylene a) dimer, b) trimer, and c) tetramer used in the EET simulations.

transfer while LMM deviates from the exact curve almost from the onset.

Geometrical effects in excitonic energy transfer

Next, we consider the situation where the EET proceeds through a bridging molecule (Figure (5.8 b)). The relative orientation between the C-C axis of the donor/acceptor and bridge molecules determines the strength of the dipole-dipole coupling, being it equal to zero for an orthogonal configuration. In the studied cluster, the donor and acceptor systems have a relative orientation of 90 degrees and therefore there is zero energy transfer between them without the intervention of the bridging molecule. A similar system was considered, e.g., in Ref. 136. The bridging system is considered at three angles $\theta = 0, 30, 45$ with respect to the acceptor molecule. For $\theta = 0$, no EET can occur because the transition dipole moments between the donor and the acceptor, as well as the mediator and the acceptor, are zero. For $\theta = 30$ deg., partial EET to the acceptor becomes possible. This partial EET is captured by both the MM and LMM mappings. In both cases, the classical models yield a smaller amount of energy transfer by 10 to 20% with respect to full quantum results after the first half period. As seen in fig (5.10a, 5.10b), the time-scale of the first period is well captured by the MM mapping, whereas LMM again yields a slower EET dynamics than the exact result. The general trends are similar for $\theta = 45$ degrees. The EET to the acceptor molecule is almost complete after the first half period. Both classical models yield a smaller total energy transfer by about 20% and LMM again yields a slower EET dynamics than the exact result.

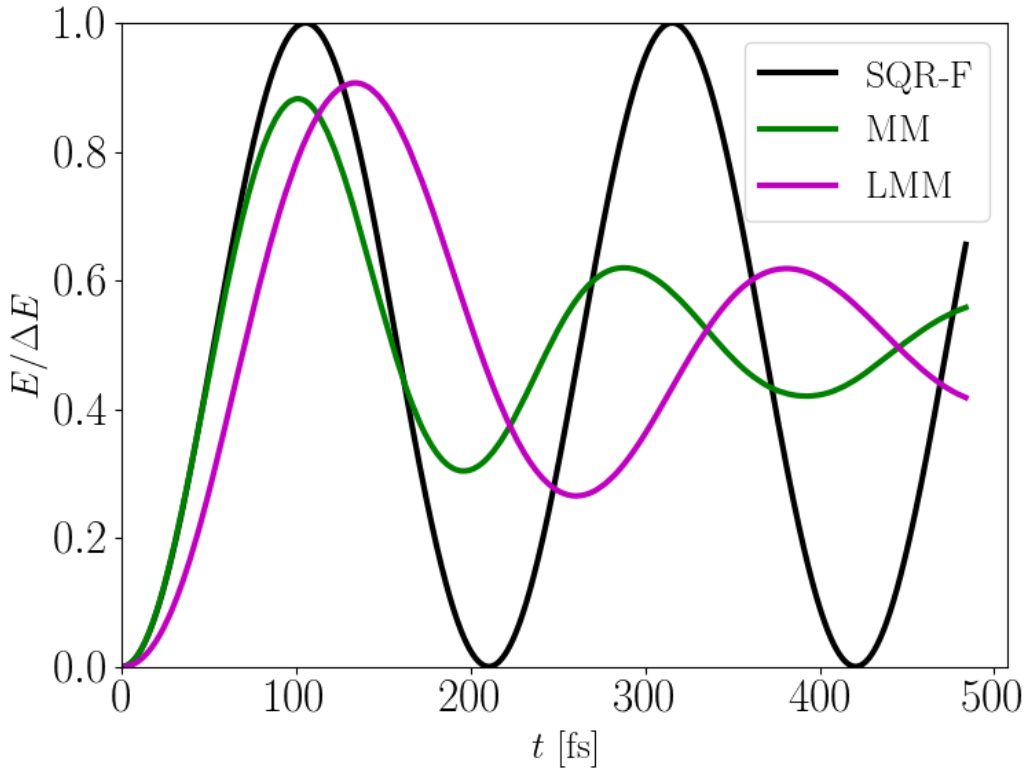

Figure 5.9. Energy (in units of the HOMO-LUMO energy gap ΔE) of the acceptor ethylene molecule in the ethylene dimer system.

Interference between two pathways

Finally, we consider a cluster with four monomers, two acting as donor (I) and acceptor (IV) systems, while the two other monomers (II, III) act as a symmetrical bridge between the former two. In all cases, monomer I is initially excited at $t = 0$ and the energy of monomer IV as a function of time is shown in Figure (5.11). The EET is faster when the two bridging pathways constructively interfere. These kinds of coherent EET dynamics involving various pathways are known to operate in models of light-harvesting complexes [137]. The onset of the EET process is well captured by the MM mapping, while the EET described by LMM is slower (cf. slopes during first 100 fs in fig (5.11a) and (5.11b)). After the first period, about 120 fs, both mappings deviate from the exact result and do not capture the almost complete back-transfer to monomer I after about 270 fs. When one of the pathways is completely suppressed, the EET process also reaches almost 100% yield, although it requires now a longer time, roughly 220 fs, until monomer IV is fully excited. Similarly, as before, the initial EET dynamics and the duration of the first half period are captured by the MM mapping. For all the considered ethylene clusters, the MM mapping properly describes the EET rate while the LMM underestimate the EET rate in the first half period.

Next, we artificially change the sign of the coupling matrix element between monomers

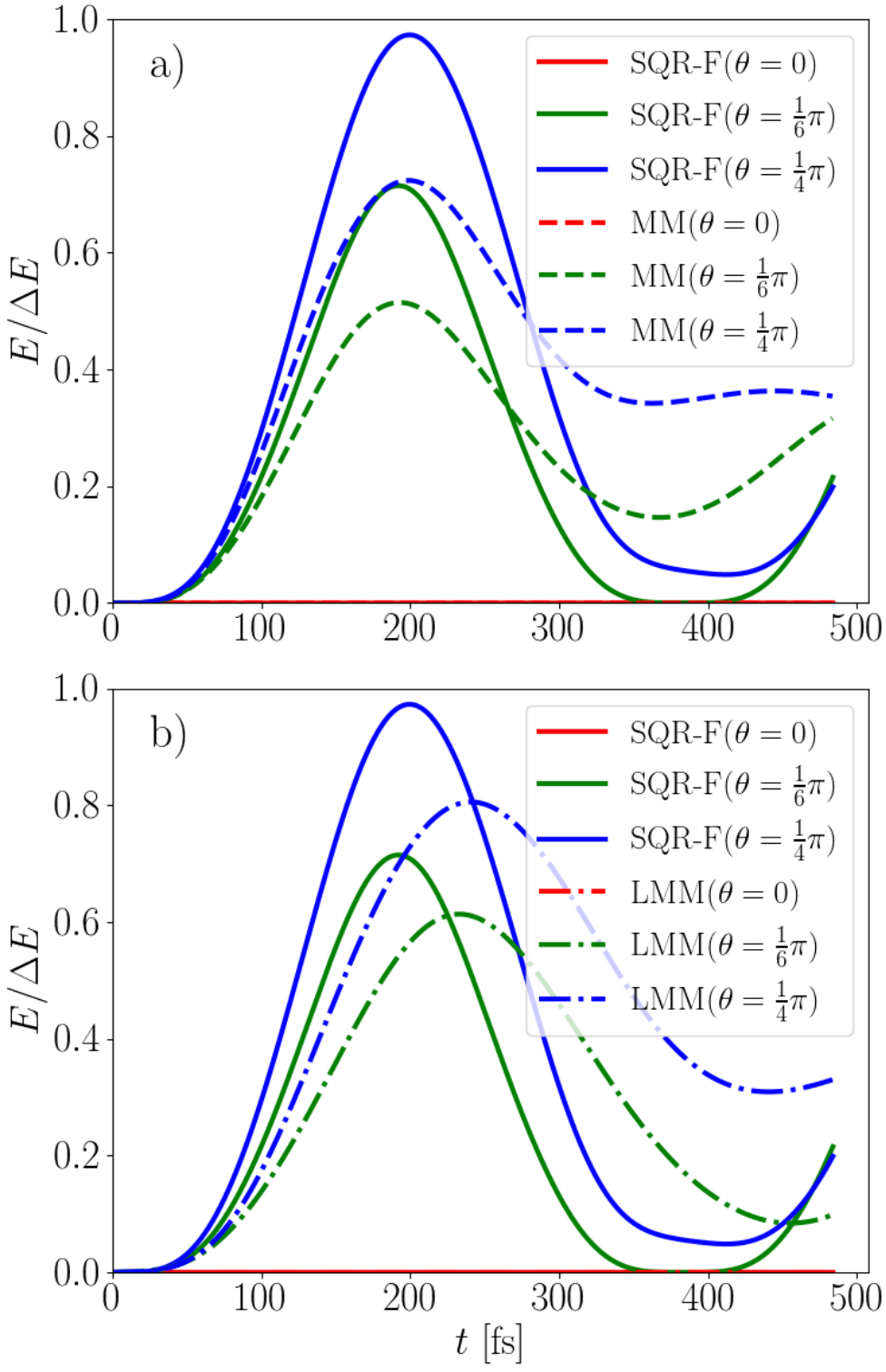

Figure 5.10. Energy of the acceptor monomer in the ethylene trimer system (normalized to the HOMO-LUMO energy gap). The donor is initially excited to the first singlet excited state. a) MM mapping and b) LMM mapping compared to the exact quantum mechanical result for different relative orientations of central monomer.

II and IV. This results in a destructive interference and the EET process is strongly suppressed, reaching only about 10 to 20% of the EET yield compared to the constructive case. Interestingly, the classical mappings capture this destructive interference effect and describe a strongly suppressed EET process. In this example, LMM reproduces the exact quantum result slightly better than MM at short times, and both mappings describe the EET dynamics approximately to within 10 to 20% of the HOMO-LUMO energy gap for the whole duration of the simulation, about 500 fs.

5.3 Conclusion

In this chapter, the application of MM mapping of fermions is explored. In both non-interacting and interacting systems, the MM mapping is compared with the quantum calculation and various classical mappings. The MM mapping provides an exact description to represent the one-body density of a quantum system that is composed of non-interacting particles, as long as the initial state can be prepared from fermionic occupations. This is because the one-body density and the one-body dynamics are the equivalent for both fermionic and bosonic systems that start from the same initial state. In interacting systems, the MM mapping deviates from the quantum calculations due to the improper description of the two-body densities. This is also observed in LMM, which is designed for mapping fermions. For excited state energy transfer, the MM mapping captures the initial EET rate and later on deviates from the exact dynamics. Our results show that the MM mapping does not perform worse than mappings designed specifically for fermions.

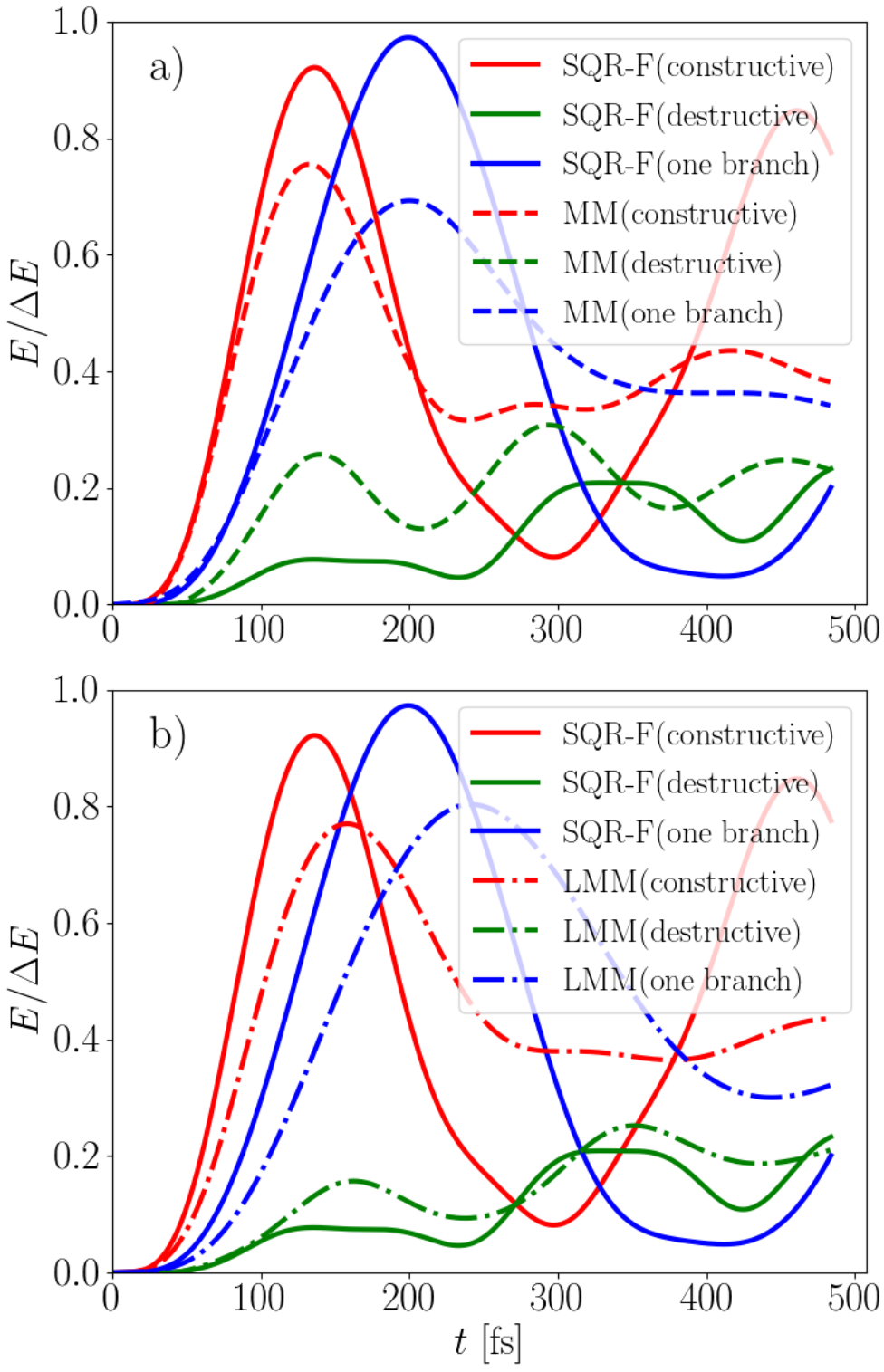

Figure 5.11. Energy of the acceptor monomer in the ethylene tetramer system (normalized to the HOMO-LUMO energy gap). The donor is initially excited to the first singlet excited state. a) MM mapping and b) LMM mapping compared to the exact quantum mechanical result.

Chapter 6

Summary and Outlook

In this thesis, we theoretically study cavity-controlled isomerization of HONO and explore the applicability of Meyer-Miller mapping for fermionic dynamics.

In chapter 3 and 4, we describe how the cavity alters the reaction rate of HONO isomerization. The reaction rates inside and outside the cavity are described by the reactive flux method, which is a fully classical method. We stress that no quantum effect is included in our study. Also, when investigating the modification of the reaction rate, a perfect cavity is assumed except for the last section of chapter 4.

In chapter 3, our main contribution has been to identify dynamical effects played by the cavity in the low-friction (or underdamped) regime of the reaction coordinate. In this regime, the cavity effect is twofold: (1) It *accelerates* the chemical rate by increasing the friction compared to the cavity-free system. The acceleration is attributed to the reduction of the recrossing. This reduction indicated trajectories are stabilized when visiting reactant and product regions, thus increasing the transmission coefficient $\kappa^{(c)}$ compared to $\kappa^{(0)}$. As the cavity coupling keeps increasing, the overall increased friction can introduce again more coupling at the barrier and the trend can overturn. The well-known Kramers turnover situation is reached, and this regime can exist in the condensed phase [115, 124]. (2) In the low-friction regime, sharp resonant effects are possible. These are related to the new IVR pathways offered by the cavity. In the products-side, they dissipate energy from the nascent hot products. In the reactants-side, the resonances funnel energy into the nascent activated complexes. Numerically, the former is captured by trajectories starting towards the products-side and being effectively captured there. The latter is captured by the trajectories initially moving towards reactants and being effectively captured as well. If this reactants-side capture would be ineffective, they would be counted as products but with a negative contribution to the flux, in this way lowering the transmission (cf. Eq. 3.4). When a bath is added to the HONO molecule and the overall friction is sufficiently increased, the model reverts to the already known as the overdamped regime where the cavity only affects

the recrossings at the top of the reaction barrier.

In chapter 4 we have investigated the effect of a cavity mode coupled to an ensemble of randomly oriented HONO molecules in the gas phase on the rate of the *cis-trans* isomerization reaction. Our simulations demonstrate that the activated molecule, which undergoes the chemical reaction at a given instant of time, and the ensemble of non-activated molecules, play fundamentally different roles. Specifically, the orientation with respect to the cavity that leads to the largest effect can be different for the activated molecule and the non-activated molecules. Also, the relevant resonances of the activated molecule that couple with the cavity may be shifted with respect to those of the non-activated molecules due to the much larger energy content of the former and the anharmonicity of the vibrational modes.

The largest modulation in the transmission coefficient occurs when the reaction coordinate (or a mode strongly coupled to the reaction coordinate) in the activated molecule becomes resonant with the cavity or a polaritonic resonance of the cavity with the non-activated molecules. This does not mean that the polaritonic resonance is already populated at room temperature before the chemical reaction takes place. It means that the polaritonic mode exists and it can be populated through coupling to a resonant subsystem, in this case the activated molecule. Finally, the main mechanistic cause for the relative change in the transmission coefficient, $R = \kappa^{(c)}/\kappa^{(0)}$, is the average energy loss from the activated molecule at short times, meaning until $\kappa^{(c)}$ reaches its plateau value, due to the resonant coupling to the rest of the polaritonic system. This can also be demonstrated by introducing lifetime of the cavity, which enhances the energy loss from the AM to the cavity.

Our simulations cover the single-molecule to small-ensemble strong coupling regime in the gas phase, and therefore one should be cautious about extrapolating our results to the macroscopic limit of large N in Fabry-Perot cavity experiments. Strong coupling in the gas phase with methane molecules has recently been observed by the Weichman's group [138], and this could represent an interesting avenue for gas-phase experiments of cavity-modified molecular reactivity under well-controlled conditions, where solid mechanistic insights can be gained by the interplay of experiment and theory. From a practical perspective, although the alteration of rates by Fabry-Perot cavities holds great mechanistic interest, the relatively small alterations achieved in most cases studied so far compared to chemical catalysts raise doubts regarding the viability of Fabry-Perot cavities as general catalytic components.

Our findings of chapter 3 and 4 shed important new light onto the question of collective effects in chemical reactivity under vibrational strong coupling. However, it still remains for future work to better understand how these cavity e□ects can survive in actual liquid phases and in the collective regime for truly macroscopic numbers of molecules. It is plausible these answers lie beyond the Hamiltonian of non-interacting molecules with idealized cavity

modes, and unveiling them may require studies of the transmission coe□cient with full consideration of the molecular as well as electromagnetic environments.

In chapter 5, we have investigated and compared the performance of different classical mappings (MM, SM, SM+JWT, LMM) to simulate the dynamics of fermions (electrons) in Fock space. Our aim has been to examine the advantages and limitations of the MM mapping and to contrast it with the LMM mapping, which incorporates specific features designed to improve the classical representation of fermionic dynamics in Fock space.

The MM mapping provides an exact description to represent the one-body density of a quantum system that is composed of non-interacting particles, as long as the initial state can be prepared from fermionic occupations. This is because the one-body density and the one-body dynamics are the equivalent for both fermionic and bosonic systems that start from the same initial state. To map the quantum one-body density to the classical phase space, an ensemble of trajectories is required. An exception occurs when there is only one electron included in the system. The phase-space mapping can be achieved either by randomly sampling the classical angle coordinates while selecting action-coordinate values that fulfill the initial quantum populations, or by picking a discrete set of points that yield the quantum one-body density when averaged under Eq (2.67). Both schemes are equivalent in the non-interacting case.

The SM mapping, with or without a Jordan-Wigner transformation, fails to describe the dynamics of non-interacting systems. This fact was already known and is due to the non-linear nature of Hamilton's equations originating from these models [69–71]. Importantly, combining the Jordan-Wigner transformation with the SM, which has been shown to be equivalent to the original MW mapping [31], does not result in any improvement.

We further considered the LMM mapping for fermions in comparison with the simpler MM mapping. LMM uses two vectorial coordinates per fermionic degree of freedom to restrict its maximal occupation and accounts for the sign-rules of fermionic matrix elements through the form of the interacting terms of the classical analog. LMM is in spirit similar to the original MW mapping. It can be obtained by mapping each fermionic DOF to two harmonic oscillators plus including the classical functions of the sign-change operators of a Jordan-Wigner transformation. LMM yields linear equations of motion for the non-interacting case and hence the exact one-body dynamics, but it uses twice as many degrees of freedom as the simpler MM mapping. These two mappings were applied to Hubbard-like cyclic models, to linear-chain impurity models and models of excitonic energy transfer. Cyclic models provide important insights into the role of anti-symmetry in classical mappings for fermions. In the cyclic systems, sign-change operators survive after applying the Jordan-Wigner transformation, while these operators are absent in the corresponding linear models. We found that inclusion of these non-linear terms in the MM (and SM) mapping

does more harm than good and worsens the description in all considered examples. As mentioned, linear tight-binding and Hubbard Hamiltonians do not feature sign-change operators after the JWT. Hence, the only actual difference between MM and LMM mappings in these examples is the limitation of the maximal orbital occupation in the LMM case. However, this enforced limitation of the LMM mappping plays no particular role in the considered impurity models. The orbital occupation in the central impurity site is very similar in both mappings and always below the maximal occupation of 1 electron per spin-orbital.

Finally, we considered the process of excitonic energy transfer in model clusters of ethylene. In the models, monomers interact via the two-body integrals calculated from localized Hartree-Fock orbitals in each monomer. We found that the MM mapping correctly captures the initial EET rate (roughly the first half period) and later on deviates from the exact dynamics.

Compared to MM, LMM gives similar results in terms of the overall EET efficiency and the interference patterns between different EET pathways. However, LMM tends to underestimate the energy transfer efficiency of EET, which may be important for some applications. Both LMM and MM can capture the quantum effects of constructive and destructive interferences that arise from the coherent coupling of the donor and acceptor chromophores.

Our results of chapter 5 indicate that the original MM mapping may be a valid classical analog alternative for the description of fermions in Fock space, and that it does not perform worse than mappings designed specifically for fermions. Our results also cast a question mark on whether the Jordan-Wigner transformation (or an equivalent formulation) is a useful addition to classical mapping strategies for fermions. Our conclusion is that it should be avoided. A limitation by the construction of the maximal fermionic occupation does not seem to be necessary either, at least within the bench-marked examples. In fact, in most of the considered examples, the MM mapping outperforms the more complicated LMM. Future work shall consider sampling strategies of the initial phase-space distribution designed for fermions, i.e. explicitly solving Eqs. (2.70) for a discrete set of phase-space points, as well as the inclusion of nuclear displacements.

Chapter 7

List of publications

- Sun, J., Sasmal, S., and Vendrell, O. (2021). A bosonic perspective on the classical mapping of fermionic quantum dynamics. Journal of Chemical Physics (Vol. 155, Issue 13). https://doi.org/10.1063/5.0066740
- Sun, J., and Vendrell, O. (2022). Suppression and Enhancement of Thermal Chemical Rates in a Cavity. Journal of Physical Chemistry Letters (Vol. 13, Issue 20, pp. 4441–4446). https://doi.org/10.1021/acs.jpclett.2c00974
- Sun, J., and Vendrell, O. (2023). Modification of Thermal Chemical Rates in a Cavity via Resonant Effects in the Collective Regime. Journal of Physical Chemistry Letters (Vol. 14, Issue 38, pp. 8397–8404). https://doi.org/10.1021/acs.jpclett.3c02199

Appendix A

OpenMM implementation

In chapter 4, we increase the size of the system from one molecule to 64 molecules. In order to reach higher computational efficiency, we build our molecular simulation on the top of OpenMM package. [96] There are several advantages of the OpenMM package. For example, OpenMM provides an efficient algorithm of equations of motion. Also, it is possible to do parallel calculations with GPU. The most important is that OpenMM allows developers to customize their potential energy surface, which means H_{cav} can be implemented. In this chapter, we aim to describe how we prepare calculations step by step through OpenMM.

In practice, we first prepare molecular structure, which is stored in a protein data bank (PDB) file. In OpenMM, several potential energy or forcefields have already been implemented, including vibrational energy, torsional energy, and various non-bonded interactions. And these forcefields can be described in XML files. On the other hand, considering molecules inside the cavity, H_{cav}, which has not been implemented in OpenMM yet, can be described by the function, *CustomNonbondedForce*, in OpenMM package. To prepare trajectories, we use the Langevin equation of motion to obtain a canonical ensemble. Finally, the trajectories are propagated under the Verlet equation of motion. And all these equations of motion can be found in OpenMM package.

A.1 Preparation of molecule

As mentioned, molecular structures are described in PDB files, which have been widely used in quantum mechanics and molecular dynamics. Not only small molecules, large system such as proteins can also be described in PDB files. Due to the ample information on proteins, the PDB format is designed to include all required information to describe the system for small and large molecules. The rules are summarized in Table A.1. In our study, we only use two types including **ATOM** and **TER** (see in Table A.2). For a single HONO molecule, all four atoms can be easily implemented in the type of **ATOM**. On the other

hand, we also need to manually add a cavity into the PDB file. The cavity here is treated as a virtual atom interacting with the HONO molecules.

Table A.1. Protein data bank format

Record Type	Columns	Data	Data Type
ATOM	1-4	ATOM	character
	7-11	Atom serial number	integer
	13-16	Atom Name	character
	17	Alternate location indicator	character
	18-20	Residue name	character
	22	Chain identifier	character
	23-26	Residue sequence number	integer
	27	Code for insertions of residues	character
	31-38	X orthogonal Angstrom coordinate	floating
	39-46	Y orthogonal Angstrom coordinate	floating
	47-54	Z orthogonal Angstrom coordinate	floating
	55-60	Occupancy	floating
	61-66	Temperature factor	floating
	73-76	Segment identifier (optional)	character
	77-78	Element symbol	character
	79-80	Charge (optional)	character
TER	1-3	TER	character
	7-11	Serial number	integer
	18-20	Residue name	character
	22	Chain identifier	character
	23-26	Residue sequence number	integer
	27	Code for insertions of residues	character

A.2 Description of Hamiltonian in OpenMM

Based on the Hamiltonian in eq 2.23, one need to describe the kinetic energy of both HONO molecules and the cavity, the potential energy of the HONO molecules, and the interaction between the HONO molecules and the cavity. In terms of the kinetic energy part, OpenMM can evaluate them automatically if we provide mass of each particle in the XML file. Since we aim to use an *ab initio* potential energy surface, the **CustomBondForce** function is utilized to describe on the top of OpenMM. For the same reason, the **CustomBondForce**

Table A.2. Selected Protein Data Bank Record Types

ATOM	atomic coordinate record containing the x,y,z orthogonal Angstrom coordinates for atoms in standard residues (amino acids and nucleic acids).
TER	indicates the end of a chain of residues. For example, a hemoglobin molecule consists of four subunit chains, which are not connected. TER indicates the end of a chain and prevents the display of a connection to the next chain.

function is utilized to build H_{cav} in OpenMM.

A.3 Sampling of trajectories

In order to obtain the ensemble average in Eq. 3.4, one needs to prepare a set of trajectories, which represent all possible microscopic configurations in a canonical ensemble at TS. The probability distribution of a canonical ensemble is given by the Boltzmann distribution, which describes the probability of finding the system in a particular energy state. The Boltzmann distribution is proportional to the exponential of the negative energy divided by the thermal energy of the system:

$$P(E) = \frac{1}{Z} e^{\frac{-E}{k_B T}}, \tag{A.1}$$

where E denotes the energy of the configuration, k_B is the Boltzmann constant, T is the temperature. Z denotes the partition function, which is the sum of the exponential of all possible energy of the configuration in the system:

$$Z = \sum_{\mu} e^{\frac{-E_\mu}{k_B T}}. \tag{A.2}$$

In our case, all microscopic configurations of the canonical ensemble is above TS, the probability is rewritten as:

$$P'(i) = \frac{1}{Z'} e^{\frac{-(E(\mu)-E^{\ddagger})}{k_B T}}, \tag{A.3}$$

where $E^{\ddagger}$ denotes the minimal energy at TS. And Z' represents a new partition function, which is written as:

$$Z' = \sum_{\mu} e^{\frac{-(E_\mu - E^{\ddagger})}{k_B T}}. \tag{A.4}$$

In this research, we consider N molecules collectively coupled to an optical cavity. In practice, for N molecules, one molecule is prepared at the top of the barrier between *cis* and *trans*

(activated) while the other $N-1$ molecules stay at either *cis* or *trans* (non-activated) in our system(Fig 4.1). Throughout this work, the system is thermalized through the Langevin equation of motion [139] at 300 K. The thermalization is reached by three cycles of 20 ps propagation and optimization of the geometry of the system. After thermalization, one trajectory is obtained for every 100 fs propagation to confirm the independence between each trajectory. To reach convergence, the ensemble average is obtained through 10000 trajectories, which is propagated through the Verlet equation of motion [140, 141].

A.4 Verlet equation of motion

The Verlet equation of motion is a numerical integration algorithm used to solve the equations of motion for a system of particles in classical mechanics. It is widely used in molecular dynamics simulations to model the motion of atoms and molecules over time. The Verlet algorithm is a second-order method, which means that it has a higher accuracy compared to first-order methods like the Euler method [142]. Several alogrithm has been developed to implement Verlet integration [140, 141]. A basic way can be derived based on the Taylor series expansion. The Verlet algorithm can be written as:

$$q(t+\Delta t) = 2q(t) - q(t-\Delta t) + \frac{dv}{dt}dt^2 + O(\Delta t^4) \tag{A.5}$$

$$v(t) = \frac{1}{2}(q(t+\Delta t) - q(t-\Delta t))/\Delta t + O(dt^3)) \tag{A.6}$$

The Verlet algorithm is computationally efficient and stable, and it conserves energy and momentum to a high degree of accuracy. This makes it a popular choice for molecular dynamics simulations of large systems, where accuracy and efficiency are important. Overall, the Verlet equation of motion provides a accurate method for simulating the motion of particles in classical mechanics, and is widely used in molecular dynamics simulations to study the behavior of atoms and molecules in a wide range of physical and chemical systems.

A.5 Langevin equation of motion

The Langevin equation of motion is a stochastic differential equation that describes the motion of a particle or molecule in a fluid, subject to a heat bath. It is a fundamental equation in the study of Brownian motion and has important applications in statistical physics, molecular dynamics simulations, and other areas of physics. The Langevin equation is given by:

$$m_i \frac{dv_i}{dt} = F_i - \gamma v_i + \eta_i, \tag{A.7}$$

where m_i is the mass of the i-th particle, v_i is its velocity at time t, and γ is friction coefficient. η_i is an uncorrelated random force, which represents the effect of the surrounding.

The random force η is often modeled as a normal distribution with mean zero and variance $2m_i\gamma k_B T$, where T is the temperature of the heat bath. η is assumed to be uncorrelated in time and to satisfy the fluctuation-dissipation theorem, which relates the strength of the random force to the friction coefficient. The integration is done using the Langevin leap-frog method [139]. In each step, the positions and velocities are updated as follows:

$$v_i(t + \Delta t/2) = v_i(t - \Delta t/2)\alpha + F_i(t)(1 - \alpha)/\gamma m_i + \sqrt{k_B T(1 - \alpha)/m_i}\eta_i \quad \text{(A.8)}$$

$$q_i(t + \Delta t) = q_i(t) + v_i(t + \Delta t/2)\Delta t, \quad \text{(A.9)}$$

where q_t represent position of the $i - th$ particle, Δt denotes the time step, and $\alpha = e^{-\gamma \Delta t}$.

Bibliography

[1] J. J. Hopfield. Theory of the contribution of excitons to the complex dielectric constant of crystals. *Phys. Rev.*, 112:1555–1567, Dec 1958.

[2] V. M. Agranovich. Dispersion of electromagnetic waves in crystals. *Soviet Physics - JETP*, 37:307–313, 1960.

[3] D. Meschede, H. Walther, and G. Müller. One-atom maser. *Phys. Rev. Lett.*, 54:551–554, Feb 1985.

[4] M. G. Raizen, R. J. Thompson, R. J. Brecha, H. J. Kimble, and H. J. Carmichael. Normal-mode splitting and linewidth averaging for two-state atoms in an optical cavity. *Phys. Rev. Lett.*, 63:240–243, Jul 1989.

[5] I. Pockrand, A. Brillante, and D. Möbius. Exciton–surface plasmon coupling: An experimental investigation. *J. Chem. Phys.*, 77(12):6289–6295, 12 1982.

[6] Joel Bellessa, Clementine Symonds, Julien Laverdant, Jean-Michel Benoit, Jean Claude Plenet, and Stephane Vignoli. Strong coupling between plasmons and organic semiconductors. *Electronics*, 3(2):303–313, 2014.

[7] D. G. Lidzey, D. D. C. Bradley, M. S. Skolnick, T. Virgili, S. Walker, and D. M. Whittaker. Strong exciton–photon coupling in an organic semiconductor microcavity. *Nature*, 395:53–55, 1998.

[8] James A. Hutchison, Tal Schwartz, Cyriaque Genet, Eloïse Devaux, and Thomas W. Ebbesen. Modifying Chemical Landscapes by Coupling to Vacuum Fields. *Angew. Chem.*, 124(7):1624–1628, February 2012.

[9] Felipe Herrera and Jeffrey Owrutsky. Molecular polaritons for controlling chemistry with quantum optics. *J. Chem. Phys.*, 152(10):100902, March 2020.

[10] Kalaivanan Nagarajan, Anoop Thomas, and Thomas W. Ebbesen. Chemistry under Vibrational Strong Coupling. *J. Am. Chem. Soc.*, 143(41):16877–16889, October 2021.

[11] Francisco J. Garcia-Vidal, Cristiano Ciuti, and Thomas W. Ebbesen. Manipulating matter by strong coupling to vacuum fields. *Science*, 373(6551):eabd0336, 2021.

[12] Elad Eizner, Luis A. Martínez-Martínez, Joel Yuen-Zhou, and Stéphane Kéna-Cohen. Inverting singlet and triplet excited states using strong light-matter coupling. *Sci. Adv.*, December 2019.

[13] Shota Takahashi, Kazuya Watanabe, and Yoshiyasu Matsumoto. Singlet fission of amorphous rubrene modulated by polariton formation. *J. Chem. Phys.*, 151(7):074703, 08 2019.

[14] Kati Stranius, Manuel Hertzog, and Karl Börjesson. Selective manipulation of electronically excited states through strong light–matter interactions. *Nat. Commun.*, 9:2273, 2018.

[15] Anoop Thomas, Jino George, Atef Shalabney, Marian Dryzhakov, Sreejith J. Varma, Joseph Moran, Thibault Chervy, Xiaolan Zhong, Eloïse Devaux, Cyriaque Genet, James A. Hutchison, and Thomas W. Ebbesen. Ground-State Chemical Reactivity under Vibrational Coupling to the Vacuum Electromagnetic Field. *Angew. Chem. Int. Ed.*, 55(38):11462–11466, September 2016.

[16] A. Thomas, L. Lethuillier-Karl, K. Nagarajan, R. M. A. Vergauwe, J. George, T. Chervy, A. Shalabney, E. Devaux, C. Genet, J. Moran, and T. W. Ebbesen. Tilting a ground-state reactivity landscape by vibrational strong coupling. *Science*, 363(6427):615–619, February 2019.

[17] Jyoti Lather, Pooja Bhatt, Anoop Thomas, Thomas W. Ebbesen, and Jino George. Cavity Catalysis by Cooperative Vibrational Strong Coupling of Reactant and Solvent Molecules. *Angew. Chem. Int. Ed.*, 58(31):10635–10638, 2019.

[18] Tao E. Li, Abraham Nitzan, and Joseph E. Subotnik. On the origin of ground-state vacuum-field catalysis: Equilibrium consideration. *J. Chem. Phys.*, 152(23):234107, June 2020.

[19] Xinyang Li, Arkajit Mandal, and Pengfei Huo. Cavity frequency-dependent theory for vibrational polariton chemistry. *Nat Commun*, 12(1):1315, February 2021.

[20] Arkajit Mandal, Xinyang Li, and Pengfei Huo. Theory of vibrational polariton chemistry in the collective coupling regime. *J. Chem. Phys.*, 156(1):014101, January 2022.

[21] Jing Sun and Oriol Vendrell. Suppression and enhancement of thermal chemical rates in a cavity. *J. Phys. Chem. Lett.*, 13(20):4441–4446, 2022.

[22] Lachlan P. Lindoy, Arkajit Mandal, and David R. Reichman. Resonant cavity modification of ground-state chemical kinetics. *J. Phys. Chem. Lett.*, 13(28):6580–6586, 2022.

[23] John P. Philbin, Yu Wang, Prineha Narang, and Wenjie Dou. Chemical reactions in imperfect cavities: Enhancement, suppression, and resonance. *J. Phys. Chem. C*, 126(35):14908–14913, 2022.

[24] Lachlan P. Lindoy, Arkajit Mandal, and David R. Reichman. Quantum dynamical effects of vibrational strong coupling in chemical reactivity. *Nat. Commun.*, 126(35):14908–14913, 2022.

[25] Tao E. Li, Joseph E. Subotnik, and Abraham Nitzan. Cavity molecular dynamics simulations of liquid water under vibrational ultrastrong coupling. *Proc. Natl. Acad. Sci.*, 117(31):18324–18331, August 2020.

[26] Tao E. Li, Abraham Nitzan, and Joseph E. Subotnik. Collective Vibrational Strong Coupling Effects on Molecular Vibrational Relaxation and Energy Transfer: Numerical Insights via Cavity Molecular Dynamics Simulations**. *Angew. Chem. Int. Ed.*, 60(28):15533–15540, 2021.

[27] Derek S. Wang, Tomáš Neuman, Susanne F. Yelin, and Johannes Flick. Cavity-Modified Unimolecular Dissociation Reactions via Intramolecular Vibrational Energy Redistribution. *J. Phys. Chem. Lett.*, pages 3317–3324, April 2022.

[28] Jorge A. Campos-Gonzalez-Angulo, Raphael F. Ribeiro, and Joel Yuen-Zhou. Resonant catalysis of thermally activated chemical reactions with vibrational polaritons. *Nat Commun*, 10(1):4685, October 2019.

[29] Matthew Du and Joel Yuen-Zhou. Catalysis by Dark States in Vibropolaritonic Chemistry. *Phys. Rev. Lett.*, 128(9):096001, February 2022.

[30] Juan B. Pérez-Sánchez, Arghadip Koner, Nathaniel P. Stern, and Joel Yuen-Zhou. Simulating molecular polaritons in the collective regime using few-molecule models. *Proceedings of the National Academy of Sciences*, 120(15):e2219223120, 2023.

[31] William H. Miller and Kim A. White. Classical models for electronic degrees of freedom: The second□quantized many□electron hamiltonian. *J. Chem. Phys.*, 84(9):5059–5066, 1986.

[32] H. D. Meyer and W. H. Miller. A classical analog for electronic degrees of freedom in nonadiabatic collision processes. *J. Chem. Phys.*, 70:3214–3223, 1979.

[33] Hans-Dieter Meyer and William H. Miller. Classical models for electronic degrees of freedom: Derivation via spin analogy and application to f*+h2→f+h2. *J. Chem. Phys.*, 71(5):2156–2169, 1979.

[34] Hans-Dieter Meyer and William H. Miller. Analysis and extension of some recently proposed classical models for electronic degrees of freedom. *J. Chem. Phys.*, 72:2272, 1980.

[35] Eric J. Heller. Frozen gaussians: A very simple semiclassical approximation. *J. Chem. Phys.*, 75(6):2923–2931, 1981.

[36] J. Tully. Molecular dynamics with electronic transitions. *J. Chem. Phys*, 93:1061–1071, 1990.

[37] S. Hammes-Schiffer and J. C. Tully. Proton-transfer in solution - molecular-dynamics with quantum transitions. *J. Chem. Phys.*, 101:4657–4667, 1994.

[38] Craig C. Martens and Jian-Yun Fang. Semiclassical-limit molecular dynamics on multiple electronic surfaces. *J. Chem. Phys.*, 106(12):4918–4930, 1997.

[39] Raymond Kapral and Giovanni Ciccotti. Mixed quantum-classical dynamics. *J. Chem. Phys.*, 110(18):8919–8929, 1999.

[40] Dónal Mac Kernan, Giovanni Ciccotti, and Raymond Kapral. Trotter-based simulation of quantum-classical dynamics. *J. Phys. Chem. B*, 112(2):424–432, 2008.

[41] Gerhard Stock and Michael Thoss. Semiclassical description of nonadiabatic quantum dynamics. *Phys. Rev. Lett.*, 78:578–581, Jan 1997.

[42] Michael Thoss and Gerhard Stock. Mapping approach to the semiclassical description of nonadiabatic quantum dynamics. *Phys. Rev. A*, 59:64–79, Jan 1999.

[43] M. Ben-Nun, Jason Quenneville, and Todd J. Martínez. Ab initio multiple spawning: Photochemistry from first principles quantum molecular dynamics. *J. Phys. Chem. A*, 104(22):5161–5175, 2000.

[44] Basile F. E. Curchod and Todd J. Martínez. Ab initio nonadiabatic quantum molecular dynamics. *Chem. Rev.*, 118(7):3305–3336, 2018.

[45] Ivano Tavernelli. Ab initio–driven trajectory-based nuclear quantum dynamics in phase space. *Phys. Rev. A*, 87:042501, Apr 2013.

[46] Basile F. E. Curchod, Ivano Tavernelli, and Ursula Rothlisberger. Trajectory-based solution of the nonadiabatic quantum dynamics equations: an on-the-fly approach for molecular dynamics simulations. *Phys. Chem. Chem. Phys.*, 13:3231–3236, 2011.

[47] Federica Agostini, Seung Kyu Min, Ali Abedi, and E. K. U. Gross. Quantum-classical nonadiabatic dynamics: Coupled- vs independent-trajectory methods. *J. Chem. Theory Comput.*, 12(5):2127–2143, 2016.

[48] Johan E. Runeson and Jeremy O. Richardson. Spin-mapping approach for nonadiabatic molecular dynamics. *J. Chem. Phys.*, 151(4):044119, 2019.

[49] Johan E. Runeson and Jeremy O. Richardson. Generalized spin mapping for quantum-classical dynamics. *J. Chem. Phys.*, 152(8):084110, 2020.

[50] Haifeng Lang, Oriol Vendrell, and Philipp Hauke. Generalized discrete truncated wigner approximation for nonadiabatic quantum-classical dynamics. *J. Chem. Phys.*, 155:024111, 2021.

[51] I. V. Aleksandrov. The statistical dynamics of a system consisting of a classical and a quantum subsystem. *Naturforsch.*, 36(8):902–908, 1981.

[52] Wayne Boucher and Jennie Traschen. Semiclassical physics and quantum fluctuations. *Phys. Rev. D*, 37:3522–3532, Jun 1988.

[53] Arlen Anderson. Quantum backreaction on ”classical” variables. *Phys. Rev. Lett.*, 74:621–625, Jan 1995.

[54] Oleg V. Prezhdo and Vladimir V. Kisil. Mixing quantum and classical mechanics. *Phys. Rev. A*, 56:162–175, Jul 1997.

[55] Craig C. Martens and Jian-Yun Fang. Semiclassical-limit molecular dynamics on multiple electronic surfaces. *J. Chem. Phys.*, 106(12):4918–4930, 03 1997.

[56] Arnaldo Donoso and Craig C. Martens. Simulation of coherent nonadiabatic dynamics using classical trajectories. *J. Phys. Chem. A*, 102(23):4291–4300, 1998.

[57] J. Caro and L. L. Salcedo. Impediments to mixing classical and quantum dynamics. *Phys. Rev. A*, 60:842–852, Aug 1999.

[58] Raymond Kapral and Giovanni Ciccotti. Mixed quantum-classical dynamics. *J. Chem. Phys.*, 110(18):8919–8929, 05 1999.

[59] Stephen J. Cotton and William H. Miller. Symmetrical windowing for quantum states in quasi-classical trajectory simulations: Application to electronically non-adiabatic processes. *J. Chem. Phys.*, 139(23):234112, 2013.

[60] Stephen J. Cotton and William H. Miller. A symmetrical quasi-classical spin-mapping model for the electronic degrees of freedom in non-adiabatic processes. *J. Phys. Chem. A*, 119(50):12138–12145, 2015.

[61] Guohua Tao. Topology of quantum coherence in singlet fission: Mapping out spin micro-states in quasi-classical nonadiabatic simulations. *J. Chem. Phys*, 152(7):074305, February 2020.

[62] Andrei A. Golosov and David R. Reichman. Classical mapping approaches for nonadiabatic dynamics: Short time analysis. *J. Chem. Phys*, 114(3):1065–1074, 01 2001.

[63] Maximilian A. C. Saller, Aaron Kelly, and Eitan Geva. Benchmarking quasiclassical mapping hamiltonian methods for simulating cavity-modified molecular dynamics. *J. of Phys. Chem. Lett.*, 12(12):3163–3170, March 2021.

[64] Ruibin Liang, Stephen J. Cotton, Robert Binder, Rainer Hegger, Irene Burghardt, and William H. Miller. The symmetrical quasi-classical approach to electronically nonadiabatic dynamics applied to ultrafast exciton migration processes in semiconducting polymers. *J. Chem. Phys.*, 149(4):044101, 2018.

[65] Xing Gao, Maximilian A. C. Saller, Yudan Liu, Aaron Kelly, Jeremy O. Richardson, and Eitan Geva. Benchmarking quasiclassical mapping hamiltonian methods for simulating electronically nonadiabatic molecular dynamics. *J. Chem. Theory Comput.*, 16(5):2883–2895, 2020. PMID: 32227993.

[66] William H. Miller. On the existence of semiclassical eigenvalues for irregular spectra. *J. Chem. Phys.*, 64(7):2880–2883, 1976.

[67] W. H. Miller and C. W. McCurdy. Classical trajectory model for electronically nonadiabatic collision phenomena. a classical analog for electronic degrees of freedom. *J. Chem. Phys.*, 69(11):5163–5173, 1978.

[68] P. Jordan and E. Wigner. Über das paulische äquivalenzverbot. *Zeitschrift für Physik*, 47:631–651, 1928.

[69] Bin Li and William H. Miller. A cartesian classical second-quantized many-electron hamiltonian, for use with the semiclassical initial value representation. *J. Chem. Phys.*, 137(15):154107, 2012.

[70] Bin Li, Tal J. Levy, David W. H. Swenson, Eran Rabani, and William H. Miller. A cartesian quasi-classical model to nonequilibrium quantum transport: The anderson impurity model. *J. Chem. Phys.*, 138(10):104110, 2013.

[71] Bin Li, William H. Miller, Tal J. Levy, and Eran Rabani. Classical mapping for hubbard operators: Application to the double-anderson model. *J. Chem. Phys.*, 140(20):204106, 2014.

[72] Amikam Levy, Wenjie Dou, Eran Rabani, and David T. Limmer. A complete quasiclassical map for the dynamics of interacting fermions. *J. Chem. Phys.*, 150(23):234112, 2019.

[73] Josef W. Zwanziger, Edward R. Grant, and Gregory S. Ezra. Semiclassical quantization of a classical analog for the jahn–teller e×e system. *J. Chem. Phys.*, 85(4):2089–2098, 1986.

[74] Troy Van Voorhis and David R. Reichman. Semiclassical representations of electronic structure and dynamics. *J. Chem. Phys.*, 120(2):579–589, 2004.

[75] David W. H. Swenson, Tal Levy, Guy Cohen, Eran Rabani, and William H. Miller. Application of a semiclassical model for the second-quantized many-electron hamiltonian to nonequilibrium quantum transport: The resonant level model. *J. Chem. Phys.*, 134(16):164103, 2011.

[76] Claude Cohen-Tannoudji, Jacques Dupont-Roc, and Gilbert Grynberg. *Photons and Atoms - Introduction to Quantum Electrodynamics*. Wiley, 1997.

[77] J. D. Jackson. *Classical Electrodynamics*. Wiley, 1962.

[78] Alexandre Archambault, Fran çois Marquier, Jean-Jacques Greffet, and Christophe Arnold. Quantum theory of spontaneous and stimulated emission of surface plasmons. *Phys. Rev. B*, 82:035411, Jul 2010.

[79] Johannes Flick, Michael Ruggenthaler, Heiko Appel, and Angel Rubio. Atoms and molecules in cavities, from weak to strong coupling in quantum-electrodynamics (QED) chemistry. *PNAS*, 114(12):3026–3034, March 2017.

[80] Samuel L. Braunstein and Peter van Loock. Quantum information with continuous variables. *Rev. Mod. Phys.*, 77:513–577, Jun 2005.

[81] Christian Schäfer, Michael Ruggenthaler, and Angel Rubio. Ab initio nonrelativistic quantum electrodynamics: Bridging quantum chemistry and quantum optics from weak to strong coupling. *Phys. Rev. A*, 98:043801, Oct 2018.

[82] Dominik Sidler, Michael Ruggenthaler, Heiko Appel, and Angel Rubio. Chemistry in Quantum Cavities: Exact Results, the Impact of Thermal Velocities, and Modified Dissociation. *J. Phys. Chem. Lett.*, 11(18):7525–7530, September 2020.

[83] Pei-Yun Yang and Jianshu Cao. Quantum Effects in Chemical Reactions under Polaritonic Vibrational Strong Coupling. *J. Phys. Chem. Lett.*, 12(39):9531–9538, October 2021.

[84] Christian Schäfer, Michael Ruggenthaler, Vasil Rokaj, and Angel Rubio. Relevance of the Quadratic Diamagnetic and Self-Polarization Terms in Cavity Quantum Electrodynamics. *ACS Photonics*, 7(4):975–990, April 2020.

[85] Edwin Albert Power, S. Zienau, and Harrie Stewart Wilson Massey. Coulomb gauge in non-relativistic quantum electro-dynamics and the shape of spectral lines. *Philos. Trans. R. Soc. Lond. Ser. Math. Phys. Sci.*, 251(999):427–454, September 1959.

[86] Derek S. Wang, Tomáš Neuman, Susanne F. Yelin, and Johannes Flick. Cavity-modified unimolecular dissociation reactions via intramolecular vibrational energy redistribution. *ArXiv210906631 Nlin Physicsphysics Physicsquant-Ph*, November 2021.

[87] David Chandler. *Introduction to Modern Statistical Mechanics*. Oxford University Press, New York, 1987.

[88] Bruce J. Berne, Michal Borkovec, and John E. Straub. Classical and modern methods in reaction rate theory. *J. Phys. Chem.*, 92(13):3711–3725, June 1988.

[89] Robert O. Rosenberg, Bruce J. Berne, and David Chandler. Isomerization dynamics in liquids by molecular dynamics. *Chemical Physics Letters*, 75(1):162–168, October 1980.

[90] Henry Eyring. The Activated Complex in Chemical Reactions. *J. Chem. Phys.*, 3(2):107–115, February 1935.

[91] Peter Hänggi, Peter Talkner, and Michal Borkovec. Reaction-rate theory: Fifty years after Kramers. *Rev. Mod. Phys.*, 62(2):251–341, April 1990.

[92] Jorge A. Campos-Gonzalez-Angulo and Joel Yuen-Zhou. Polaritonic normal modes in transition state theory. *J. Chem. Phys.*, 152(16):161101, April 2020.

[93] Igor Vurgaftman, Blake S. Simpkins, Adam D. Dunkelberger, and Jeffrey C. Owrutsky. Negligible Effect of Vibrational Polaritons on Chemical Reaction Rates via the Density of States Pathway. *J. Phys. Chem. Lett.*, pages 3557–3562, April 2020.

[94] Thomas W. Ebbesen. Hybrid Light–Matter States in a Molecular and Material Science Perspective. *Acc. Chem. Res.*, 49(11):2403–2412, November 2016.

[95] BJ Gertner, RM Whitnell, KR Wilson, and JT Hynes. Activation to The Transition-State - Reactant and Solvent Energy-Flow for a Model SN2 Reaction in Water. *J. Am. Chem. Soc.*, 113(1):74–87, January 1991.

[96] Eastman P, Swails J, Chodera JD, McGibbon RT, Beauchamp KA Zhao Y, Wang LP, Simmonett AC, Harrigan MP, Stern CD, Wiewiora RP, Brooks BR, and Pande VS. OpenMM 7: Rapid development of high performance algorithms for molecular dynamics. *PLoS Comput Biol.*, 13(7):1005659, 07 2017.

[97] Stephen J. Cotton and William H. Miller. The symmetrical quasi-classical model for electronically non-adiabatic processes applied to energy transfer dynamics in site-exciton models of light-harvesting complexes. *J. Chem. Theory Comput.*, 12(3):983–991, feb 2016.

[98] F. Remacle and R. D. Levine. On the classical limit for electronic structure and dynamics in the orbital approximation. *J. Chem. Phys.*, 113(11):4515–4523, 2000.

[99] David J. Tannor. *Introduction to quantum mechanics: a time-dependent perspective*. University Science Books, 2007.

[100] Kaya İmre, Ercüment Özizmir, Marcos Rosenbaum, and P. F. Zweifel. Wigner method in quantum statistical mechanics. *J. Math. Phys.*, 8(5):1097–1108, May 1967.

[101] Hans-Dieter Meyer and William H. Miller. Analysis and extension of some recently proposed classical models for electronic degrees of freedom. *J. Chem. Phys.*, 72(4):2272–2281, 1980.

[102] P. Jordan and E. P. Wigner. *The Collected Works of Eugene Paul Wigner: Part A: The Scientific Papers*. Springer Berlin Heidelberg, 1993.

[103] Haobin Wang and Michael Thoss. Numerically exact quantum dynamics for indistinguishable particles: The multilayer multiconfiguration time-dependent hartree theory in second quantization representation. *J. Chem. Phys.*, 131:024114, 2009.

[104] Sudip Sasmal and Oriol Vendrell. Non-adiabatic quantum dynamics without potential energy surfaces based on second-quantized electrons: Application within the framework of the MCTDH method. *J. Chem. Phys.*, 153(15):154110, oct 2020.

[105] A. Shalabney, J. George, J. Hutchison, G. Pupillo, C. Genet, and T. W. Ebbesen. Coherent coupling of molecular resonators with a microcavity mode. *Nat Commun*, 6:5981, January 2015.

[106] A. D. Dunkelberger, B. T. Spann, K. P. Fears, B. S. Simpkins, and J. C. Owrutsky. Modified relaxation dynamics and coherent energy exchange in coupled vibration-cavity polaritons. *Nat. Commun.*, 7(1):13504, December 2016.

[107] Adam D. Dunkelberger, Roderick B. Davidson, Wonmi Ahn, Blake S. Simpkins, and Jeffrey C. Owrutsky. Ultrafast Transmission Modulation and Recovery via Vibrational Strong Coupling. *J. Phys. Chem. A*, 122(4):965–971, February 2018.

[108] Zimo Yang, Bo Xiang, and Wei Xiong. Controlling Quantum Pathways in Molecular Vibrational Polaritons. *ACS Photonics*, 7(4):919–924, April 2020.

[109] Francesca Fassioli, Kyu Hyung Park, Sarah E. Bard, and Gregory D. Scholes. Femtosecond Photophysics of Molecular Polaritons. *J. Phys. Chem. Lett.*, 12(46):11444–11459, November 2021.

[110] Robrecht M. A. Vergauwe, Anoop Thomas, Kalaivanan Nagarajan, Atef Shalabney, Jino George, Thibault Chervy, Marcus Seidel, Eloïse Devaux, Vladimir Torbeev, and Thomas W. Ebbesen. Modification of Enzyme Activity by Vibrational Strong Coupling of Water. *Angew. Chem. Int. Ed.*, 58(43):15324–15328, 2019.

[111] Anoop Thomas, Anjali Jayachandran, Lucas Lethuillier-Karl, Robrecht M. A. Vergauwe, Kalaivanan Nagarajan, Eloise Devaux, Cyriaque Genet, Joseph Moran, and Thomas W. Ebbesen. Ground state chemistry under vibrational strong coupling: Dependence of thermodynamic parameters on the Rabi splitting energy. *Nanophotonics*, 9(2):249–255, February 2020.

[112] Mario V. Imperatore, John B. Asbury, and Noel C. Giebink. Reproducibility of cavity-enhanced chemical reaction rates in the vibrational strong coupling regime. *J. Chem. Phys.*, 154(19):191103, May 2021.

[113] Javier Galego, Clàudia Climent, Francisco J. Garcia-Vidal, and Johannes Feist. Cavity Casimir-Polder Forces and Their Effects in Ground-State Chemical Reactivity. *Phys. Rev. X*, 9(2):021057, June 2019.

[114] Javier del Pino, Johannes Feist, and Francisco J Garcia-Vidal. Quantum theory of collective strong coupling of molecular vibrations with a microcavity mode. *New J. Phys.*, 17(5):053040, May 2015.

[115] J.T. Hynes. Chemical reaction rates and solvent friction. *J. Stat. Phys.*, 42(1):149–168, 1986.

[116] Laura Masgrau, Àngels González-Lafont, and José M. Lluch. Variational Transition-State Theory Rate Constant Calculations with Multidimensional Tunneling Corrections of the Reaction of Acetone with OH. *J. Phys. Chem. A*, 106(48):11760–11770, December 2002.

[117] William H. Miller. Tunneling corrections to unimolecular rate constants, with application to formaldehyde. *J. Am. Chem. Soc.*, 101(23):6810–6814, November 1979.

[118] Frank Matzkies and Uwe Manthe. Accurate quantum calculations of thermal rate constants employing MCTDH: H2+OH→H+H2O and D2+OH→D+DOH. *J. Chem. Phys.*, 108(12):4828–4836, March 1998.

[119] Clàudia Climent and Johannes Feist. On the S N 2 reactions modified in vibrational strong coupling experiments: Reaction mechanisms and vibrational mode assignments. *Phys. Chem. Chem. Phys.*, 22(41):23545–23552, 2020.

[120] Falk Richter, Majdi Hochlaf, Pavel Rosmus, Fabien Gatti, and Hans-Dieter Meyer. A study of the mode-selective trans–cis isomerization in HONO using ab initio methodology. *J. Chem. Phys.*, 120(3):1306–1317, January 2004.

[121] Falk Richter, Pavel Rosmus, Fabien Gatti, and Hans-Dieter Meyer. Time-dependent wave packet study on trans-cis isomerization of HONO. *J. Chem. Phys.*, 120(13):6072–6084, April 2004.

[122] Falk Richter, Fabien Gatti, Céline Léonard, Frédéric Le Quéré, and Hans-Dieter Meyer. Time-dependent wave packet study on trans-cis isomerization of HONO driven by an external field. *J. Chem. Phys.*, 127(16):164315, October 2007.

[123] John A. Montgomery, David Chandler, and Bruce J. Berne. Trajectory analysis of a kinetic theory for isomerization dynamics in condensed phases. *J. Chem. Phys.*, 70(9):4056–4066, May 1979.

[124] Robert A. Kuharski, David Chandler, John A. Montgomery, Faramarz Rabii, and Sherwin J. Singer. Stochastic molecular dynamics study of cyclohexane isomerization. *J. Phys. Chem.*, 92(11):3261–3267, June 1988.

[125] Tor S. Haugland, Christian Schäfer, Enrico Ronca, Angel Rubio, and Henrik Koch. Intermolecular interactions in optical cavities: An ab initio QED study. *J. Chem. Phys.*, 154(9):094113, March 2021.

[126] Christian Schäfer, Johannes Flick, Enrico Ronca, Prineha Narang, and Angel Rubio. Shining Light on the Microscopic Resonant Mechanism Responsible for Cavity-Mediated Chemical Reactivity. *ArXiv210412429 Phys. Physicsquant-Ph*, June 2021.

[127] Oriol Vendrell. Collective Jahn-Teller Interactions through Light-Matter Coupling in a Cavity. *Phys. Rev. Lett.*, 121(25):253001, December 2018.

[128] Donald A. McQuarrie. *Statistical Mechanics*. University Science Books, Sausalito, California, 2000.

[129] Abraham Nitzan. *Chemical Dynamics in Condensed Phases: Relaxation, Transfer and Reactions in Condensed Molecular Systems*. Oxford University Press, 04 2006.

[130] H.-D. Meyer, U. Manthe, and L.S. Cederbaum. The multi-configurational time-dependent hartree approach. *Chem. Phys. Lett.*, 165(1):73–78, 1990.

[131] M. H. Beck, A. Jäckle, G. A. Worth, and H.-D. Meyer. The multiconfiguration time-dependent Hartree method: A highly efficient algorithm for propagating wavepackets. *Phys. Rep.*, 324:1–105, 2000.

[132] Tao E. Li, Abraham Nitzan, and Joseph E. Subotnik. Polariton relaxation under vibrational strong coupling: Comparing cavity molecular dynamics simulations against Fermi's golden rule rate. *J. Chem. Phys.*, 156(13):134106, 04 2022. 134106.

[133] G. A. Worth, M. H. Beck, A. Jäckle, O. Vendrell, and H.-D. Meyer. The MCTDH Package, Version 8.2, (2000). H.-D. Meyer, Version 8.3 (2002), Version 8.4 (2007). O. Vendrell and H.-D. Meyer Version 8.5 (2013). Version 8.5 contains the ML-MCTDH algorithm. Current versions: 8.4.18 and 8.5.11 (2019). See http://mctdh.uni-hd.de/.

[134] Uwe Manthe and Thomas Weike. On the multi-layer multi-configurational time-dependent hartree approach for bosons and fermions. *J. Chem. Phys.*, 146:064117, 2017.

[135] Hiroyuki Tamura, Miquel Huix-Rotllant, Irene Burghardt, Yoann Olivier, and David Beljonne. First-principles quantum dynamics of singlet fission: Coherent versus thermally activated mechanisms governed by molecularπstacking. *Phys. Rev. Lett.*, 115(10):107401, aug 2015.

[136] Jack S. Ford and David L. Andrews. Geometrical effects on resonance energy transfer between orthogonally-oriented chromophores, mediated by a nearby polarisable molecule. *Chem. Phys. Lett.*, 591:88 – 92, 2014.

[137] Stefano Tomasi and Ivan Kassal. Classification of coherent enhancements of light-harvesting processes. *J. Phys. Chem. Lett.*, 11:2348, 2020.

[138] John C. Wright. Coherent multidimensional vibrational spectroscopy. *Int. Rev. Phys. Chem.*, 21:185, 2002.

[139] Zhijun Zhang, Xinzijian Liu, Kangyu Yan, Mark E. Tuckerman, and Jian Liu. Unified efficient thermostat scheme for the canonical ensemble with holonomic or isokinetic constraints via molecular dynamics. *J. Phys. Chem. A*, 123(28):6056–6079, 2019.

[140] William C. Swope, Hans C. Andersen, Peter H. Berens, and Kent R. Wilson. A computer simulation method for the calculation of equilibrium constants for the formation of physical clusters of molecules: Application to small water clusters. *J. Chem. Phys.*, 76(1):637–649, 1982.

[141] C.K. Birdsall and A.B Langdon. *Plasma Physics via Computer Simulation*. McGraw-Hill Book Company, 1st edition, 1991.

[142] Kendall Atkinson. *An Introduction to Numerical Analysis*. Cambridge University Press, 2nd edition, 2003.

Acknowledgements

I am deeply grateful to all those who have contributed to the completion of this thesis through their guidance, support, and encouragement. Without their unwavering assistance, this achievement would not have been possible.

First and foremost, I would like to express my sincere appreciation to everyone who supported me during my Ph.D. research, Prof. Dr. Oriol Vendrell, for his guidance, encouragement, and feedback throughout this project. He was always available to discuss ideas, answer questions, and provide constructive criticism. His expertise, patience, and dedication have been instrumental in shaping the direction of this work.

I would like to acknowledge the collaboration and assistance of Dr. Sudip Sasmal, Markus Schröder, Krishna Nandipati, and David Mendive-Tapia. They generously shared their expertise and insights on the topic.

I extend my sincere appreciation to my friends and colleagues who have provided endless encouragement, thought-provoking discussions, and much-needed morale boosts during moments of doubt. Your support has been a constant source of inspiration.

My gratitude extends to the International Max Planck Research School Quantum Dynamics (IMPRS-QD) for their financial support, which has facilitated the execution of this research project. Your investment in my education has been integral to the successful completion of this thesis.

I would like to thank everyone who helped me in this project. I could not have done it without you.